# MESOSCALE MODELING OF CONTROLLED DEGRADATION IN POLYMER NETWORKS AND MELTS

---

A Dissertation
Presented to
the Graduate School of
Clemson University

---

In Partial Fulfillment
of the Requirements for the Degree
Doctor of Philosophy
Materials Science and Engineering

---

by
Vaibhav Abhay Palkar
May 2023

---

Accepted by:
Prof. Olga Kuksenok, Committee Chair
Prof. Marek Urban
Prof. Igor Luzinov
Prof. Ulf D. Schiller

# ABSTRACT

Controlled degradation of polymers finds various applications in fields ranging from the design of functional soft materials to recycling of polymers. In several of these applications, the characteristic length scale at which relevant processes occur ranges from nanometers to microns, typically referred to as the mesoscale. Although analytical models and continuum approaches inform our current understanding, analysis of degradation at the mesoscale is exceptionally limited. For modeling degradation at the mesoscale, we use the Dissipative Particle Dynamics (DPD) technique and the LAMMPS simulation software. Within the DPD framework, we model controlled degradation or the breaking of covalent bonds within a polymer as a stochastic process that reproduces first order degradation reaction kinetics. A known limitation of the DPD approach is polymer chains crossing through each other. Previous researchers had developed a modified segmental repulsive potential (mSRP) framework which prevents such crossing of polymers by introducing extra repulsion between the bonds of polymer chains. We modified the existing model in LAMMPS to enable switching off the extra repulsion when a bond is broken. We implemented this feature within the LAMMPS framework, and it is now available for the general scientific community as a part of the online open-source project. Later, we extended this feature to introduce the extra repulsion when a bond is formed to simulate the hydrosilylation reaction used in the synthesis of polymer derived ceramics.

As a model polymer network for studying degradation, we use the tetra-arm polyethylene glycol (tetra-PEG) based hydrogel films. Tetra-PEG networks have a uniform network structure and hence superior mechanical properties. We tracked the degradation

of these networks by measuring the evolution of the weight average molecular weight and dispersity during degradation. By tracking the fraction of degradable bonds broken, we identified the “reverse gel point”, the point where the polymer network dissolves into the surrounding solvent. Additionally, we tracked the erosion or mass loss from the degrading network by accounting for polymer fragments which dissociate and diffuse away from the network. We identified that the mass loss from the network depends on the initial thickness of the hydrogel films.

As a second system, we modeled the controlled degradation of nanogels that are either suspended in a single solvent or adsorbed onto a liquid-liquid interface. Controlled degradation of nanogels at an interface provides a dynamic approach to control interface topography at the nanoscale. We tracked the degradation of these particles by analyzing the evolution of their shape and size along with the molecular weights and dispersity in the system. In bulk, the particles swell almost homogenously while at the interface, the particles spread and cover the interface as degradation occurs. We found that the reverse gel point for these particles varies with the total initial number of precursors. The evolution of particle shape and size is significantly affected by the surrounding solvent and the surface tension between the two liquid phases.

The final part of this dissertation focuses on developing an initial framework to extend the above approach to model degradation of polyolefin melts under a local temperature gradient. The long term goal of this project is to study thermal degradation of polyolefins caused by introducing microwave absorbing nanosheets and subjecting the polymer to microwave irradiation.

# DEDICATION

I dedicate this dissertation to my girlfriend, Chandana Bathulapalli, without whose constant support and unwavering belief in me this PhD journey would not have been possible, and to my beloved family, my grandma, parents, brother, and sister-in law, whose encouragement and support have been invaluable.

# ACKNOWLEDGMENTS

First and foremost, I would like to express my sincerest gratitude towards my advisor, Prof. Olga Kuksenok. Her enthusiasm for research is infectious and her work ethic has set a standard for me to aspire to. It is truly admirable how much she prioritizes her students' success above all else and I am grateful for the countless hours she has spent in guiding me.

I would also like to thank my committee members, Prof. Ulf D. Schiller, Prof. Marek Urban, and Prof. Igor Luzinov for serving on my committee and guiding my research and academic journey.

Next, I would like to thank current and past members of Prof. Kuksenok's lab for their collaboration and discussions on various projects related to this dissertation, Dr. Chandan K. Choudhury, Yao Xiong, Sidong Tu, Devanshu Thakar, Arefin M. Anik, Eric Miller, and Cassandra Simpson.

I am particularly grateful to Prof. Ulf D. Schiller for his several insightful comments and suggestions at our Computational Materials Science group seminars every semester. Also, thanks to all the current and past members of the Schiller and Kuksenok research groups for their questions, comments, and discussions during these presentations.

I would especially like to thank Oleksandr Kuksenok. With his constant help and support I have been able to focus solely on my research without any technological concerns.

My sincere gratitude goes to Prof. Konstantin Kornev, for guiding me through the initial years of my graduate studies and helping me explore the experimental side of materials research.

My acknowledgements also go to Clemson University for generous allotment of compute time on the Palmetto cluster.

I would like to acknowledge the Materials Science and Engineering Department for awarding me the George Bishop Annual Fellowship and the David Jennings Memorial Fellowship. I would also like to thank the American Association of Textile Chemists and Colorists for awarding the Kanti and Hansa Jasani Family Scholarship.

I would also like to acknowledge Clemson's Materials Science and Engineering department and the following funding agencies for financially supporting my work. This research was supported in part by the National Science Foundation (NSF) EPSCoR Award # OIA-1655740, the Ameican Chemical Society's Petroleum Research Fund grant # 56632-ND7, NSF Award # 2110309, and NSF Award # 2134564. Any opinions, findings and conclusions or recommendations expressed in this dissertation are those of the author and do not necessarily reflect those of the National Science Foundation.

Last but not the least, I would like to thank the countless friends that I have made during my stay at Clemson, for supporting my journey and making my stay memorable.

TABLE OF CONTENTS

Page

TITLE PAGE ..... i

ABSTRACT ..... ii

DEDICATION ..... iii

ACKNOWLEDGMENTS ..... iv

LIST OF TABLES ..... ix

LIST OF FIGURES ..... x

CHAPTER

I. Introduction ..... 1

II. Dissipative Particle Dynamics simulations of polymers ..... 8

2.1 The standard DPD model ..... 9
2.2 The modified Segmental Repulsive Potential ..... 15
2.3 Energy conserving dissipative particle dynamics ..... 18
2.4 Integrating the dynamic equations and visualizing simulation results ..... 19

III. Implementation of a stochastic approach within the DPD framework for simulating controlled degradation with mSRP ..... 21

3.1 The stochastic approach for modeling degradation reactions ..... 22
3.2 Handling topology violations along with chemical reactions ..... 22
3.3 Kinetics of the degradation reaction ..... 23
3.4 Introducing local temperature dependence of the degradation reaction rate ..... 24

Table of Contents (Continued) Page

IV. Mesoscale modeling of controlled degradation and erosion in hydrogel films ..... 27

4.1 Introduction ..... 27
4.2 Methods ..... 29
4.3 Results and Discussion ..... 34
4.4 Conclusions ..... 52

V. Mesoscale modeling of nanogel degradation at interfaces and in bulk ..... 55

5.1 Introduction ..... 55
5.2 Methods ..... 58
5.3 Results and Discussion ..... 63
5.4 Conclusions ..... 85

VI. Modeling controlled thermal degradation of polyolefins under a local temperature gradient ..... 88

6.1 Introduction ..... 88
6.2 Methods ..... 96
6.3 Results and Discussion ..... 103
6.4 Conclusions ..... 112

VIII. Conclusions ..... 114

REFERENCES ..... 116

APPENDICES ..... 130

A: Implementation specifics for mSRP with bond breaking and formation ..... 130
B: Permissions to reproduce journal articles ..... 136
C: Permissions to reproduce figures ..... 139

LIST OF TABLES


Table Page

4.1 Simulation parameters sets for initial hydrogel films used in this work..... 32

5.1 Parameter sets corresponding to the degradation simulations in single solvent..... 61

5.2 Parameter sets used in simulations of degradation at interface ..... 62

6.1 Details of the simulated systems for determining properties of eDPD melts..... 106

LIST OF FIGURES

Figure Page

1.1 Schematic of a possible gelation and degradation pathway for tetra-PEG gels. (a) Structure of the two mutually reactive tetra-PEG precursors and the resulting network on gelation. (b) Change in storage modulus during gelation and subsequent degradation upon exposure to ultraviolet light. (c) Chemistry of the coumarin based degradation reaction and the resulting degraded tetra-PEG precursors. Reproduced with permission from ref. [24]. Copyright 2014 American Chemical Society. ..... 3

1.2 Schematic of a polyethylene glycol (PEG) based hydrogel platform that enables user-defined growth of a neural network. Adapted with permission from ref. [1]. Copyright 2014 American Chemical Society. ..... 3

1.3 Schematic of a degradable thermoset synthesized by introducing cleavable comonomers into the polymer chain. Reproduced from ref. [2] with permission from Springer Nature..... 4

1.4 Schematic of the coarse-graining scheme applied in Dissipative Particle Dynamics simulations. Reproduced from ref. [36] with permission from Elsevier. ..... 5

2.1 Representation of a set of coarse-graining schemes for polymeric species based on the number of water molecules coarse-grained into one DPD bead. The blue spheres on the right of Fig. 2.1 show a DPD bead representing water in each scheme. The red spheres on the left correspond to a DPD bead representing a hydrophobic hydrocarbon chain and the green beads in the middle represent a hydrophilic polyethylene oxide (PEO) chain. Reproduced with permission from ref. [67] Copyright 2016 American Chemical Society. ..... 11

2.2 Schematic representation of the three pairwise forces in DPD. The spring element at the top represents the conservative force, the dashpot in the middle represents the dissipative force and the bottom element represents the random force. Reprinted from ref. [35] with permission from AIP publishing. ..... 14

List of Figures (Continued)

Figure Page

2.3 The polymer volume fraction, $\phi$, (left $y$ axis, solid line) and crosslink density, $c_0$, (right $y$ axis, dashed line) as functions of $N_x$, i.e. the number beads between two crosslinks. Both lines are from analytical calculations. The symbols (filled for $\phi$ and unfilled for $c_0$) represent data points from simulations. Reproduced with permission from ref. [68] Copyright 2020 American Chemical Society. ..... 15

2.4 (a) Initial configuration of two entangled loops in good solvent. Simulation snapshots after $10^5$ timesteps using (b) mSRP and (c) sDPD formulations. Inset in b shows zoomed view of the entangled loops. (d) Distance between centers of masses (COMs) of the two loops. Figure reproduced from ref. [70] with permission from American Chemical Society. Copyright 2022 American Chemical Society. ..... 17

3.1 Schematic of the bond breaking and formation mechanism highlighting the role of mSRP pseudo beads (shown in yellow). When a bond is broken, the corresponding pseudo bead is deleted..... 23

3.2 (a) Evolution of the fraction of bonds intact as a function of time. Symbols represent average measurements over five DPD simulations with error bars representing standard deviations. Lines represent the function $p = exp\ (-kt)$, with $k = P/\tau_R$ provided in the legend in the units of $10^{-5}\ \tau^{-1}$. Table on the right contains a list of $P$ and $\tau_R$ values for each simulation in the figure. Figure reproduced from ref. [84] with permission from Springer Nature. ..... 25

4.1 (a) A fragment of polymer network with degradable bonds (bonds between red and blue beads), initial configuration prior to equilibration. Tetra-functional centers and PEG beads are shown in yellow and cyan, respectively, and water beads are shown as blue dots. (b-d) Snapshots of degradation of a reference hydrogel film (parameters set A in Table 4.1) with the degradation rate $k = 4.5 \cdot 10^{-5}$ at $t = 0$ in (b), $t = 10{,}000$ in (c), and $t = 20{,}000$ in (d). The largest connected cluster is highlighted in each snapshot, remaining polymer beads are shown as translucent and in less saturated color. Water beads are hidden for visual clarity..... 33

List of Figures (Continued)

Figure Page

4.2 (a) Evolution of the size of the largest cluster (in black) and number of clusters in the system (in red) for the degradation simulation shown in Fig. 4.1. (b-d) Distribution of cluster sizes at time instants $t = 10{,}000$ in (b), $t = 20{,}000$ in (c), and $t = 30{,}000$ in (d), the same time instants are marked in (a). Insets in (b-d) highlight the distributions of clusters with large number of precursors (>20 precursors).....35

4.3 Time evolution of (a) weight average degree of polymerization, $DP_w$ (left axis) and fraction of bonds broken, 1-p, (right axis), (b) normalized reduced $DP_w^r$ for 5 independent simulations for each degradation rate, and (c) reduced z-average degree of polymerization, $DP_z^r$ , and $DP_w^r$ for a single simulation run for each degradation rate. (d) Measured reverse gel points $p_c^w$ (solid bars) and $p_c^z$ (striped bars). Each curve in (a) and each data point in (d) represent average over 5 independent simulations, error bars represent the standard deviation. Each curve in (b) and (c) represents a single simulation and the data in (b) is normalized by the maximum value in each simulation. Gel film with $N_x = 6$ and reference parameters set (set A) is considered. Black, red, and green colors in (a)-(d) correspond to degradation rates $k_1 = 1.5x10^{-5}$, $k_2 = 3.0x10^{-5}$, and $k_3 = 4.5x10^{-5}$, respectively. These rates were obtained by setting $P = 3x10^{-6}, 6x10^{-6}$ and, $9x10^{-6}$ with $\tau_R = 0.2$. The degradation rate constants are provided in units of reduced simulation time, $\tau^{-1}$.....37

4.4 Time evolution of (a) number-average degree of polymerization, $DP_n$, and (b) polydispersity index, $PDI$. Each curve represents an average over 5 independent simulations, error bars represent the standard deviation. The colors have the same meaning as in Fig. 4.3 above.....38

List of Figures (Continued)

Figure Page

4.5 (a) Fractional mass loss from the largest topological cluster (black curve) and the largest agglomerate (red curve) measured up to the reverse gel point ($t = 20{,}500$) for the $N_x = 6$, 8x8x4 hydrogel film, degradation rate is $k = 4.5x10^{-5}$ in dimensionless units. The dashed line represents the fraction of degradable bonds intact, $p(t)$, for the same simulation run. Snapshots of the degrading film at (b) $t = 10{,}000$ and (c) $t = 18{,}000$ (corresponding time instances are marked in (a)). The fragments within the interaction distance with the largest agglomerate, including the fragments that are stuck inside the film, are highlighted in red with the rest of the polymer shown as translucent. (d) Number density distribution of all polymer beads in vertical direction averaged over xy plane (solid line), largest cluster (dashed line) and largest agglomerate (filled circles) at t=0 (black), $t = 10{,}000$ (red), and $t = 18{,}000$ (green).....43

4.6 Comparison of $f_T$ (solid) and $f_D$ (dashed lines) during the degradation of the hydrogel film as a function of relative extent of reaction with z direction box size 30 (black), 40 (red), 50 (green) and 60 (blue) units. .....45

4.7 Snapshots of the degrading film for parameter sets B(a,d), C(b,e) and E(c,f) (see Table 4.1). Polymer fragments that either remain stuck within the percolated film or remain within the interaction distance from it are shown in red. Water beads and fragments that are no longer within the interaction distance with the film are hidden for clarity of representation. The beads representing largest topological cluster are translucent. The snapshots in the top row (a-c) are taken at $t = 10{,}000$, corresponding to the fraction of degradable bonds intact $p = 0.64$. The snapshots in the bottom row (d-f) are taken at $t = 18{,}000$,corresponding to $p = 0.44$. .....47

4.8 (a) Number density distribution of all polymer beads in vertical direction averaged over x and y coordinates prior to degradation. (b) Polydispersity Index, $PDI$, as a function of the relative extent of reaction, $\epsilon$. The inset shows maximum value of $PDI$ as a function of a number of precursors in the film, $N_0$. (c-d) Fractional mass loss from the largest topological cluster, $f_T$ in (c) , and from the largest agglomerate, $f_D$, in (d) as functions of the relative extent of reaction, $\epsilon$. The colors in (a-d) represent simulations with the parameter sets provided in Table 4.1 as following: A(black), B(red), C(green), D(blue), E(orange), and F (purple). .....49

List of Figures (Continued)

Figure Page

4.9 Comparison of $PDI$ normalized by the number of precursors $N_0$ for the films described in Table 4.1. Colors correspond to the same parameters sets as in Fig. 4.7. ..... 51

5.1 Nanogel degradation in water and at the oil-water interface. (a) Schematic of the fragment of nanogel network with degradable bonds. Snapshots of a single nanogel corresponding to the reference parameter set (set F in Table 5.1), (b-d) nanogel degradation in good solvent and (e-j) degradation of a nanogel initially adsorbed at the oil-water interface. Dimensionless time, in units of $\tau$, is $t = 0$ in (b, e, h), $t = 10{,}000$ in (c, f, i), and $t = 22{,}000$ in (d, g, j). Polymer beads are colored as described in the text, oil beads are shown in red and water beads are hidden for visual clarity. (e-g) Side view and (h-j) top view of the nanogel at the interface. In the above snapshots, the largest cluster is highlighted while all other polymer beads shown as translucent. ..... 64

5.2 Tracking nanogel as the largest connected cluster in the system. Displacement of the center of mass of the largest cluster every 5000 simulation steps ($d_{COM}$, black curve, left axis) and reduced weight average degree of polymerization, ($DP_w^r$, red curve, right axis) during degradation of the nanogel with reference parameters set F (Table 5.1). Large "jumps" in $d_{COM}$ only occur at or after the reverse gel point (global peak in $DP_w^r$) indicating that up to the reverse gel point the largest cluster corresponds to the remaining portion of the original nanogel, hence only smooth changes in $d_{COM}$ are observed until the reverse gel point. As degradation continues, either the fragment corresponding to the original nanogel or one of the larger fragments that broke-off can become the largest clusters in the system; large "jumps" in $d_{COM}$ indicate that different fragments separated by a notable distance are identified as largest clusters at various time instants. ..... 65

5.3 Time evolution of (a) the radius of gyration, $R_g$, (b) shape anisotropy, $\kappa^2$, (c) reduced weight average degree of polymerization, $DP_w^r$ . The points marked by arrows correspond to the snapshots in Fig. 5.1. The data in c are normalized by the corresponding maxima. ..... 68

List of Figures (Continued)

Figure Page

5.4 Evolution of (a) shape anisotropy, (b) ratio of largest to smallest eigenvalues, (c) radius of gyration normalized by the value prior to degradation, and (d) topological and distance-based mass loss for degradation in water and at the interface. The distance-based mass loss is represented by green (in water) and blue (at interface) curves, and $f_T$ is shown in black (in water) and in blue (at interface). All data represent an average over five independent simulations with error bars denoting standard deviation... 71

5.5 Scaling of the reverse gel point with the number of precursors, $N_p$. The dependence of reverse gel point $p_c$ on the total number of precursors in the system. Symbols correspond to the measured $p_c$ for nanogels degrading in water (black symbols), nanogels degrading at the interface (red symbols) and hydrogel films from Ref. [70] (green symbols). The dashed line corresponds to $p_c^{\infty} = 0.39$. The error bars represent standard deviation taken over five independent simulations in each case. The red line corresponds to a weighted nonlinear least squares fitting of the simulated data. ..... 75

5.6 Effects of solvent quality on nanogel degradation in a single solvent. Snapshots of the nanogel degrading in a solvent with a_ps=82.0 (a-c) and in a solvent with $a_{ps} = 85.0$ (d-i) at t=0 (a, d), t=10,000 (b, e) and $t = 22{,}000$ (c, f). (g) Evolution of the distance-based mass loss and (h) radius of gyration during degradation in a solvent with $a_{ps} = 79.5$ (black curve), $a_{ps} = 82.0$ (red curve) and $a_{ps} = 85.0$ (green curve). ..... 78

5.7 Snapshots of the nanogel degrading at an interface with the oil-water interaction parameter (a-c) $a_{ow} = 100$ , (d-f) $a_{ow} = 120$ and (g-i) $a_{ow} = 150$ at (a, d, g) $t = 0$, (b, e, h) $t = 10{,}000$ and (c, f, i) $t = 22{,}000$..... 81

5.8 Effects of liquid-liquid interaction parameter. Evolution of (a) the number of contacts between two liquid phases, (b) radius of gyration, (c) extent of spreading, and (d) shape anisotropy for a nanogel particle degrading at the interface with $a_{ow} = 100$ (black curves), $a_{ow} = 120$ (red curves) and $a_{ow} = 150$ (green curves). All quantities are averaged over five simulations with error bars representing standard deviation. The data in (a) is normalized by the initial number of contacts for each case. ..... 83

List of Figures (Continued)

Figure Page

6.1 Figure 6.1. Schematic pathway of thermal degradation of polyethylene. Reproduced from ref. [18] with permission from Elsevier. ..... 90

6.2 Mechanism of chain-end scission reaction of polyethylene. Reproduced from ref. [173] with permission from Elsevier. ..... 91

6.3 Schematic of the random scission mechanism in linear polyethylene chain. Reproduced from ref. [21] with permission from Elsevier. ..... 93

6.4 (a) Mean squared displacement of eDPD beads. (b) Velocity profile during perioidic Poiseuille flow of the eDPD system. A simulation box of 30x30x30 was used in each case. ..... 101

6.5 Temperature dependence of (a) diffusivity and (b) kinematic viscosity of the eDPD fluid measured numerically from simulations (symbols) and calculated as per analytical expressions (solid lines). ..... 102

6.6 (a) Snapshot of the simulation box after the second equilibration step, see text for details. The red and blue beads indicate the immobile and mobile phases respectively. (b) Number density of eDPD beads inside the simulation box at the end of the first (black) and second (red) equilibrations. The dashed lines indicate the interface between the mobile and immobile phases. (c) Temperature profiles inside the simulation box at $t = 0$ (black), $t = 15$ (red), $t = 25$ (green) and $t = 75$ (blue). The symbols indicate measurements from eDPD simulations and lines indicate analytical solutions of the heat equation. ..... 105

6.7 Snapshots of polymer chains in the equilibrated simulation box with (a) $N = 20$ and (b) $N = 120$ beads per chain. Only eight chains are shown in each box while the rest are hidden. The simulation box size is $L = 20$ in a and $L = 40$ in b. (c) Scaling of the mean squared end-to-end distance (open symbols, blue line) and mean squared radius of gyration (closed symbols, red line). The lines show fitting to $a + bN^{\nu}$. Both quantities follow expected scaling for random coils with $\nu = 1.0$. ..... 108

List of Figures (Continued)

Figure Page

6.8 (a) Evolution of the mean squared displacement of the chain center of mass, $g_3(t)$ for melts of polymers with different degrees of polymerization (N) as described in the legend. (b) Dependence of the product $(N-1)\,.\,D$ on the number of bonds in the chains $N-1$. ..... 109

6.9 Evolution of the fraction of bonds intact during simulation of an eDPD melt with $N = 120$. The symbols represent data from an eDPD simulation and the line represents a fitting of the first order equation $p = exp\,(-kt)$. The values $P(T) = 900exp\,(-32/T), \tau_R = 0.1$ were used for the degradation simulation which was carried out at $T = 1.53$ in reduced DPD units corresponding to $T = 450^0C$. ..... 111

6.10 (a) Number fraction $n_i(x)$ and (b) weight fraction $w_i(x)$ distributions during random scission of polymer melt with initial degree of polymerization $N = 120$. Symbols represent data from eDPD simulations while lines representing plots of equations 6.11 and 6.13 above..... 112

# CHAPTER ONE

# Introduction

Polymeric materials undergoing controlled degradation are an integral part of several polymer applications. Controlled degradation is applied in the development of recycling strategies for thermosets[1] and thermoplastics[2], platforms for controlled delivery of drugs and biomolecules[3-5], platforms for tissue scaffolds[6] and materials for enabling smart biological applications[7]. In the context of polymeric materials, the term "degradation" typically refers to the chemical reaction that cleaves covalent bonds between atoms[8, 9]. Such breaking of covalent bonds can be enabled via several mechanisms; these mechanisms can be correspondingly classified according to the stimulus enabling the bond breaking reaction into: thermal degradation, photo-degradation, pH controlled degradation, etc. Photo-controlled degradation is often interesting in biological applications as it facilitates spatially-resolved dynamic control of the physical and chemical properties of the materials[10-16]. Thermal degradation is prominently used in the recycling of polyolefins[17, 18]. The breaking of covalent bonds is often accompanied by erosion[8, 9] which is defined as a decrease in the weight of the degrading polymer. During degradation of polymer networks, erosion occurs due to dissolution of soluble fragments that are formed during the degradation process[8]. This erosion process for polymer networks continues upto a critical "reverse gel point"[1, 8, 19, 20] beyond which the entire material becomes soluble. During thermal degradation of polyolefins, mass loss occurs due to formation of low molecular weight products that are volatile at the elevated temperatures applied to cause the degradation[21, 22].

Broadly, this dissertation will focus on understanding controlled degradation in two classes of polymeric materials: hydrogels and polyolefin melts. Hydrogels are polymers networks used in several biological applications. As a model hydrogel system, we analyze controlled degradation in hydrogels made from tetra-arm polyethylene glycol (tetra-PEG) precursors. To synthesize hydrogels, tetra-PEG precursors can either be crosslinked directly via reactive end functionalities[23, 24] or used in conjunction with linear or other multi-arm polymeric linkers[7, 25]. The specific model hydrogel network that we will use in a part of this dissertation can be synthesized experimentally by crosslinking tetra-PEG precursors with mutually reactive end functionalities[23, 24]. Gelation of such mutually reactive tetra-PEG precursors near overlap concentration of the precursors has been shown to form nearly ideal network structures exhibiting superior mechanical properties prior to degradation[23]. Controlled degradation can be introduced in this network by incorporating photo-degradable groups in the vicinity of the end functionalities responsible for gelation[24, 26-28]. Fig. 1.1 below shows the schematic of a possible gelation and degradation pathway[24] for synthesizing tetra-PEG networks. As shown in Fig. 1.1a, the two mutually reactive precursors, in this case the reactivity is introduced via the alkyne and azide functionalities, react to form a uniform network[23]. Network formation is evidenced via the increase in storage modulus during the gelation process (Fig. 1.1b). Then, degradation is carried out via the photo-degradation reaction of the coumarin group (Fig. 1.1c) which was originally incorporated in the vicinity of the azide functionality. Another example of a smart biological application based on the tetra-PEG polymeric precursors is shown in the schematic of Fig. 1.2. The green and red structure in Fig. 1.2 represents a hydrogel network synthesized using linear and tetra-arm polyethylene glycol (PEG) precursors, while the green blob represents neural cells embedded into the polymer.

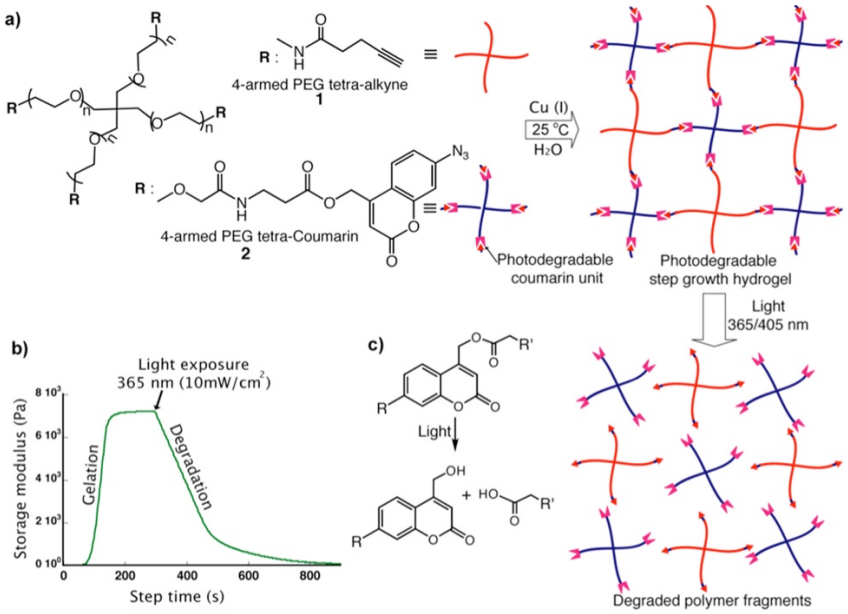


**Figure 1.1:** Schematic of a possible gelation and degradation pathway for tetra-PEG gels. (a) Structure of the two mutually reactive tetra-PEG precursors and the resulting network on gelation. (b) Change in storage modulus during gelation and subsequent degradation upon exposure to ultraviolet light. (c) Chemistry of the coumarin based degradation reaction and the resulting degraded tetra-PEG precursors. Reproduced with permission from ref. [24]. Copyright 2014 American Chemical Society.

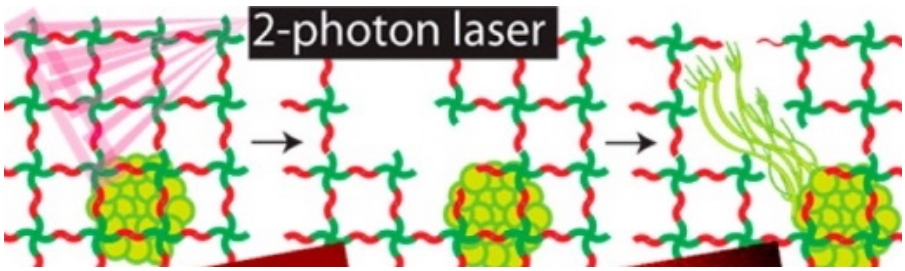


**Figure 1.2:** Schematic of a polyethylene glycol (PEG) based hydrogel platform that enables user-defined growth of a neural network. Adapted with permission from ref. [7]. Copyright 2014 American Chemical Society.

When a 2-photon laser is shone on the hydrogel network, it leads to controlled degradation in the direction that the laser is shone and enables growth of a neural network in this user-defined direction[7]. Although the focus in this dissertation is on hydrogels, similar controlled degradation can also be carried out in other polymer networks. A schematic for the use of controlled degradation in recycling of thermoset polymers[1] is shown in Fig. 1.3 below.

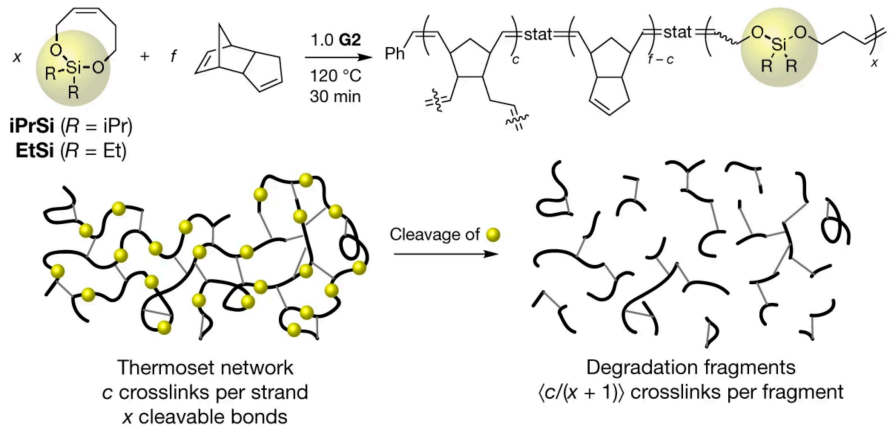


**Figure 1.3:** Schematic of a degradable thermoset synthesized by introducing cleavable comonomers into the polymer chain. Reproduced from ref. [1] with permission from Springer Nature.

In this work by Shieh et. al.[1] cleavable silyl ether based comonomers were introduced in the polydicyclopentadiene (pDCPD) polymer chains constituting a thermoset material. The silyl ether comonomers can be selectively degraded in the presence of an excess of tetrabutylammonium fluoride (TBAF). It was shown that a 25 wt% mixture of the degradation products from this process with DCPD produces a thermoset polymer with comparable properties as the original material[1].

It is important to note here that in several of the above applications, the characteristic features of degradable polymeric materials (e.g. mesh size of a degrading hydrogel network) [7,

10, 12] lies in the length scale of several nanometers upto a few microns; these length scales are also referred to as mesoscopic length scales. Traditionally, analytical and numerical approaches[8, 9, 20, 29-32], both applied at the much longer continuum length scales, have been applied to study degradation and erosion processes. Despite the mesoscopic length scale being relevant to the degradation process, an understanding of degradation and erosion at the mesoscale is exceptionally limited. Hence, the objective of this dissertation is to develop a framework for mesoscale modeling of degradation in polymer networks and melts. Using a mesoscale simulation technique allows to account for factors such as the diffusion of all degrading fragments, hydrodynamic interactions between various components, bonding topology of the polymer, heterogeneities in the polymer structure and, dependence of the degradation reaction on local environment.

In this dissertation we primarily use the mesoscale simulation technique called Dissipative Particle Dynamics (DPD)[33-35] to model these complex systems. Within the DPD approach, collections of atoms are coarse-grained into beads. The schematic in Fig. 1.4 below shows a representation of the coarse-graining approach applied in DPD simulations of polymers.

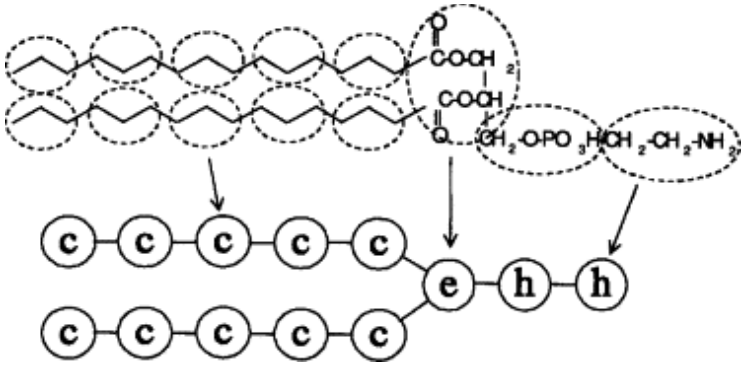


**Figure 1.4:** Schematic of the coarse-graining scheme applied in Dissipative Particle Dynamics simulations. Reproduced from ref. [36] with permission from Elsevier.

The atomic representation of a surfactant is provided at the top of the schematic in Fig. 1.4. The circles with dashed lines represent groups of atoms within the surfactant that are coarse-grained into a single DPD bead. Interactions between beads of various types, for example the beads labeled “c” and “e” in Fig. 1.4 are then defined by tuning a soft repulsive force between these beads[33-35]. A detailed description of the coarse-graining approach along with other salient features of the DPD scheme relevant to this work are provided in chapter two. Overall, DPD has been widely used to model a variety of complex polymeric systems[35-44]. To overcome unphysical topological crossings of polymer chains in DPD, we use the modified Segmental Repulsive Potential (mSRP) DPD formulation[45]. Further, we simulate the degradation reaction as a stochastic similar to the choice made in several other DPD simulations of reactions[46-51]. DPD approach has also been previously utilized to model gelation via atom transfer radical polymerization[52], free radical polymerization[49], iniferter-mediated photo-growth of hydrogels[50, 51], and complexation and decomplexation reactions within hydrogels[53]. It is worth noting that in some reactive systems the DPD approach can be integrated with another computational technique. Among the most recent examples, DPD approach integrated with quantum-chemical reaction path calculation was recently utilized to model the process of curing of thermoset resin[54]. DPD had also been recently used to quantify the effect of crosslinking reaction on drug diffusion in hyaluronic acid microneedles; in this work, atomistic MD simulations were performed to derive DPD parameters.[55] In chapter three of this dissertation, we describe the implementation of an approach to combine mSRP with the stochastic framework to simulate reactions.

The text in this dissertation is organized as follows. We first begin with a detailed description of our simulation approach which is provided in chapter two. In chapter two, we also

discuss the energy conserving DPD[56, 57] (eDPD) approach we use to simulate local temperature dependent degradation of polymer melts. Chapter three provides a detailed discussion of the approach we use for simulating the bond breaking reaction during degradation. We modified the mSRP DPD formulation to enable simulation of degradation while overcoming unphysical topological crossings of polymer chains. Details of our modifications and our implementation of this framework in the LAMMPS open-source software are also discussed in chapter three. We then use this framework to simulate photo-controlled degradation in hydrogel films. Chapter four describes our analysis of the degradation and erosion process in hydrogel films. We track the progress of degradation by measuring the fraction of degradable bonds intact along with the evolution of molecular weight distribution in the system. We identify a reverse gel point as a critical fraction of bonds broken and then analyze fractional mass loss from the hydrogel film as a function of the relative extent of the degradation reaction with respect to the reverse gel point. In chapter five, we apply our technique to the simulation of nanogel particles either suspended in a single solvent or adsorbed at the interface between two incompatible liquids. We identify the dependence of the reverse gel point of these particles on the total number of polymer precursors. We also analyze the evolution of particle shape and size during degradation and study the impact of surrounding conditions, such as the solvent quality, on the evolution of particle properties. In chapter six, we discuss our initial progress towards developing a framework for simulating local temperature dependent thermal degradation of polyolefin melts.

# CHAPTER TWO

## Dissipative Particle Dynamics simulations of polymers

Depending on the material properties to be studied, the dynamics of polymeric materials are generally modeled at three length scales: the atomistic scale (a few nanometers), the mesoscale (from tens of nanometers to a few microns) and the macroscale (hundreds of microns and beyond). Several simulation techniques, each with their own merits and limitations, exist at each of these length scales with Molecular Dynamics (MD) at the atomistic scale, Dissipative Particle Dynamics (DPD) and coarge-grained Molecular Dynamics at the mesoscale and Finite Elements Method at the macroscale being among the popular examples. As discussed in the previous chapter, several phenomena during the process of degradation of polymers occur at the mesoscale and hence a mesoscale modeling technique is appropriate for the simulation of this process. Specifically, we choose DPD, a particle-based technique involving soft repulsive potentials that has been used in modeling several phenomena in polymeric systems such as phase separation of polymer blends[58] and block copolymers[59], dynamics of polymer networks[46, 60] and bottlebrushes[61], dynamics of surfactants at interfaces[36] and entanglement regime dynamics of polymer melts[62, 63].

In comparison to MD, DPD reproduces complex hydrodynamic phenomena[64] with computational efficiency. While hydrodynamic interactions are shielded for polymer melts, they are known to play a significant role in polymer solutions with relatively low polymer concentrations. On the other hand, due to the soft repulsive potential in the standard form of the DPD approach, polymer chains can pass through each other causing unphysical topological

violations. We use the modified Segmental Repulsive Potential (mSRP)[62] formulation of DPD which decreases such topological violations.

In its standard form, the DPD method is a "thermostat" i.e., a constant temperature is maintained throughout the simulation. To simulate local variations of temperature within the DPD approach, Espanol[56] developed the energy conserving dissipative particle dynamics (eDPD) method that introduces temperature as an additional degree of freedom and adds energy conservation equations to the original DPD approach. Li et. al.[57] modified the eDPD approach to model variation of temperature dependent properties such as the Schmidt number in eDPD simulations. The eDPD method allows simulation of local temperature gradients and has been used to model temperature induced phase transitions in polymers[65].

In this chapter, we first introduce the details of the DPD approach relevant to this work. We then discuss the mSRP formulation that is used in all subsequent chapters and finally the eDPD approach used in chapter six to model local temperature gradients in polymer melts. The protocol we developed for modeling the bond breaking reaction with this simulation approach is discussed in more details in chapter three. Main features of the simulation methodology used in this dissertation are highlighted below while values of parameters and other specific details are provided in the corresponding chapters.

**2.1 The standard DPD model**

DPD was originally developed by Hoogerbrugge and Koelmann[66] as a more efficient alternative to molecular dynamics simulations for modeling complex fluid flow. Along with conceptual and algorithmic simplicity, the DPD method can handle relatively larger simulation timesteps[58]. The dynamics of a DPD system are simulated via beads whose motion is governed by the Newton's equations of motion[58]

$$\frac{d\boldsymbol{r}_i}{dt} = \boldsymbol{v}_i, \quad \frac{d\boldsymbol{p}_i}{dt} = \boldsymbol{F}_i, \tag{2.1}$$

where $\boldsymbol{r}_i, \boldsymbol{v}_i, \boldsymbol{p}_i = m\boldsymbol{v}_i$ and $\boldsymbol{F}_i$ are the position, velocity, momentum and total force corresponding to bead $i$, respectively. Each bead represents groups of atoms and parameters of the interaction forces between beads are governed by factors such as the degree of coarse-graining, i.e. the number of atoms represented by one bead. The total force between the non-bonded beads has three contributions

$$\boldsymbol{F}_i = \sum \left( \boldsymbol{F}_{ij}^C + \boldsymbol{F}_{ij}^D + \boldsymbol{F}_{ij}^R \right), \tag{2.2}$$

where the sum is evaluated over all other beads within an interaction distance $r_c$. $\boldsymbol{F}_{ij}^C, \boldsymbol{F}_{ij}^D$ and $\boldsymbol{F}_{ij}^R$ are respectively the conservative, dissipative and random contributions to the total force. We choose the typical "soft" repulsion form of the conservative force[58, 64]

$$\boldsymbol{F}_{ij}^C = a_{ij}\left(1 - \frac{r_{ij}}{r_c}\right)\boldsymbol{e}_{ij}, \tag{2.3}$$

where the parameter $a_{ij}$ sets a repulsion magnitude between beads $i$ and $j$, $r_{ij} = |\boldsymbol{r}_{ij}|$ is the distance between these beads, $\boldsymbol{r}_{ij} = \boldsymbol{r}_i - \boldsymbol{r}_j$, and $\boldsymbol{e}_{ij} = \boldsymbol{r}_{ij}/r_{ij}$. Other choices of the conservative repulsion are also possible. The conservative force described in equation (2.3) contains only the repulsive part of a harmonic force and is much weaker than the force derived from the Lennard-Jones potential in MD simulations. This peculiar characteristic of the DPD conservative force enables usage of longer simulation timesteps compared to MD[58]. The same peculiar form also allows polymer chains to unphysically pass through each other since the repulsion is not strong enough to avoid such topological violations[62, 63]. Suggested modifications to minimize unphysical crossing are discussed later in this chapter. The interaction parameter $a_{ij}$ in equation (2.3) is derived to match physical properties such as the compressibility of the system and the

nature of interaction between various species[36, 58]. An important aspect in making the choice of a suitable $a_{ij}$ is the particular coarse graining scheme used. For this dissertation, we choose the standard scheme originally introduced by Groot and Rabone[36] whose modifications and other alternative approaches have been analyzed by Lee et. al.[67] Fig. 2.1 below shows a compilation of a subset of possible coarse graining schemes[67] based on a choice of "degree of coarse-graining" or number of water molecules coarse-grained into one DPD bead.

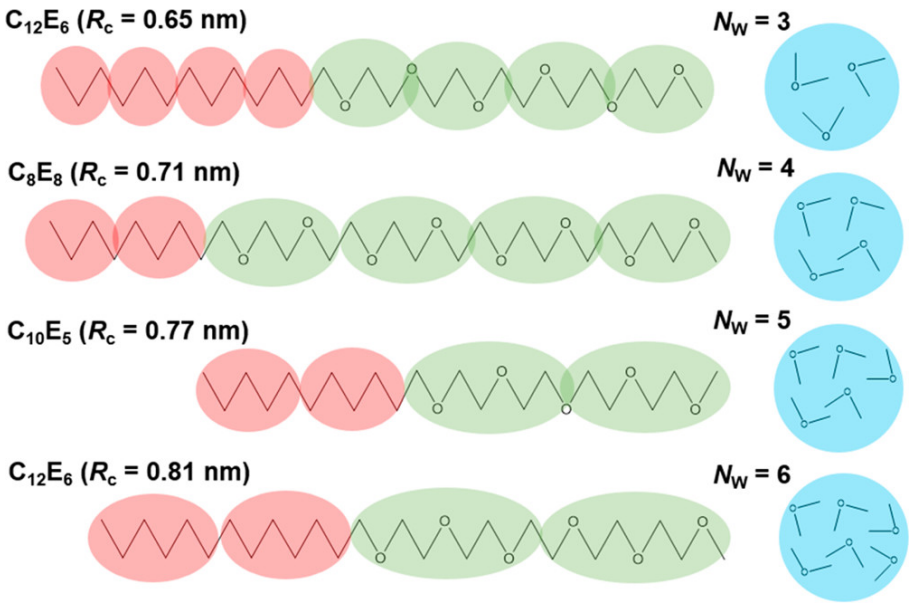


**Figure 2.1:** Representation of a set of coarse-graining schemes for polymeric species based on the number of water molecules coarse-grained into one DPD bead. The blue spheres on the right of Fig. 2.1 show a DPD bead representing water in each scheme. The red spheres on the left correspond to a DPD bead representing a hydrophobic hydrocarbon chain and the green beads in the middle represent a hydrophilic polyethylene oxide (PEO) chain. Reproduced with permission from ref. [67]. Copyright 2016 American Chemical Society.

In each of the coarse graining schemes in Fig. 2.1, each colored bead is chosen to represent the same volume, i.e. one blue bead represents the same volume as one green bead and also the same volume as one red bead. We choose the degree of coarse-graining corresponding to three water molecules coarse-grained into one bead, represented by the scheme in the top row of Fig. 2.1. This choice results in a dimensional value $r_c \approx 0.65$ nm. After making the choice of the degree of coarse graining, a choice is then made for $a_{ii}$, the interaction parameter in equation (2.3) for beads of same type. We choose $a_{ii} = 78\, k_B T / r_C$ as this choice is known to reproduce the compressibility of water at our chosen degree of coarse-graining[36, 58]. The interaction parameter for dissimilar beads is then chosen depending on the affinity between the two beads using the relation $a_{ij} = a_{ii} + 3.27\chi_{ij}$,[58] where $\chi_{ij}$ is the Flory-Huggins interaction parameter for the interaction between the respective beads. Note that our above choice of the model parameters is based on the approach derived by Groot and Warren[58]. The specific parameters for interaction between various components simulated in this dissertation are provided in the corresponding chapters.

Apart from the conservative force, the dissipative and random contributions to the total force are written as,[64]

$$\boldsymbol{F}_{ij}^{D} = -\gamma \omega_D(r_{ij})(\boldsymbol{e}_{ij} \cdot \boldsymbol{v}_{ij})\boldsymbol{e}_{ij}, \tag{2.4}$$

$$\boldsymbol{F}_{ij}^{R} = \sigma \omega_R(r_{ij})\, \zeta_{ij} \Delta t^{-\frac{1}{2}}\, \boldsymbol{e}_{ij}, \tag{2.5}$$

correspondingly, here γ and σ are the strengths of the dissipative and random forces, $\boldsymbol{v}_{ij} = \boldsymbol{v}_i - \boldsymbol{v}_j$ is the relative velocity, $\zeta_{ij}$ is a symmetric Gaussian distributed random variable with zero mean and unit variance, and $\Delta t$ is the simulation time step. The random force provides thermal fluctuations causing the system to effectively "heat up" while the dissipative force decreases the relative velocity of beads effectively causing the system to "cool down". These forces are coupled

via the fluctuation-dissipation theorem which tunes the magnitude of the two forces, effectively enforcing a thermostat and leading to the correct thermodynamic equilibrium distribution[64]. The following relations must be satisfied in order to satisfy the fluctuation-dissipation theorem,

$$\sigma^2 = 2\gamma k_B T, \tag{2.6}$$

$$\omega_D(r_{ij}) = \omega_R^2(r_{ij}). \tag{2.7}$$

We choose the soft repulsion form of the weight function $\omega_D(r_{ij}) = \omega_R^2(r_{ij}) = \left(1 - \frac{r_{ij}}{r_c}\right)^2$. According to the standard Groot and Warren[58] DPD model, we set $r_c$, temperature, and mass of a bead at 1.0 in reduced DPD units, and the bead number density in the simulation box is set at 3. The simulation time is correlated to a dimensional unit of time by matching diffusion coefficient of water beads with the known value of self-diffusion coefficient of water as[36] $\tau \approx 88\,ps$ . Unless otherwise specified, all quantities reported in this dissertation are in reduced DPD units, with $r_c$ as the unit length, τ as unit time, and $k_B T$ as the unit of energy.

Overall, the non-bonded interactions in the standard DPD model have been summarized in the graphic shown in Fig. 2.2 below. The conservative force, represented by the spring element in Fig. 2.2, tunes the interaction between beads of different types. The dissipative and random forces, depicted by the middle and bottom element in Fig. 2.2 can be tuned to vary physical properties such as the diffusivity and viscosity[57].

Lastly, for creating polymer chains, the DPD beads are stringed together by introducing a force corresponding to the harmonic potential,

$$U_{bond} = \frac{K_b}{2}\left(r_{ij} - r_b\right)^2, \tag{2.8}$$

where $K_b$ is a spring constant and $r_b$ is the equilibrium bond distance taken as $K_b = 1000$ and $r_b = 0.7$, respectively.

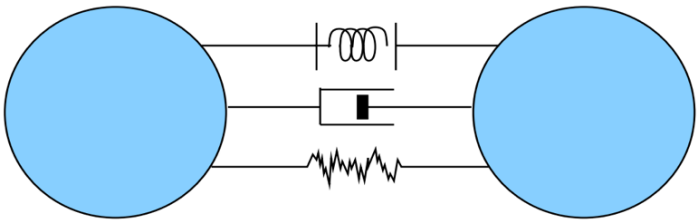

**Figure 2.2:** Schematic representation of the three pairwise forces in DPD. The spring element at the top represents the conservative force, the dashpot in the middle represents the dissipative force and the bottom element represents the random force. Reprinted from ref. [35] with permission from AIP publishing.

While the main goal of this dissertation is to study degradation of polymer networks, the standard DPD technique described so far can also be used to simulate equilibrium characterisitcs of polymer networks. Specifically, we used the above described framework for modeling the equilibrium swelling of polyacrylamide (PAAm) hydrogels[68]. The equilibrium swelling data from our DPD simulations of PAAm hydrogels[68] is shown in Fig. 2.3. For simulating the PAAm hydrogels, we made a choice for the $a_{ij}$ parameter in equation (2.3) based on the Flory-Huggins $\chi$ parameter for the PAAm-water interaction as described above. We compared the equilibrium swelling volume fractions $\phi$ and crosslink densities $c_0$ measured from DPD simulations with analytical estimates of the quantities.[68] The analytical estimate of $\phi$ is obtained from the Flory-Rehner swelling theory of polymers. According to Flory-Rehner theory, the equilibrium swelling is governed by a balance between the osmotic pressure due to the favorable polymer-solvent interactions and the elastic stresses developing within the hydrogel due to the stretching of polymer strands. An affine network approximation was used for the analysis in Fig. 2.3 and a near perfect

matching between the analytical estimates and values measured from the DPD simulations is evident in Fig. 2.3[68]

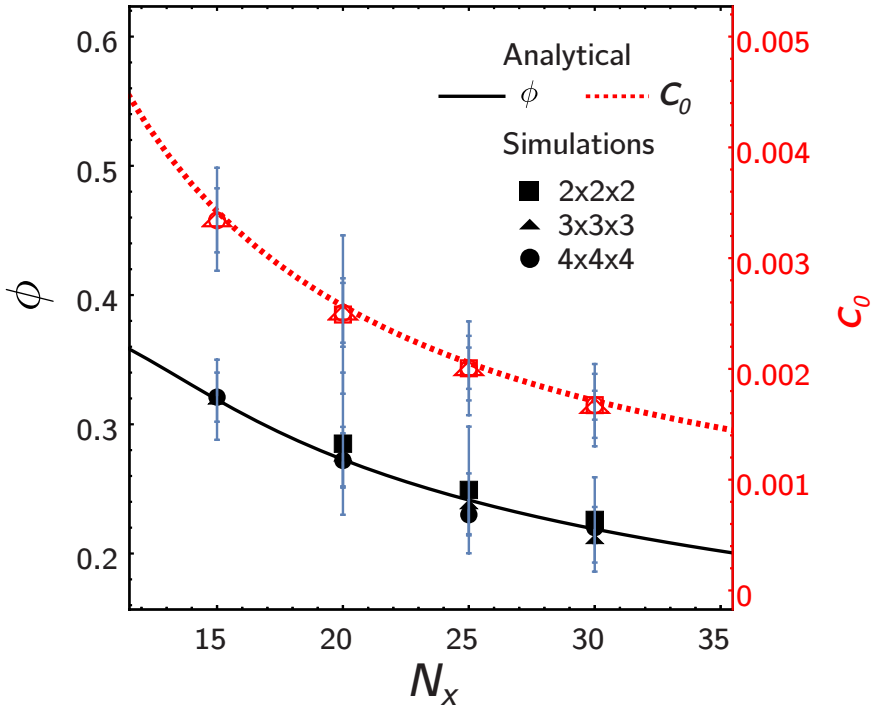


**Figure 2.3.** The polymer volume fraction, $\phi$, (left $y$ axis, solid line) and crosslink density, $c_0$, (right $y$ axis, dashed line) as functions of $N_x$, i.e. the number beads between two crosslinks. Both lines are from analytical calculations. The symbols (filled for $\phi$ and unfilled for $c_0$) represent data points from simulations. Reproduced with permission from ref. [68] Copyright 2020 American Chemical Society.

### 2.2 The modified Segmental Repulsive Potential

As mentioned in the previous section, the soft conservative force in DPD allows for chains to unphysically cross through each other. This concerns simulations of polymers since such topological violations would effectively mean phenomena such as entanglements are not captured

by the simulations. Kartunnen et. al.[63] reported that such topological violations can be decreased by making the bonds between monomers stiffer, hence causing stronger repulsion when two polymer chains approach each other. In an alternative approach, Kumar and Larson[69] first developed a segmental repulsive potential (SRP) which adds extra repulsive forces between the bonds of neighboring polymer chains. The additional SRP force is given as,

$$\boldsymbol{F}_{ij}^{SRP} = b\left(1 - \frac{d_{ij}}{d_c}\right)\boldsymbol{e}_{ij}^{S}, \tag{2.9}$$

where, $d_c$is the SRP cut-off distance,$b$ is the strength of the SRP repulsion, $d_{ij} = |\boldsymbol{d}_{ij}|$ is the distance between bonds and $\boldsymbol{e}_{ij}^{S} = \boldsymbol{d}_{ij}/d_{ij}$ is the unit vector in the direction from one bond to another. In the original SRP approach, the minimum distance between bonds is used as the distance measure[69]. This approach was later modified by Sirk et. al[62] to use the distance between mid-points of bonds as the distance measure. As compared to the original SRP, use of the distance between mid points of the bonds was shown to improve structural and thermodynamic properties of the simulate polymer chains. By selecting appropriate parameters, the modified approach demonstrates minimization of topological violations and reproduces entanglement regime scaling of the diffusion constant of polymer chains in the melt state.[62] We use the parameters $b = 80$ and $d_c = 0.8$ in our work, these parameters were shown to minimize topology violations in the original framework. We additionally conducted a series of simulations for the dynamics of entangled polymer loops in a good solvent to validate minimization of bond crossings using the above parameters. We simulated two entangled polymer loops (Fig. 2.4a) for $10^5$ DPD steps with and without the mSRP potential. We then compared the standard DPD (sDPD) simulation, without mSRP interactions, and the simulation using mSRP DPD formulation Fig. 2.4b-d. Snapshots at late simulation time are shown in Fig. 2.4b,c respectively. Due to the added repulsion, loops remains entangled for the entire length of the mSRP simulation while the loops pass through each

other at a very early stage in the DPD simulation. To quantify this behavior, we measure the time evolution of the distance between the centers of masses (COMs) of the two loops (Fig. 2.4d).

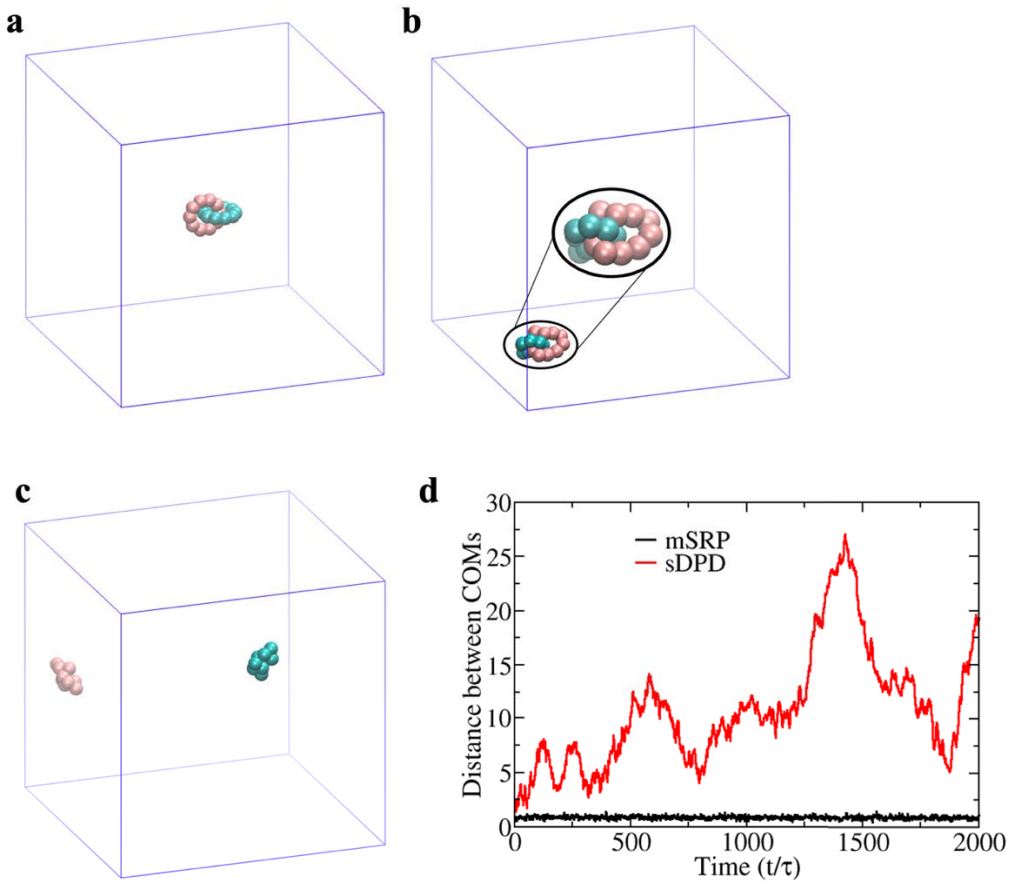


**Figure 2.4**: (**a**) Initial configuration of two entangled loops in good solvent. Simulation snapshots after $10^5$ timesteps using (**b**) mSRP and (**c**) sDPD formulations. Inset in **b** shows zoomed view of the entangled loops. (**d**) Distance between centers of masses (COMs) of the two loops. Figure reproduced from ref. [70] with permission from American Chemical Society. Copyright 2022 American Chemical Society.

This distance remains small for the mSRP simulation (black curve), confirming that the loops remain entangled throughout, while it is significantly higher for the separated sDPD loops. We

repeated the mSRP simulation and observed the above reported behavior in 98 out of 100 independent simulations run for $10^7$ DPD steps, in two simulations the loops separated at very early timestep (less than 100 steps, data not shown).

### 2.3 Energy conserving dissipative particle dynamics

As mentioned earlier in this chapter, the standard DPD method is a thermostat and can only simulate constant temperature situations. For non-isothermal processes involving polymers, such as heating a polymer through its volume phase transition[65, 71] or flow of micelles through a temperature gradient[72], the ability to model local variations of temperature is important. To this end, Espanol[56] introduced the internal energy of a DPD bead as an additional degree of freedom. The energy conservation equations in the eDPD are given as:

$$\frac{d(mC_v T_i)}{dt} = \Sigma_{i\neq j}\left(q_{ij}^C + q_{ij}^V + q_{ij}^R\right), \tag{2.10}$$

$$q_{ij}^C = k_{ij} w_{CT}(r_{ij})\left(\frac{1}{T_i} - \frac{1}{T_j}\right), \tag{2.11}$$

$$q_{ij}^V = \frac{1}{2C_v}\left(w_D(r_{ij})\left[\gamma_{ij}\left(\boldsymbol{e_{ij}}.\boldsymbol{v_{ij}}\right)^2 - \frac{(\sigma_{ij})^2}{m}\right] - \sigma_{ij} w_R(r_{ij})\left(\boldsymbol{e_{ij}}.\boldsymbol{v_{ij}}\right)\zeta_{ij}\right), \tag{2.12}$$

$$q_{ij}^R = \beta_{ij} w_{RT}(r_{ij}) dt^{-\frac{1}{2}} \zeta_{ij}^e, \tag{2.13}$$

where $C_v$ is the heat capacity of each eDPD bead with temperature $T_i$. The collisional ($q_{ij}^C$) and random ($q_{ij}^R$) heat fluxes together account for conduction of heat through the material. The viscous heat flux $\left(q_{ij}^V\right)$ accounts for viscous heating due to conversion of the particle's mechanical energy to heat. The strengths of the collisional and random heat fluxes $k_{ij}$ and $\beta_{ij}$ are given as $k_{ij} = C_v^2 \kappa\left(T_i + T_j\right)^2 / 4k_B$ and $\beta_{ij}^2 = 2k_B k_{ij}$, where $\kappa$ is a mesoscopic heat friction parameter. We

choose the typical form[56, 57] of the weighting functions in the collisional and random forces as $w_{CT}(r_{ij}) = w_{RT}^2(r_{ij}) = \left(1 - \frac{r_{ij}}{r_c}\right)^2$.

The introduction of energy conservation leads to some modifications to the momentum conservation equations of the standard DPD method. The momentum conservation equations for eDPD have the following temperature dependent parameters:

$$a_{ij} = A_{ij}.\frac{k_B(T_i + T_j)}{2}, \tag{2.14}$$

$$\sigma_{ij}^2 = \frac{4\gamma_{ij}k_B T_i T_j}{T_i + T_j}. \tag{2.15}$$

The strength of the conservative force $a_{ij}$ can have an additional temperature dependence prescribed through the $A_{ij}$ parameter. The function $A_{ij} = A_{ij}^* + \Delta A/(1 + \exp(\pm\omega(T_{ij} - T_0)))$ has been used previously to model LCST and UCST type polymers[65, 72]. To model temperature dependence of system properties such as the diffusivity and viscosity, the weight functions $w_D$ and $w_R$ are also chosen to be temperature dependent via the exponent $s$,

$$w_D = w_R^2 = \left(1 - \frac{r}{r_c}\right)^s, \tag{2.16}$$

The exact form of this temperature dependence and the resulting variations in system properties are discussed in more details in chapter six.

### 2.4 Integrating the dynamic equations and visualizing simulation results

One of the advantages of DPD is the ability to handle larger simulation timesteps. To further enhance this capability, Groot and Warren[58] proposed a modified form of the popular velocity-Verlet algorithm[73],

$$\boldsymbol{r}_i(t + \Delta t) = \boldsymbol{r}_i(t) + \Delta t\boldsymbol{v}_i(t) + \frac{1}{2}(\Delta t^2)\boldsymbol{f}_i(t), \tag{2.17}$$

$$\tilde{\boldsymbol{v}}_i(t+\Delta t) = \boldsymbol{v}_i(t) + \lambda \Delta t \boldsymbol{f}_i(t), \tag{2.18}$$

$$\boldsymbol{f}_i(t+\Delta t) = \boldsymbol{f}_i\big(r(t+\Delta t), \tilde{\boldsymbol{v}}_i(t+\Delta t)\big), \tag{2.19}$$

$$\boldsymbol{v}_i(t+\Delta t) = \boldsymbol{v}_i(t) + \frac{1}{2}\Delta t(\boldsymbol{f}_i(t) + \boldsymbol{f}_i(t+\Delta t). \tag{2.20}$$

We use the standard velocity-Verlet algorithm which can be recovered by setting $\lambda = 0.5$ in the above scheme. Other integration schemes have also been proposed for DPD[74].

We use the LAMMPS open-source simulation package[75-77] along with the corresponding code for mSRP[62] and eDPD[57] to integrate the momentum and energy conservation equations. All visualizations of the simulations are performed using the Visual Molecular Dynamics (VMD) software[78]. In addition to the methodology described above, the stochastic approach used to simulate the bond breaking reaction during controlled degradation is described in chapter three. Dr. Chandan K. Choudhury is acknowledged for providing the initial data to conduct simulations provided in Fig. 2.3.

# CHAPTER THREE

## Implementation of a stochastic approach within the DPD framework for simulating controlled degradation with mSRP

In chapter two we discussed the general mesoscale details of the DPD framework used in this dissertation. In the current chapter we will introduce the stochastic approach used in this work to simulate bond breaking during the controlled degradation reaction. In developing this framework, several things need to be considered. Firstly, the framework should reproduce degradation reaction kinetics. In this regard, it should be noted that several degradation reactions in polymers follow either first order[79] or pseudo first order[8, 20, 26] reaction kinetics. Hence, we aim to use a framework that reproduces first order kinetics. Further, the use of mSRP, as described in chapter two, requires additional repulsive interactions between bonds. These interactions need to be switched off as bond breaking occurs. Additionally, the dependence of degradation reaction kinetics on local material properties, such as the local temperature need to be incorporated into the framework.

In what follows, we will first introduce the basic stochastic protocol for simulating the degradation reaction with a rate constant independent of local properties. Next, we will discuss the implications of bond breaking on the mSRP approach and provide a modified mSRP implementation to allow for switching off the additional repulsion from a bond after it breaks. In the last section, we will describe modifications to the stochastic approach that incorporate dependence of the reaction rate on local temperature during the reaction.

### 3.1 The stochastic approach for modeling degradation reactions

Chemical reactions, either bond formation or bond breaking reactions in polymeric systems are often simulated within DPD as stochastic processes[46-51]. Similarly, such protocols are also used in coarse-grained MD simulations[80, 81] of polymers. To implement such a framework, the probability of bond breaking $P$, and the reaction time step $\tau_R$, need to be defined. Within this framework, the possibility of reaction is evaluated every $\tau_R$ which, in DPD simulations, is commonly chosen to be $\tau_R = 10\Delta t$ [46, 47, 49-52]. To evaluate the reaction probability, at each of the reaction timesteps, a random number is generated for each of the "degradable" bonds; the reaction is allowed to happen for a certain bond only if the generated random number for that bond is lower than $P$. A first order degradation reaction can be simulated by simply setting appropriate values for $P$ and $\tau_R$. Details of the resulting degradation reaction kinetics are provided below.

### 3.2 Handling topology violations along with chemical reactions

The mSRP approach described in chapter two was developed for polymers with a fixed topology, i.e. polymeric systems without chemical reactions. In order to model the degradation reaction, the mSRP interaction for a bond needs to be switched off as soon as the bond breaks. We recently assimilated this ability with the existing mSRP framework and implemented it as part of the LAMMPS simulation software[75-77]. To implement the mSRP framework within LAMMPS, Sirk et. al.[62, 82] introduced pseudo beads at the location of the bonds to introduce the inter-bond mSRP repulsion. Each psuedo bead only experiences the mSRP repulsive force (equation 2.9) from other pseudo beads and has no interaction with any other bead. Hence, to deactivate the mSRP repulsion upon bond breaking, we introduced the ability to delete pseudo beads via the pair style srp/react command in LAMMPS[70, 83, 84]. A schematic of the bond breaking mechanism

along with the pseudo beads for mSRP interaction is shown in Fig. 3.1 below. In addition to the bond breaking reaction, the mSRP framework is also useful for bond formation reactions. Hence, our implemented pair style srp/react command in LAMMPS also enables insertion of pseudo beads when a bond formation reaction occurs and this functionality was utilized recently in our lab for simulation of crosslinking via the hydrosilylation reaction during synthesis of polymer derived ceramics[85]. Specific details of the LAMMPS implementation, along with the relevant C++ code is provided in the Appendix A.

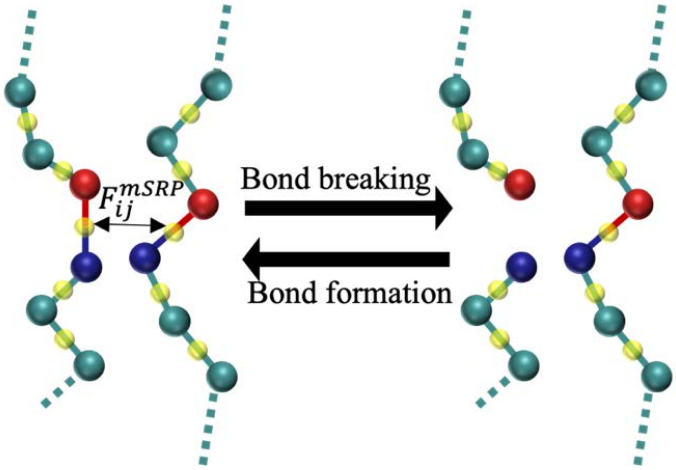


**Figure 3.1:** Schematic of the bond breaking and formation mechanism highlighting the role of mSRP pseudo beads (shown in yellow). When a bond is broken, the corresponding pseudo bead is deleted.

### 3.3 Kinetics of the degradation reaction

In this dissertation, we use the approach described above to simulate the degradation reaction in polymer networks and melts. To analyze the reaction kinetics resulting from the use of the approach described above, we first simulated degradation of nanogel particles[84] suspended in a single solvent. All relevant details about the setup of the nanogel system along with analysis

of the degradation process of nanogels is provided in chapter five. Here, we will use this system only for the specific purpose of analyzing the degradation reaction kinetics. As a result of using the approach described above, the first-order degradation rate constant ($k$) in these simulations is a function of $P$ and $\tau_r$ as [70, 84] $k = P/\tau_R$. The fraction of degradable bonds intact, $p$, provides a measure of the progress of the degradation reaction and follows the relation $p = \exp(-kt)$ expected for first order reaction kinetics. We conducted several simulations by varying $P$ and $\tau_{R,}$ effectively varying $k$, and the evolution of fraction of degradable bonds intact for these simulations is plotted in Fig. 3.2a below. Results from the DPD simulations, represented by symbols in Fig. 3.2a, are reported as average measurements from five independent simulations with error bars representing standard deviation. We used several combinations of P and $\tau_r$ values[84] as is shown in Fig. 3.2b. Solid lines in Fig. 3.2a represent the analytical plot of $p = \exp(-kt)$. The simulations reproduce first order reaction kinetics for all tested parameter sets with the rate constant given as $k = P/\tau_R$; no fitting of the rate constant is required.

### 3.4 Introducing local temperature dependence of the degradation reaction rate

In addition to the framework described so far, we aim in this dissertation to introduce the initial framework to incorporate effects of the local environment on the degradation reaction. In general, kinetics of the degradation reaction depend on the local environment such as temperature

or pH in the vicinity of the degradable bond. The dependence of reaction rate constant on local properties is represented mathematically by the Arrhenius relation:

$$k = k_0 \exp\left(-\frac{E_a}{RT}\right), \tag{3.1}$$

where $k_0$ is a pre-exponential factor, $E_a$ is the activation energy for the reaction, $R$ is the universal gas constant and, $T$ the local temperature.

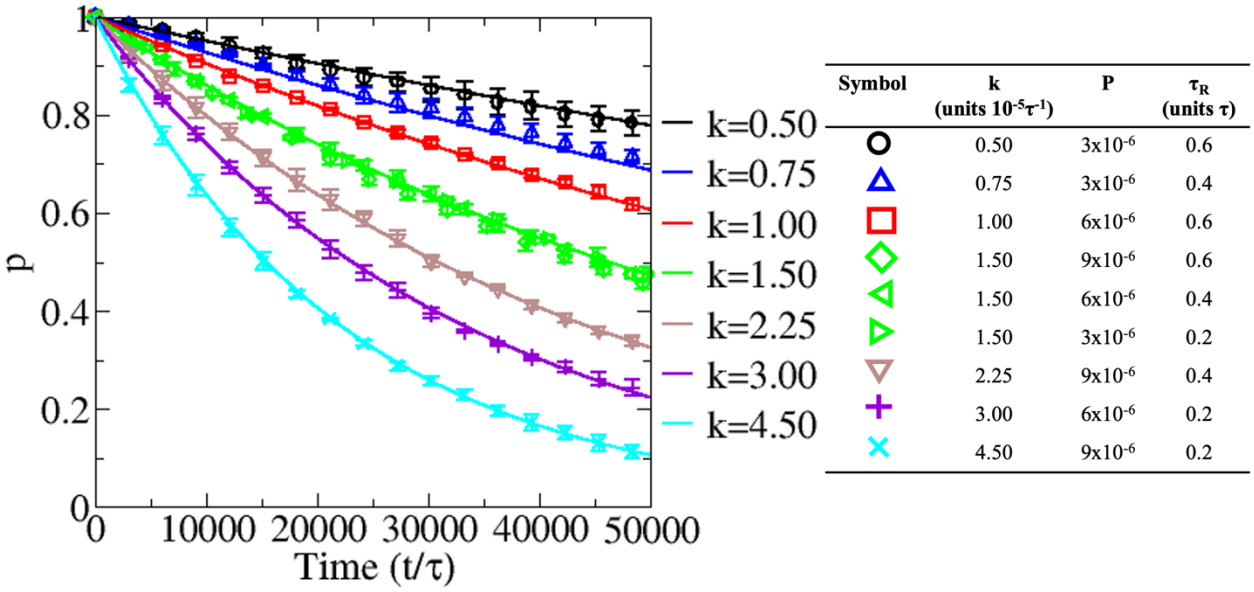


| Symbol | k (units $10^{-5}\tau^{-1}$) | P | $\tau_R$ (units $\tau$) |
|---|---|---|---|
| ○ | 0.50 | $3\times10^{-6}$ | 0.6 |
| △ | 0.75 | $3\times10^{-6}$ | 0.4 |
| □ | 1.00 | $6\times10^{-6}$ | 0.6 |
| ◇ | 1.50 | $9\times10^{-6}$ | 0.6 |
| ◁ | 1.50 | $6\times10^{-6}$ | 0.4 |
| ▷ | 1.50 | $3\times10^{-6}$ | 0.2 |
| ▽ | 2.25 | $9\times10^{-6}$ | 0.4 |
| + | 3.00 | $6\times10^{-6}$ | 0.2 |
| × | 4.50 | $9\times10^{-6}$ | 0.2 |

**Figure 3.2:** (**a**) Evolution of the fraction of bonds intact as a function of time. Symbols represent average measurements over five DPD simulations with error bars representing standard deviations. Lines represent the function $p = \exp(-kt)$, with $k = P/\tau_R$ provided in the legend in the units of $10^{-5}\tau^{-1}$. Table on the right contains a list of $P$ and $\tau_R$ values for each simulation in the figure. Figure reproduced from ref. [84] with permission from Springer Nature.

While the temperature dependence is explicit in equation (3.1), other material properties such as the local pH alter the activation energy of the reaction, thereby affecting the overall kinetics. With this context, we introduce the temperature dependence described in equation (3.1) into the degradation framework by modifying the reaction probability $P$, to depend on the local temperature as:

$$P = P_0 \exp\left(-\frac{E_a}{RT_l}\right), \tag{3.2}$$

where $T_l$ is the local temperature at the reaction site $T_l = \frac{(T_i+T_j)}{2}$, $T_i$ and $T_j$ is the eDPD temperature of bead $i$ and $j$, respectively. The above dependence of the reaction probability is used in chapter six to simulate local temperature dependent thermal degradation in polyolefin melts.

# CHAPTER FOUR

# Mesoscale modeling of controlled degradation and erosion in hydrogel films

## 4.1 Introduction

Controlled degradation of polymer networks plays a vital role in a variety of applications ranging from the design of degradable thermoset polymers[1] to controlled delivery of drugs and biomolecules[3-5] and regulating growth of neural networks[7]. Of a particular interest is photo-controlled degradation, which permits spatially-resolved dynamic control of physical and chemical properties of the materials[10-16]. Notably, in a number of the above applications, either the characteristic features of degradable gels[7, 10, 12] or the dimensions of the entire degradable gel particle[5] range between nanometers to microns, the length scales referred to as mesoscopic. While analytical models and continuum approaches[8, 9, 20, 29-32] inform our current understanding of hydrogel degradation, an understanding of degradation and erosion at the mesoscale to date is exceptionally limited despite of the relevance of this length scale to a plethora of applications.

The term degradation commonly refers to the reaction that cleaves covalent bonds, while erosion refers to the mass loss that accompanies degradation[8, 9]. Correspondingly, the polymer network undergoing degradation is often characterized by the mass loss capturing erosion processes[1, 8, 19, 86], and by the reverse gel point[1, 8, 19, 20] capturing the critical extent of degradation reaction. Similar to the gel point, which is defined as a critical point of formation of an infinite percolating network during gelation[87], the reverse gel point is a critical point corresponding to the disappearance of the percolating network[1, 8, 19] . This point is characterized by a critical value of the reaction conversion; the term reverse gel point is sometimes

used interchangeably with gel point[8] when describing degradation process. Notably, the disappearance of the percolating network at the reverse gel point results in a sudden drop in the mass of the polymer[8, 19].

To capture the polymer network degradation and erosion at the mesoscale, diffusion of all the network fragments along with reaction kinetics, hydrodynamic interactions, and network topology and heterogeneities need to be taken into account. We use Dissipative Particle Dynamics (DPD)[33-35] to model these complex systems. DPD is a mesoscale approach utilizing soft repulsive interactions between the beads representing clusters of atoms; this approach has been widely used to model variety of complex systems[35-44], including dynamics of hydrogels in various environments[51, 52, 60, 68, 88-93]. To overcome unphysical topological crossings of bonded polymer chains, we recently adapted a modified Segmental Repulsive Potential (mSRP) formulation[45] to model gels with degradable bonds[84]. More details of this implementation approach are provided in chapter three and appendix A of this dissertation.

As mentioned in chapter one, for a model hydrogel network, we focus on hydrogels formed by the end-linking of four-arm polyethylene glycol macromolecular precursors[23, 24, 94], often referred to as tetra-PEG gels[19, 23, 95]. Tetra-PEG gels fabricated by Sakai *et. al.* [23] have been shown to form nearly ideal network structures exhibiting superior mechanical properties prior to degradation. The near-ideality of the tetra-PEG gels is attributed to the elimination of a large fraction of defects during synthesis provided that the stoichiometric ratio of two macromonomer precursors is equal to one and that the overlap monomer concentration is used [23]. The four-arm PEG precursors can be modified during their synthesis to enable controlled degradation. Specifically, these hydrogels can be made degradable by including photocleavable functional groups, e.g. the coumarin[24, 27] and nitrobenzyl[14, 27, 28] groups, in the close vicinity of the

end functionalities responsible for gelation[24, 26-28]. A schematic of the coumarin-based degradable tetra-PEG hydrogels synthesized with the reaction between alkyne and azide functionalities is provided above in Fig. 1.2.

In what follows, we characterize the degradation process via tracking the time evolution of distribution of network fragments. We show that the reverse gel point can be reliably calculated from the reduced weight-average and z-average degrees of polymerization of network fragments. Based on the calculated reverse gel point, we define the relative extent of reaction and show that the polydispersity and the fraction of broken-off fragments scales with the relative extent of reaction for the samples with various thicknesses and crosslink densities. Further, we characterize erosion from the swollen polymer network via tracking the apparent mass loss that accounts for the fragments remaining in contact with the percolated network. The proposed framework allows one to clearly distinguish the main features of degradation and erosion on the mesoscale. The work described in this chapter is published in the Journal of Physical Chemistry. The corresponding journal article is ref. [70] of the dissertation and the permission to reproduce this work in this chapter is included in Appendix B of this dissertation.

## 4.2 Methods

### *4.2.1 Introducing DPD formulation for tetra-PEG hydrogels*

The main features of the overall DPD approach used in this work are outlined in chapter two. Below, we go into the details of parameter choices and other specifics for modelling tetra-PEG gels using this approach. As described in chapter two, we chose $a_{ii} = 78$ (in reduced DPD units) for the interaction between beads of the same type based on the compressibility of water and our choice of coarse-graining three water molecules into one bead[36]. The repulsion parameter for the dissimilar beads is chosen based on the affinity between these beads as[34] $a_{ij} = a_{ii} +$

$3.27\chi_{ij}$, where $\chi_{ij}$ is the Flory-Huggins polymer-solvent interaction parameter. The affinity of PEG beads to water beads is set by the choice of the repulsion parameter between the polymer and water beads as $a_{pw} = 79.5$ based on the PEG-water Flory-Huggins interaction parameter [29, 96] [26, 29, 96], $\chi = 0.45$. The degradable end groups are assumed to have the same solubility as a PEG monomer and hence the same interaction parameter is used for these beads.

We also conducted a series of additional simulations tracking the dynamics of entangled polymer loops to validate the effective minimization of bond crossings[70]. In addition, we confirmed that with the chosen parameters both the bond lengths distribution and the mean-squared internal distances for beads separated by a fixed number of bonds remain largely unaffected by the mSRP potential[70]. To integrate dynamic equations, the LAMMPS simulation package[75, 77] with mSRP code[45] is used. All visualizations of the hydrogel network were performed using the Visual Molecular Dynamics (VMD) software[78]. The trajectories used for the analysis below are saved every $\Delta t_M$=5000 time steps.

*4.2.2 Parameter choices and other details for modelling the degradation reaction*

As detailed in chapter three, to simulate the bonds breaking, we use the stochastic approach, similar to that used previously for various reactive systems[52, 81, 97]. Herein, we use $\tau_R$=10$\Delta t$, similarly to the choice of reaction time step in previous DPD simulations of various reactive systems[46, 47, 49-52]. For a number of the polymer networks undergoing controlled photodegradation, the degradation rate constants are within the range of[3, 24, 25, 27, 28] $1s^{-1}$-$10^{-3}$ $s^{-1}$, i.e., the degradation occurs orders of magnitude slower than the characteristic diffusion times on the relevant length scales[84]. Hence low degradation rates are chosen in our simulations, ensuring that our system remains in a kinetically limited regime[52, 84].

*4.2.3 Construction of initial network structure*

The initial configuration of the tetra-PEG network is modeled as a diamond-like lattice[52, 98]. The choice of diamond lattice ensures junction functionality of four, corresponding to the network formed by the four-arm precursors. The centers of the tetra arm precursors are placed at the lattice sites and the precursor arms are then formed by placing $N_x/2$ beads ($N_x/2$-1 PEG beads and one end functionality bead) along the directions from each lattice site to its nearest neighbors. Thus, there are $N_x$ beads between the centers of two bonded precursors. Two neighboring end functionalities are then connected, which results in an initial unit cell of the polymer network. Hydrogel films are made by replicating the polymer unit cell and are referred to as $X$x$Y$x$Z$, where $X$, $Y$ and $Z$ denote the number of replicas in $x$, $y$ and $z$ directions, respectively. The unit cell is replicated up to the simulation box faces in $x$ and $y$ directions with beads connected across these faces (i.e, beads at the $+x$ face are connected to the beads at the $-x$ face). In the $z$ direction, the unit cell is replicated within the simulation box to allow space for swelling. Mere repetition (without bonding across the periodic box) of the unit cell results in precursors having a functionality less than four at the $z$-faces of the network. These partial precursors are deleted to yield the hydrogel film structure containing an integer number of precursors[84], however such deletion results in dangling polymer chains at the z-faces. Fig. 4.1a shows a part of this initial network structure prior to the network equilibration. PEG beads and the end groups of both precursors are shown in cyan, red, and blue, respectively, and the water beads are shown as points in Fig. 4.1a for clarity of representation. The bond between the end functionalities is set to be degradable corresponding to a cleavable site typically located in the proximity of the end functionality[24, 26]. While herein we focus solely on a tetra-functional polymer network, it is worth noting that both the network

connectivity and a fraction of degradable bonds can be readily tailored during the hydrogel synthesis[26, 94, 99], for example by using linear linkers of various lengths[99] or by using star-shaped precursors[100]. The corresponding variations in the network architecture prior to degradation can potentially be translated into the DPD framework in a straightforward manner by choosing different functionalities of the network junctions and specifying corresponding degradable bonds for each system of interest.

**Table 4.1:** Simulation parameters sets for initial hydrogel films used in this work.

| Parameter set | $N_x$ | Unit cell repeats | Beads in one precursor | Total polymer beads | Tetra arm precursors ($N_0$) | Degradable bonds | Simulation box size | Total water beads |
|---|---|---|---|---|---|---|---|---|
| A (ref.) | 6 | 8x8x4 | 13 | 24960 | 1920 | 3584 | 42x42x50 | 239640 |
| B | 6 | 8x8x3 | 13 | 18304 | 1408 | 2560 | 42x42x50 | 246296 |
| C | 6 | 8x8x5 | 13 | 31616 | 2432 | 4608 | 42x42x60 | 285904 |
| D | 6 | 8x8x6 | 13 | 38272 | 2944 | 5632 | 42x42x70 | 332168 |
| E | 10 | 8x8x4 | 21 | 40320 | 1920 | 3584 | 57x57x60 | 544500 |
| F | 14 | 8x8x4 | 29 | 55680 | 1920 | 3584 | 66x66x60 | 728400 |

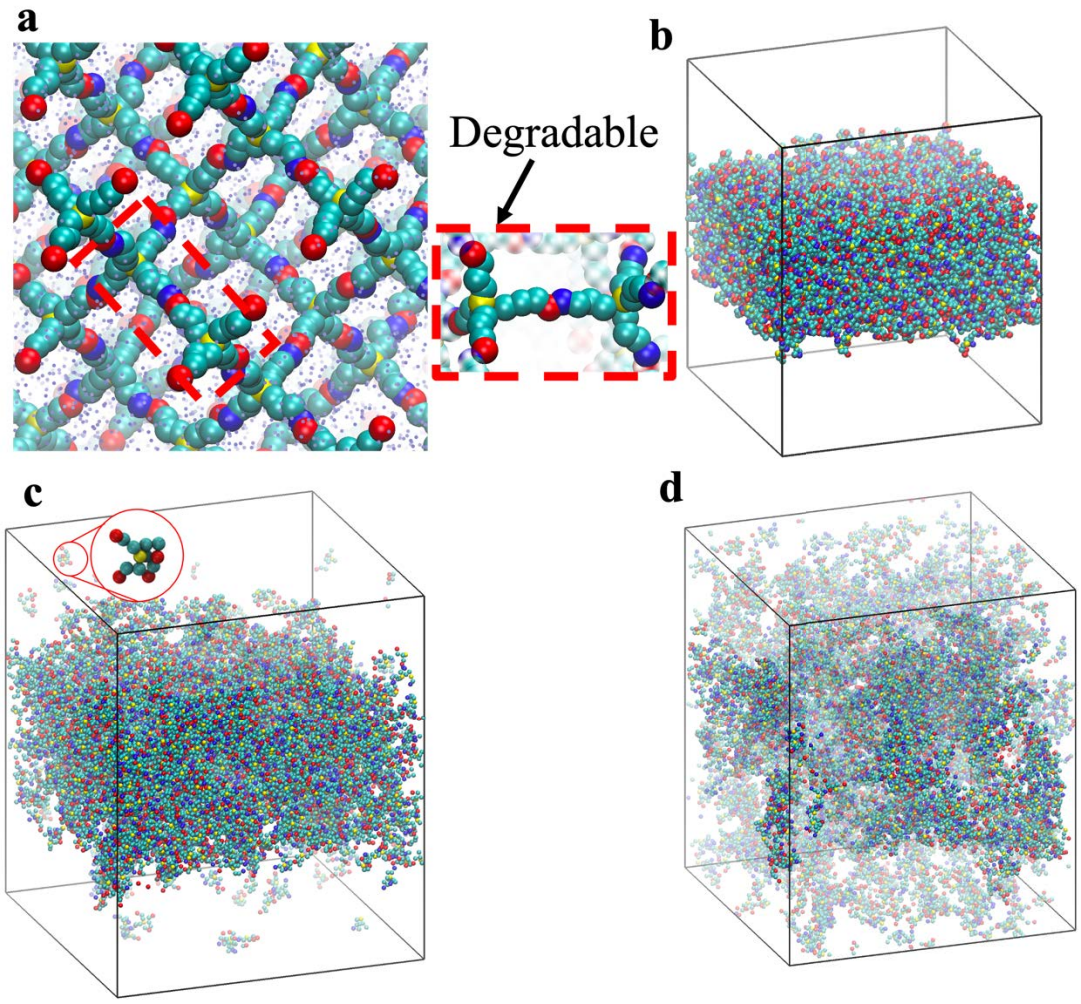


**Figure 4.1.** (**a**) A fragment of polymer network with degradable bonds (bonds between red and blue beads), initial configuration prior to equilibration. Tetra-functional centers and PEG beads are shown in yellow and cyan, respectively, and water beads are shown as blue dots. **(b-d)** Snapshots of degradation of a reference hydrogel film (parameters set A in Table 4.1) with the degradation rate $k = 4.5 \cdot 10^{-5}$ at $t = 0$ in (b), $t = 10{,}000$ in (c), and $t = 20{,}000$ in (d). The largest connected cluster is highlighted in each snapshot, remaining polymer beads are shown as translucent and in less saturated color. Water beads are hidden for visual clarity.

All parameters used for creating the initial polymer networks in this work are listed in Table 4.1 below. The simulation box size for films with higher $N_x$ was increased in horizontal direction to ensure free swelling. Additionally, the box size was increased in $z$-direction for films with higher $N_x$ or larger thickness to ensure sufficient swelling and accurate calculation of clusters.

## 4.3 Results and Discussion

### *4.3.1 Clusters distribution and reverse gel point*

In the first series of simulations, we characterize the dynamics of the degradation process of the swollen network. The film is equilibrated prior to degradation as detailed in our work in refs. [68, 70]. Fig. 4.1b shows the equilibrated hydrogel film prior to degradation. The affinity of PEG beads to water beads is chosen based on the PEG-water Flory-Huggins interaction parameter (See section 4.2 above). Snapshots in Fig. 4.1b-d illustrate the process of degradation and erosion of the hydrogel film. After the degradation begins (for example, after switching the light on for a photodegradable network), degradable bonds break according to the degradation rate constant, $k$. As a result, fragments break off from the film and are shown as translucent and in less saturated color in Fig. 4.1c,d; water beads are not shown for clarity.

To track the degradation process, we first define a topological cluster as a group of bonded beads; correspondingly, the cluster size is defined as the number of tetra-arm precursors within the cluster. Prior to the degradation, there is a single topological cluster encompassing all the precursors within the hydrogel matrix. Evolution of both the size of the largest cluster, $N_T(t)$ (black curve, left axis) and the total number of clusters during degradation (red curve, right axis) is shown in Fig. 4.2a. At early times, relatively small fragments leave the hydrogel, while the size of the largest cluster does not change significantly. This is evident from the simulation snapshot in Fig. 4.1c and the corresponding distribution of cluster sizes in Fig. 4.2b. Specifically, along with

the large number of smaller fragments, only one large cluster corresponding to the degrading hydrogel film exists in the system (inset in Fig. 4.2b). Overall, the small clusters dominate the distribution throughout the degradation process (see all distributions in Fig. 4.2b-d). As seen in the snapshot Fig. 4.1c, several of these small clusters leave the hydrogel film and are dispersed in the surrounding solvent, contributing to an overall mass loss.

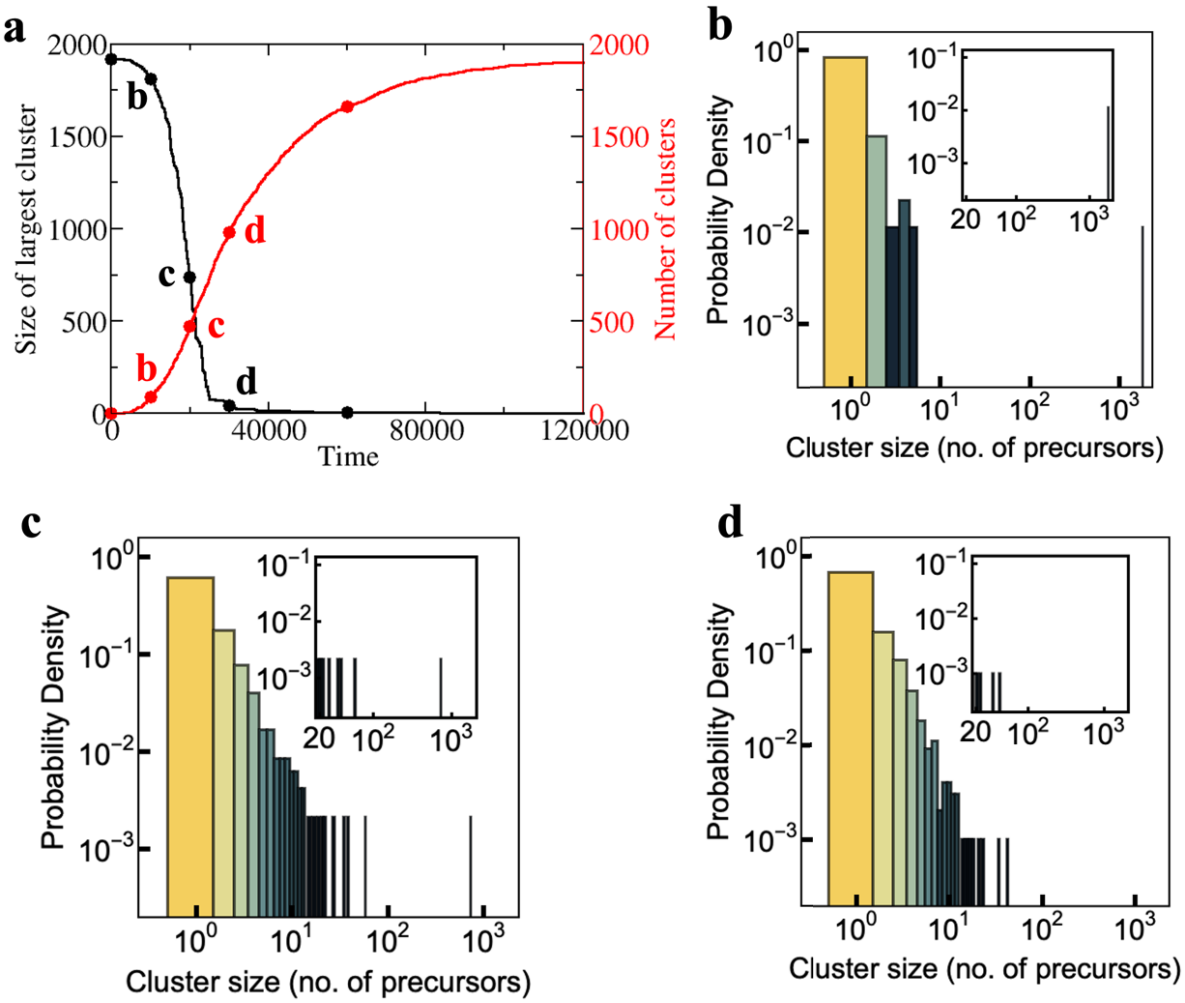


**Figure 4.2. (a)** Evolution of the size of the largest cluster (in black) and number of clusters in the system (in red) for the degradation simulation shown in Fig. 4.1. **(b-d)** Distribution of cluster sizes at time instants t=10,000 in (b), t=20,000 in (c), and t=30,000 in (d), the same time instants are

marked in (a). Insets in (b-d) highlight the distributions of clusters with large number of precursors (>20 precursors).

Notably, this topological characterization does not allow to distinguish between the smaller fragments leaving the film and the fragments that broke off but remain within the film and hence do not contribute to the mass loss. Additional characterization needed to quantify mass loss and erosion is detailed below. As degradation proceeds, multiple larger clusters appear in the system (Fig. 4.1d), while the size of the largest cluster sharply decreases (Fig. 4.2a). During this sharp decrease the percolating hydrogel network vanishes; beyond the reverse gel point, the largest cluster no longer represents the original degrading film. The existence of many relatively small clusters at late times is evident from the distributions in Fig. 4.2c,d. Correspondingly, the largest cluster in the snapshot in Fig. 4.1d (shown in more vivid color and seen through some of the translucent beads representing smaller clusters) is indeed relatively small and consists of only 736 precursors (or 38.33% of the total number of precursors). As degradation continues, the larger clusters disintegrate into smaller clusters and eventually into the single precursors.

To characterize the degradation process quantitatively, we carried out five independent simulations each at three different degradation rates. The averaged results from these simulations are summarized in Fig. 4.3, where all error bars denote standard deviation over five independent simulations. To characterize reverse gelation, we use measurements similar to those that have been used to characterize gelation[87, 101-105]. Accordingly, the weight average degree of polymerization, $DP_w$, is defined at each moment in time as $DP_w(t) = \frac{\Sigma n_i(t) i^2}{\Sigma n_i(t) i}$ , where $i$ is the number of beads in a cluster, $n_i(t)$ is the number of clusters with $i$ beads at time $t$, and summation is taken over all the clusters. The values of $DP_w$ (Fig. 4.3a) are high at early times corresponding

to the existence of the percolating network. After an initial slow decrease, there is a sudden drop in $DP_w$, which is delayed at lower degradation rates since longer time is needed to break the same number of bonds.

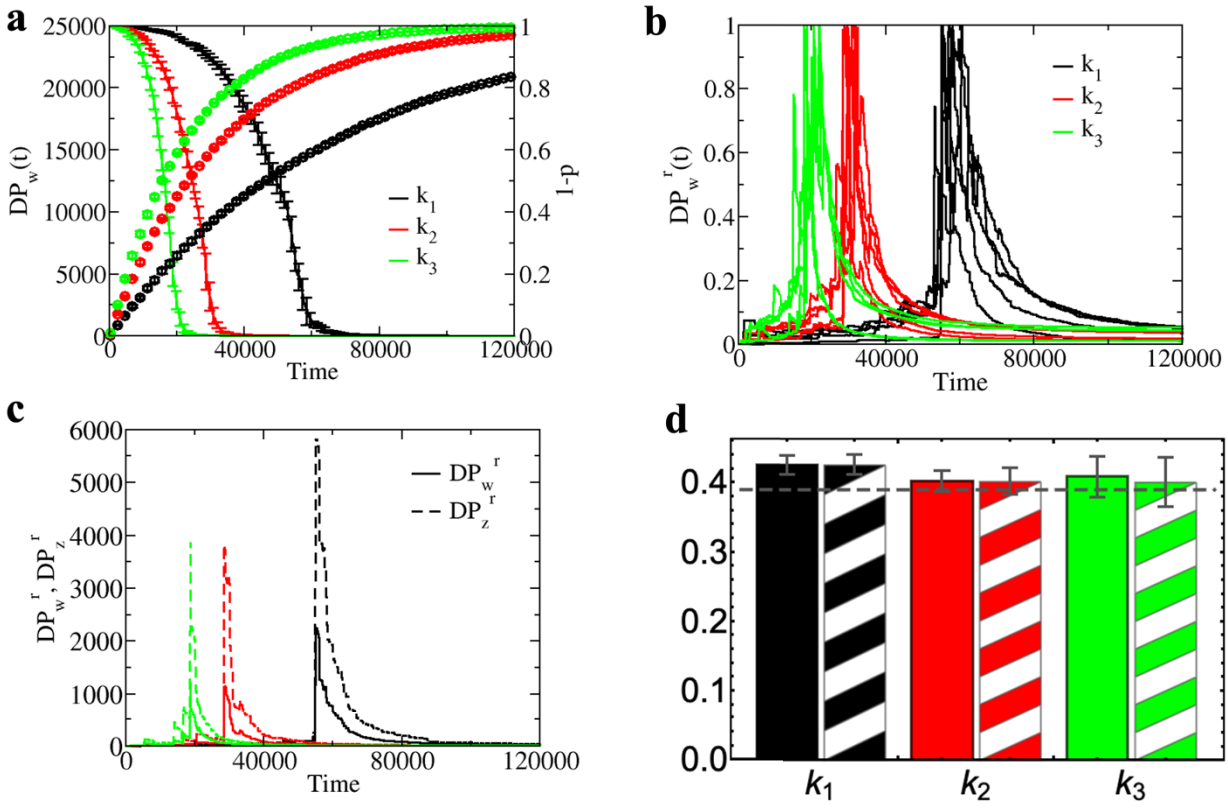


**Figure 4.3.** Time evolution of **(a)** weight average degree of polymerization, $DP_w$(left axis) and fraction of bonds broken, 1-p, (right axis), **(b)** normalized reduced $DP_w^r$ for 5 independent simulations for each degradation rate, and **(c)** reduced z-average degree of polymerization, $DP_z^r$ , and $DP_w^r$ for a single simulation run for each degradation rate. **(d)** Measured reverse gel points $p_c^w$ (solid bars) and $p_c^z$ (striped bars). Each curve in (**a**) and each data point in (**d**) represent average over 5 independent simulations, error bars represent the standard deviation. Each curve in (**b**) and (**c**) represents a single simulation and the data in (b) is normalized by the maximum value in each simulation. Gel film with $N_x = 6$ and reference parameters set (set A) is considered. Black, red, and green colors in (a)-(d) correspond to degradation rates $k_1 = 1.5x10^{-5}$, $k_2 = 3.0x10^{-5}$,

and $k_3 = 4.5\ x10^{-5}$, respectively. These rates were obtained by setting $P = 3x10^{-6}$, $6x10^{-6}$ and, $9x10^{-6}$ with $\tau_R = 0.2$. The degradation rate constants are provided in units of reduced simulation time, $\tau^{-1}$.

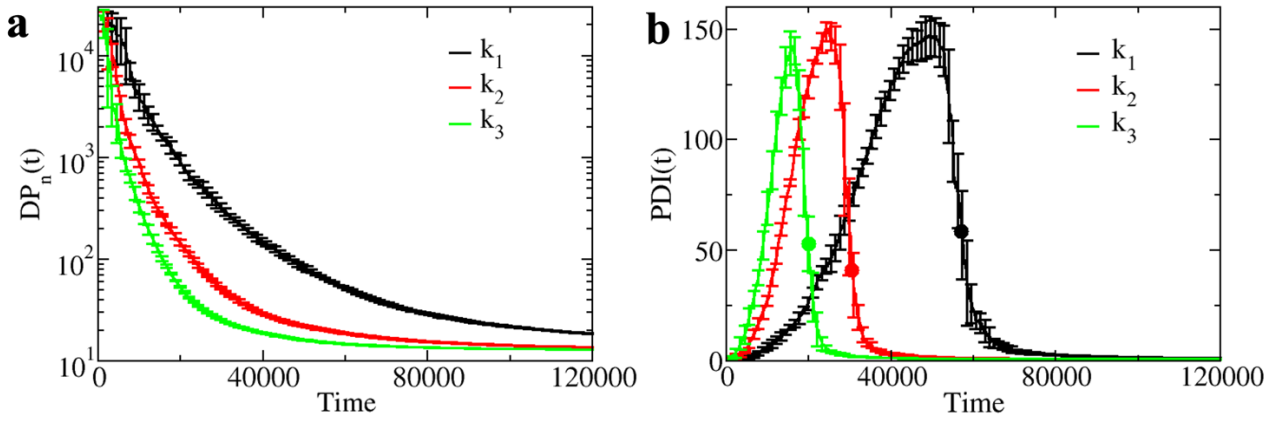


**Figure 4.4.** Time evolution of **(a)** number-average degree of polymerization, $DP_n$, and **(b)** polydispersity index, PDI. Each curve represents an average over 5 independent simulations, error bars represent the standard deviation. The colors have the same meaning as in Fig. 4.3 above

The fraction of the bonds broken in the same systems, $1 - p(t)$, is shown on the right axis in Fig. 4.3a; this value ranges from zero to one and represents an extent of the degradation reaction. While $DP_w$ diverges at the gel point in analytical gelation theories[87, 104, 105], it remains finite throughout simulations of finite size systems during gelation[106] or reverse gelation. Thus, to identify the reverse gel point in our finite-size simulations, we use the reduced weight average degree of polymerization, $DP_w^r$, defined as

$$DP_w^r(t) = \frac{\Sigma' n_i(t) i^2}{\Sigma' n_i(t) i}\ , \tag{4.1}$$

where the summation is taken over all the clusters excluding the largest cluster.

The reduced weight average degree of polymerization exhibits a peak at the gel point during the gelation process in finite size systems[101-103, 107]. The curves of the same color in Fig. 4.3b correspond to five independent simulation runs for each degradation rate $k$, and are normalized by the highest value of the $DP_w^r$ in each independent simulation. At the initial stages of degradation, $DP_w^r$ has a low value since the gel constitutes the only large cluster in the system. As degradation proceeds, $DP_w^r$ exhibits a peak similar to that observed at the gel point in simulations of gelation[101-103, 108]. This peak corresponds to the disintegration of the percolating network. The time instant corresponding to peaks in $DP_w^r$, $t_c^w$, allows us to identify a reverse gel point by calculating the corresponding critical value of the fraction of degradable bonds intact as

$$p_c^w = \exp(-kt_c^w). \tag{4.2}$$

Alternatively, reverse gel point can be identified from the analysis of the z-average degree of polymerization, $DP_z(t) = \frac{\Sigma n_i(t) i^3}{\Sigma n_i(t) i^2}$. $DP_z$, similar to $DP_w$ , diverges at gel point according to the analytical theories of *gelation*[87, 105]. In our finite size simulations, $DP_z(t)$ shows a behavior similar to the $DP_w$, although it decreases slower than $DP_w$. Using analogous arguments as for $DP_w^r$, we define the reduced z-average degree of polymerization, $DP_z^r$, at each time instant as:

$$DP_z^r(t) = \frac{\Sigma' n_i(t) i^3}{\Sigma' n_i(t) i^2}, \tag{4.3}$$

where the summation is taken over all the clusters excluding the largest cluster. The $DP_z^r$ curves for one representative simulation each at the three degradation rates are plotted along with the corresponding $DP_w^r$ curves in Fig. 4.3c. The time corresponding to the peak in $DP_z^r$, $t_c^z$, provides a second measurement of the critical conversion at the reverse gel point $p_c^z = \exp(-kt_c^z)$. Note that the peak value of $DP_z^r$ is higher than that of $DP_w^r$. The values of $p_c^w$ and $p_c^z$ obtained from the

positions of the peaks in Fig. 4.3b,c (averaged over 5 runs for each degradation rate) are provided in Fig. 4.3d. These results show that either measurement, $p_c^w$ or $p_c^z$, can be used to accurately identify the reverse gel point. An increase in standard deviation for the highest degradation rate constant can be attributed to the fact that the data is sampled for the analysis every 5000 time steps ($\Delta t_M$, see section 4.2) for all three cases; hence the deviations at the higher reaction rates can potentially be reduced at the cost of increased computation time if the data is sampled more often.

Note that our measured reverse gel point is significantly higher than the value predicted by the mean-field theories for the gel point of tetra-functional networks[104, 105] ($p_c = 0.33$). This could be attributed to the significant difference between the initial network structure prior to the degradation and Bethe lattice postulated in the mean-field models. The assumption of absence of any intramolecular connections used in these mean-field theories is not expected to hold for networks, since existence of intramolecular connections is an essential characteristic of any network architecture.[109] Recall that the initial structure in our simulations corresponds to a diamond-like lattice. Hence, the percolation problem closest to our simulations is that of bond percolation on a diamond lattice[110], which predicts $p_c = 0.39$ for the gelation problem (marked by the dashed line in Fig. 4.3d). Notably, the measured reverse gel points in Fig. 4.3d are somewhat higher than the theoretical limit of $p_c = 0.39$ corresponding to an infinite network. This could be attributed to the finite network size and is consistent with prior studies of gelation in finite-size network, where the gel point was shown to increase with the decrease in total number of macromers forming the network with respect to the gelation point of the infinite network[106, 110].

In experiments, values close to the diamond lattice percolation problem have been observed for the gelation of tetra-arm PEG precursors near the overlap concentration [111, 112], while

higher values were observed at lower concentrations. A delay in gel point is often attributed to an increased tendency of intramolecular reactions[107, 109, 113-116]. Recent work by Lang et. al.[117] suggests that such attribution may not be sufficient as the gel point delay is not fully explained by intramolecular reactions. A number of recent studies on gelation, both computational and experimental, are surveyed by Lang *et. al.* in the same publication[117]. In contrast to the numerous publications focusing on characterizing gelation process, analysis of the kinetics of controlled network degradation along with measurement of reverse gel point, specifically for the systems formed by two tetra-arm precursors (often referred to as A4B4 network), is exceptionally limited. Li et. al.[26] had reported a reverse gel point ranging within 0.43 to 0.48 for the tetra-PEG networks formed at a fixed polymer concentration but with various stochiometric ratios. In the latter work, the authors argued that their observed reverse gel points[26] are close to the reverse gel points predicted by the site and bond percolation models on the diamond lattice. The diamond lattice model and corresponding reverse gel point have also been used by Reid *et. al.* in their model [118] to explain experimental data of degradation behavior of tetra-arm PEG gels.

To characterize polydispersity within the degrading system, we track the number-average degree of polymerization, $DP_n(t) = \frac{\Sigma n_i(t) i}{\Sigma i}$ (Fig. 4.4a), and a polydispersity index, $PDI(t) = \frac{DP_w(t)}{DP_n(t)}$ (Fig. 4.4b), during the degradation process. Note that PDI is also referred to as the dispersity Đ in the system. Similar to $DP_w$, $DP_n$ initially has a large value owing to the existence of the percolating network. As anticipated, $DP_n$ decreases faster compared to $DP_w$ . The $PDI$ exhibits a peak close to the reverse gel point and decreases to one at the end of the degradation process. The peak in PDI is observed prior to the disappearance of the percolating network (average value of the reverse gel point is marked by the circle of the corresponding color in Fig. 4.4b). Analogous trend was previously observed in simulations of gelation where the PDI peak was observed after

the gel point[107]. The trend in $PDI$ is also evident from the time evolution of the cluster size distributions in Fig. 4.2b-d.

*4.3.2 Fractional mass loss*

We now turn our focus onto characterizing erosion, which can be defined as the loss of material due to the fragments leaving the original matrix[8, 9]. In experiments, the fractional mass loss from the material, $f(t) = 1 - m(t)/m_0$, where $m_0$ is the initial mass of the material, and $m(t)$ is mass of the material at a time $t$ from the start of the degradation process, can be tracked during the degradation[8]. Unlike the apparent first order degradation kinetics observed in experiments[25, 26, 119], the fractional mass loss in experiments shows more complicated behavior, with early time slow mass loss followed by an accelerated mass loss attributed to reverse gelation[8, 19]. The fast mass loss can be modeled as a discontinuity at the reverse gel point where the entire hydrogel film becomes soluble and hence complete mass loss occurs ($m(t_c) = 0$).[8]

We first measure mass loss from the largest topological cluster up to the reverse gel point by measuring the mass of topological clusters that detach from the largest cluster due to bond breaking. Since the mass of all beads is the same in DPD simulations (see section 4.2), we calculate a fractional mass loss as $f_T(t) = 1 - N_T(t)/N_0$ (black curve in Fig. 4.5a, $t_c = 20{,}500$), where $N_T(t)$ is the size of the largest cluster (expressed in the number of precursors), and $N_0 = N_T(0)$ is the total number of precursors. Thus, $f_T$ denotes the fraction of polymer beads that are no longer bonded to the hydrogel film. Two mass loss regimes can be distinguished in this fractional mass loss data. A slow mass loss regime is initially observed as only small fragments leave the hydrogel network. This slow regime occurs even though a significant fraction of degradable bonds have

broken (the fraction of degradable bonds intact for the same simulation until the reverse gel point is shown in Fig. 4.5a, dashed curve).

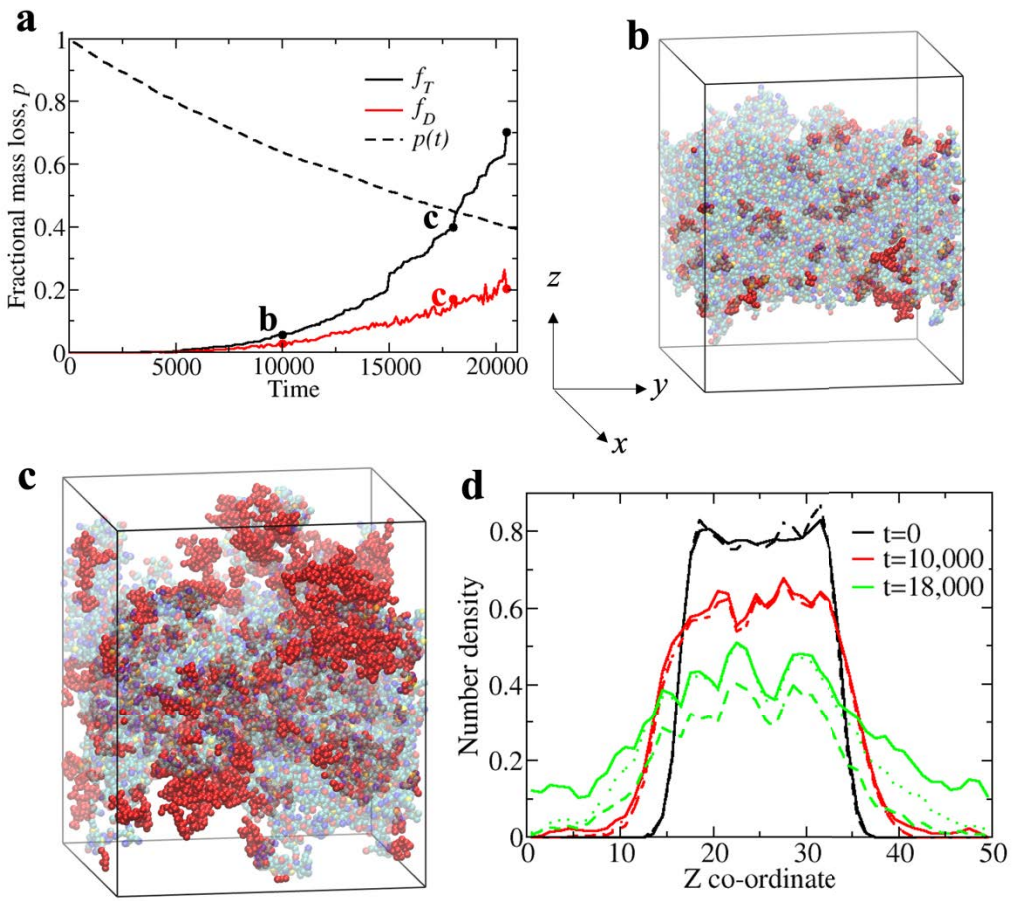


**Figure 4.5 (a)** Fractional mass loss from the largest topological cluster (black curve) and the largest agglomerate (red curve) measured up to the reverse gel point (t=20,500) for the $N_x = 6$, 8x8x4 hydrogel film, degradation rate is $k = 4.5\text{x}10^{-5}$ in dimensionless units. The dashed line represents the fraction of degradable bonds intact, *p(t)*, for the same simulation run. Snapshots of the degrading film at **(b)** t=10,000 and **(c)** t=18,000 (corresponding time instances are marked in (a)). The fragments within the interaction distance with the largest agglomerate, including the fragments that are stuck inside the film, are highlighted in red with the rest of the polymer shown as translucent. **(d)** Number density distribution of all polymer beads in vertical direction averaged

over *xy* plane (solid line), largest cluster (dashed line) and largest agglomerate (filled circles) at t=0 (black), t=10,000 (red), and t=18,000 (green).

For example, in the simulation in Fig. 4.5a, at $t = 10{,}000$ only ≈5% of the mass is lost ($f_T(t) \approx 0.05$) while ≈35% of the degradable bonds have broken (this time instant is marked by a circle (b) in Fig. 4.5a). In this regime, erosion primarily occurs from the surface where the tetra-arm precursors have lower connectivity to the film. Some precursors get detached but remain within the bulk of the largest cluster as discussed below. However, bonds breaking in the bulk primarily contribute to reduction in number of elastically active polymer strands and hence to the decrease in crosslink density and corresponding swelling of the hydrogel film, as seen in Fig. 4.1c. The initial slow mass loss from the topological largest cluster notably accelerates before the reverse gelation occurs primarily due to the detachment of larger fragments that consist of several tetra-arm precursors, as seen in Fig. 4.1d.

The above definition of $f_T(t)$ is purely topological and does not account for spatial distribution of the clusters. Consequently, it does not distinguish between the broken fragments that are no longer in contact with the film and the broken fragments that remain within the bulk or within an interaction distance from the surface of the film. Hence this definition overestimates the actual mass loss from the film. To estimate the mass loss only due to the fragments that no longer interact with the film, we define a distance-based cluster or an agglomerate as a set of beads each within $r_c$ from at least one other bead in the agglomerate. We correspondingly introduce mass loss from the largest agglomerate as: $f_D(t) = 1 - N_D(t)/N_0$, where $N_D$ is the size of the largest agglomerate (number of beads within the agglomerate normalized by the size of the precursor). The evolution of $f_D$ for our reference case is provided in Fig. 4.5a (red curve). The fragments that

remain in the bulk or at the surface of the topological largest cluster are now incorporated into the distance-based largest cluster (or agglomerate). These fragments are highlighted in dark red and shown through the hydrogel film (the film is shown as translucent) in the snapshots at t=10,000 (p=0.64) and at t=18,000 (p=0.44) in Fig. 4.5b and 4.5c, respectively. Note that reliable calculation of the agglomerate sizes requires that the simulation box size is large enough in the $z$-direction to allow space for swelling and for the detached clusters to diffuse away from the film. We chose the box size of 50 units in $z$-direction since calculation of $f_D$ for the hydrogel film with reference parameters set is independent of the box size above this value (Fig. 4.6).

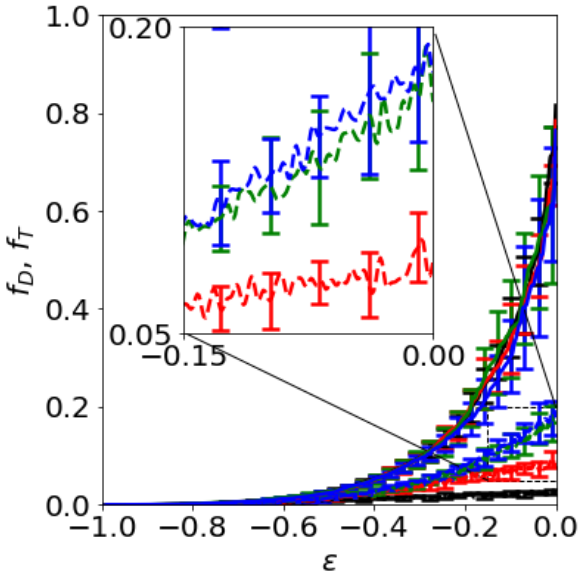


**Figure 4.6.** Comparison of $f_T$ (solid) and $f_D$ (dashed lines) during the degradation of the hydrogel film as a function of relative extent of reaction with z direction box size 30 (black), 40 (red), 50 (green) and 60 (blue) units.

To characterize the spatial distribution of clusters during erosion, we compare the number density distribution of all polymer beads in the simulation box with the distribution of those beads that form the largest topological cluster and the largest agglomerate. Before any bonds are broken,

the hydrogel film constitutes the largest cluster (both topological and distance-based). The number density of this equilibrated film along z direction (averaged over *xy* plane) is shown in black in Fig. 4.5d. The film thickness and spatial location prior to the degradation can be clearly identified from the black curve. As degradation begins, the film thickness increases due to swelling; this is seen in the density distributions at t=10,000 (red curves in Fig. 4.5, p=0.64). At this time instant (early stages of degradation), the difference between the density distribution of all polymer beads (solid line), and that of the largest topological cluster (dashed line) and largest agglomerate (circles) are minor. The distribution for the largest agglomerate closely follows that for all polymer beads (solid lines and circles) and the difference between the largest agglomerate and largest topological cluster is caused by the fragments highlighted in red in Fig. 4.5b. Quantitatively, these fragments constitute only 3.15% of the mass of the largest topological cluster at t=10,000. As the reverse gel point is approached, the relative contribution of such fragments increases to about 38.00% at t=18,000 (p=0.44, Fig. 4.5c). At this later stage of the degradation the density of the largest topological cluster within the bulk region of the film (green dashed line in Fig. 4.5d) becomes notably lower than the density of all polymer beads and the density of the largest distance-based cluster (solid and dotted green lines, respectively). The number density distribution of the largest agglomerate matches the density distribution of all polymers in the bulk region of the film (solid and dotted green lines overlap within the bulk), but attains notably higher values than that for the largest topological cluster close to film surface due to the clusters that broke off but remain within the interaction distance. Hence, $f_D$ defined above accounts for the largest topological cluster and the smaller topological clusters that are either stuck within the film or remain within the characteristic interaction distance. The latter contribution increases with time as the surface-to-volume ratio of the degrading cluster increases.

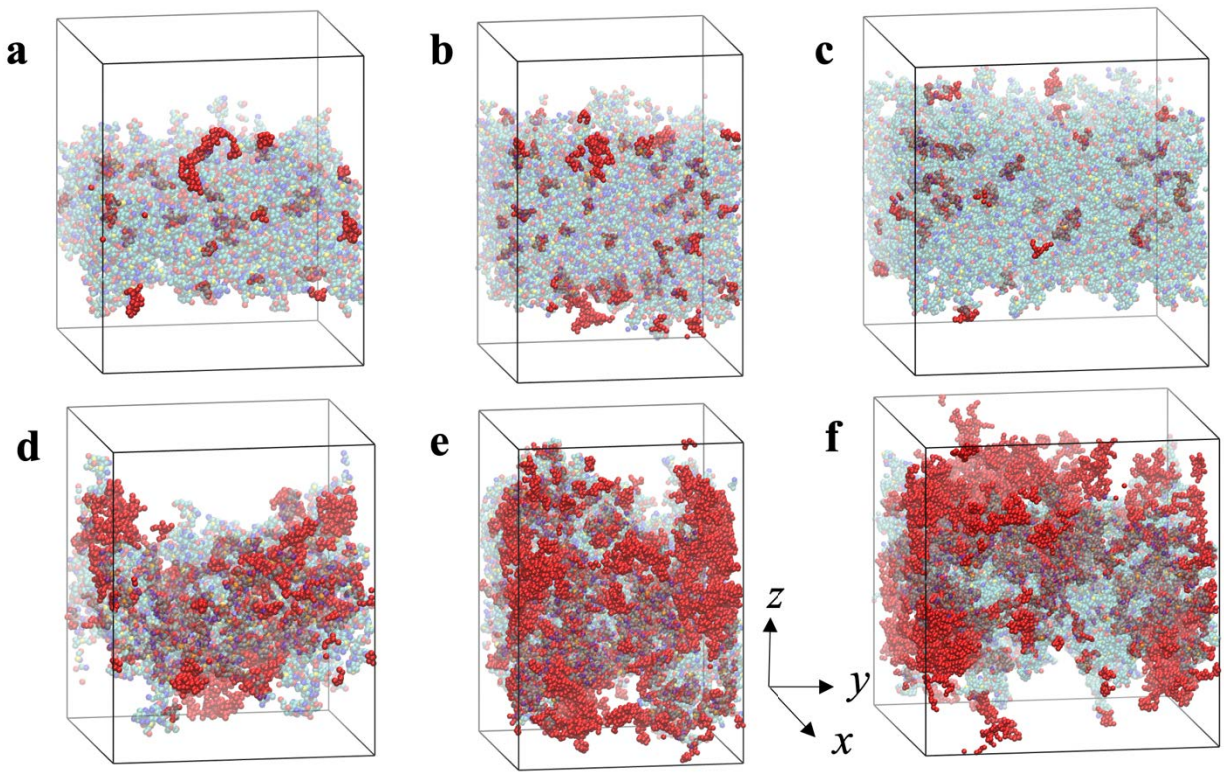


**Figure 4.7.** Snapshots of the degrading film for parameter sets B**(a,d)**, C(**b,e)** and *E***(c,f)** (see Table 4.1). Polymer fragments that either remain stuck within the percolated film or remain within the interaction distance from it are shown in red. Water beads and fragments that are no longer within the interaction distance with the film are hidden for clarity of representation. The beads representing largest topological cluster are translucent. The snapshots in the top row (a-c) are taken at t=10,000, corresponding to the fraction of degradable bonds intact p=0.64. The snapshots in the bottom row (d-f) are taken at t=18,000,corresponding to p=0.44.

*4.3.3 Effect of sample thickness and crosslink density*

Having established the essential characteristics of degradation of a hydrogel film with the reference parameters set, we now turn our attention to the effects of varying physical parameters of the polymer network, specifically film thickness and crosslink density. The detailed parameters are provided in Table 4.1 and representative snapshots during degradation are provided in Fig. 4.7. First, we varied the film thickness at a constant crosslink density ($N_x = 6$) by varying the number of unit cell repetitions in $z$-direction from three to six (parameter sets A-D). The thickness of the film prior to the degradation can be clearly seen from the number density plots in $z$-direction averaged over $x$-$y$ plane (Fig. 4.8a). Red, black, green, and blue curves in Fig. 4.8 correspond to sets A through D respectively. In the second independent series of simulations, we increased $N_x$, effectively decreasing the crosslink density while keeping the number of precursors fixed. This corresponds to parameter sets A ($N_x = 6$), E ($N_x = 10$) and F ($N_x = 14$), with corresponding data represented by black, orange, and purple curves in Fig. 4.8. Note that such an increase in $N_x$ also effectively increases the sample thickness prior to the degradation due to the more pronounced swelling at lower crosslink density. Notably, the pairs of simulations parameter sets C, E and D, F are chosen to have matching thicknesses (Fig. 4.8a) but different crosslink densities. The snapshots of the thinner and thicker films than that in the reference case during the degradation (sets B and C), and the snapshot of the sample with lower cross-link density (set E) are shown in Fig. 4.7a,d, Fig. 4.7b,e and Fig. 4.7c,f respectively. These snapshots represent relatively early stage of degradation (Fig. 4.7a-c, top row, t=10,000, p=0.64) and time instant close to the reverse gel point (Fig. 4.7d-f, bottom row, t=18,000, p=0.44), respectively.

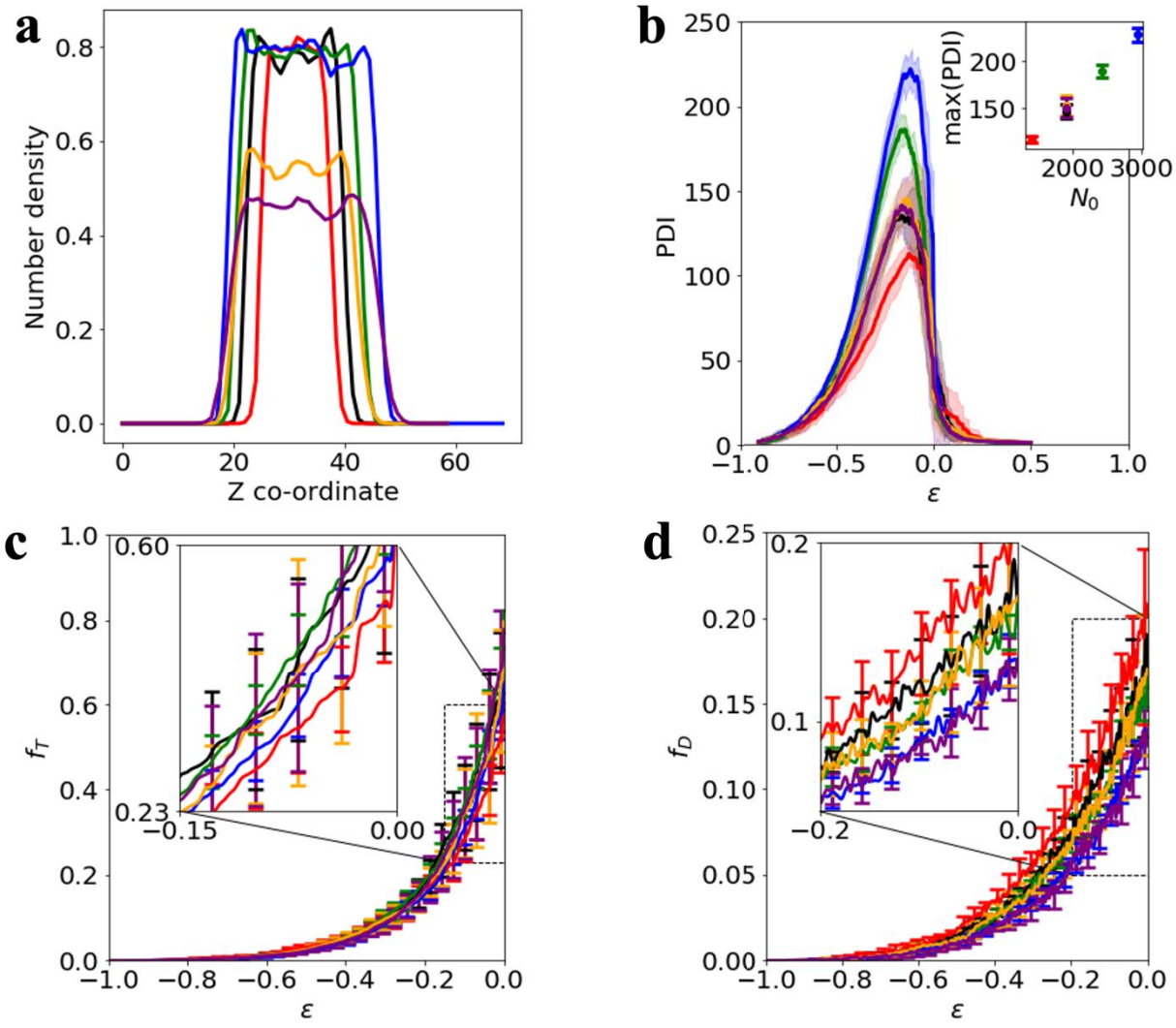


**Figure 4.8. (a)** Number density distribution of all polymer beads in vertical direction averaged over x and y coordinates prior to degradation. **(b)** Polydispersity Index, $PDI$, as a function of the relative extent of reaction, $\epsilon$ . The inset shows maximum value of PDI as a function of a number of precursors in the film, $N_0$. **(c-d)** Fractional mass loss from the largest topological

cluster, $f_T$ in (c) , and from the largest agglomerate, $f_D$, in (d) as functions of the relative extent of reaction, $\epsilon$ . The colors in (a-d) represent simulations with the parameter sets provided in Table 4.1 as following: A(black), B(red), C(green), D(blue), E(orange), and F (purple).

We now define the relative extent of degradation reaction in analogy with the definition used to characterize the gelation process[87]. Recall that the extent of degradation reaction is $1 - p$, hence the relative extent of reaction, $\epsilon$, defining a proximity to the reverse gel point, can be expressed as

$$\epsilon = \frac{p_c - p}{1 - p_c} \quad . \tag{8}$$

The value of $\epsilon$ is calculated for each simulation using the corresponding calculated reverse gel point $p_c (= p_c^w)$ for that simulation. $\epsilon$ increases from -1 at the onset of degradation to zero at the reverse gel point with positive values following the reverse gel point. The quantities in Fig. 6b-d are plotted as a function of the proximity to the reverse gel point.

The trends in PDI discussed above (Fig. 4.4b) hold for all cases considered. Films with the larger number of precursors show a higher peak in PDI while an increase in $N_x$ (an increase in the size of the precursors) has no impact on the PDI. This is anticipated since the PDI is normalized by the size of individual precursors. The maximum value of PDI is plotted as a function of the number of precursors in the inset of Fig. 4.7b and increases approximately linearly with an increase in the number of precursors, $N_0$. When each PDI($\epsilon$) curve is normalized on $N_0$ , all curves approximately collapse into a single master curve (Fig. 4.9), indicating that the polydispersity index normalized on the number of precursors depends only on the proximity to the reverse gel point.

Mass loss from the largest topological cluster, $f_T(\epsilon)$, shows the same trend for all the cases considered (Fig. 4.7d). Large error bars in Fig. 4.7d indicate high variability between the individual independent simulations for the same parameters, however average trends overlap for all the parameter sets (various number and sizes of precursors).

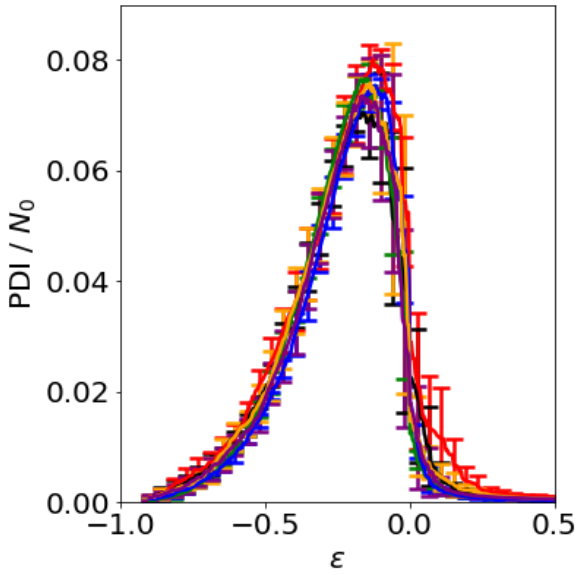


**Figure 4.9.** Comparison of PDI normalized by the number of precursors $N_0$ for the films described in Table 4.1. Colors correspond to the same parameters sets as in Fig. 4.7.

Hence these results show that the fraction of broken-off segments, or the mass loss from the largest topological cluster, depends solely on the proximity to the reverse gel point and does not depend on the total number and size of the precursors for all the cases considered herein. For all the cases considered, the average values of $f_T$ remain close to the apparent mass loss from the largest agglomerate, $f_D$, for $\epsilon \lesssim -0.65$ (Figs. 4.7d and 4.7e).

With an increase in $\epsilon$ until the reverse gel point is reached, $f_D$ increases significantly slower than $f_T$ . In the proximity of the reverse gel point $\epsilon \approx 0$ the fractional mass of the broken-off fragments is more than three fold of the apparent mass loss, $f_D$. Furthermore, erosion from the largest agglomerate distinctly varies for some of the cases considered, despite of the high variability of data from individual runs (Fig. 4.7e). The mass loss closer to the reverse gel point is lower for the films with larger number of precursors (green and blue curves) or lower crosslink density (orange and purple curves) compared to the reference case (black). This distinction is clear in the representative snapshots in Fig. 4.7 and in Fig. 4.5b,c. For the film with the reference parameter set and the film with the smaller number of precursors (Fig. 4.5b,c and Fig. 4.7a,d respectively), a significantly smaller fraction of precursors interact with the film after detachment compared to the film with more precursors (Fig. 4.7b,e) and the film with lower crosslink density (Fig. 4.7c,f).

To compare the effect of varying crosslink density at the same initial film thickness we compared the pairs of simulations C, E and D, F. Both of these pairs have matching thicknesses as seen in Fig. 4.8a, but different $N_x$ ( $N_x = 6$ in sets C, D, $N_x = 10$ in set E, and $N_x = 14$ in set F). The mass loss from the largest agglomerate shows similar trends for the two simulations within each pair. This indicates that in the considered cases the crosslink density does not significantly affect the erosion trend while the actual film thickness has more pronounced effect. The degradation rate constant and the chosen box size did not have an impact on the mass loss from the largest agglomerate, indicating that the detached fragments have sufficient space and time to diffuse away from the largest agglomerate. However, a significant fraction of these fragments remains within or in the close proximity of the largest cluster representing a degrading film near the reverse gel point.

## 4.4 Conclusions

Herein, we utilized DPD simulations to capture degradation and erosion of polymer networks on the mesoscale. We characterized the degradation process via tracking the time evolution of distribution of broken-off fragments. The reverse gel point corresponding to the disappearance of the percolated network was calculated using the reduced weight-average and z-average degrees of polymerization. We then used this calculated reverse gel point to define the relative extent of reaction which identifies the proximity to the reverse gel point. We demonstrated that the fraction of broken-off fragments depends solely on the relative extent of reaction for the samples with various number of precursors, different film thicknesses and different crosslink densities prior to the degradation. We showed that the polydispersity index exhibits a distinct peak prior to the disappearance of the percolating network and strongly decreases at the reverse gel point. The observed peak in PDI scales approximately linearly with the number of precursors; further, the PDI normalized on the total number of precursors depends primarily on the proximity to the reverse gel point.

The reverse gel point measured in our simulations is comparable to predictions of bond percolation theory on a diamond lattice[110]. Small positive deviations from the analytical value seen in our measurements are likely due to the relatively small number of precursors[106]. The dependence of the reverse gel point on number of precursors is analyzed in the next chapter. This analytical value also describes the experimentally measured values of both the gel point[111, 112] and reverse gel point[26] of networks formed with tetra-arm precursors. Notably, the measured value of the reverse gel point is significantly higher than the value predicted by the mean-field theories for the gel point of tetra-functional networks[104, 105]. This is attributed to the fact that the assumption of absence of any intramolecular connections used in these mean-field theories is

not expected to hold for a network[109] prior to degradation. Relatively high reverse gel point observed herein is consistent with the delay of the gel point during the gelation process in the presence of the finite-size loops [106].

Further, we characterized the erosion from the swollen polymer network via tracking the apparent mass loss that accounts for the fragments remaining stuck within or in contact with the percolated network ($f_D$). We showed that while this apparent mass loss remains approximately the same as mass loss from the largest topological cluster for low relative extent of reaction ($\epsilon \lesssim -0.65$), an increase in $\epsilon$ until the reverse gel point is reached results in significantly slower increase in $f_D$ than $f_T$ . In the proximity of the reverse gel point the fractional mass of the broken-off fragments is more than three fold of the apparent mass loss, $f_D$. Furthermore, we quantified that the erosion process from the largest agglomerate does not solely depend on the relative extent of reaction but also distinctly varies with the physical properties of the gel such as sample thickness. Hence both characteristics, $f_D$ and $f_T$, are necessary to quantify and predict the outcome of the erosion process. These results elucidate the main features of degradation and erosion on the mesoscale and could provide guidelines for designing degrading materials with controlled properties. The work described in this chapter is published in the Journal of Physical Chemistry. The corresponding journal article is ref. [70] of the dissertation and the permission to reproduce this work in this chapter is included in Appendix B of this dissertation.

# CHAPTER FIVE

# Mesoscale modeling of nanogel degradation at interfaces and in bulk

## 5.1 Introduction

Nanogels and microgels find their uses in a broad range of applications including drugs and biomolecules delivery and controlled release[5, 120], catalyst carriers[121], interfacial catalysis[122], stimuli responsive emulsion stabilizers[123], and fabrication of scaffolds for cells and tissue culture[124]. These polymeric particles can be fabricated of various shapes, sizes, softness[123, 125], and with tailored stimuli-responsive functionalities. Recent advances in synthesis of functional nanogels and microgels and their applications are surveyed in a number of recent reviews[125-127]. The equilibrium size of a microgel swollen in a solvent depends on solvent quality and is defined by the balance between the osmotic and elastic contributions to the stress tensor. This balance can be externally controlled for a broad range of stimuli-responsive hydrogel networks that can respond to environmental changes such as changes in pH[128], temperature[128, 129], and external light[130]. As an example, thermoresponsive poly(N-isopropylacrylamide)-based gels undergo a temperature induced volume phase transition resulting in a fraction of water being expelled from the network, ultimately causing a particle collapse and respective reduction in microgel size[128, 129, 131]. Photodegradation of nanogels and microgels can be used to remotely control drug delivery[132] or to control properties of scaffolds for multidimensional cell culture[124].

Nanogels and microgels are also extensively used in multi-component systems with two incompatible liquids, where the particles adsorb onto and spread over the liquid-liquid interface effectively decreasing the interfacial tension. In this case, the equilibrium structural characteristics, such as shape and size, of nanogel particles are determined by a range of factors including

interfacial tension between the two liquids, particle elasticity, and affinity of the nanogel polymer to either liquid phase. An extent of deformation and an effective depth of protrusion of microgels into each of the two liquid phases depends on the affinity between the polymer strands and each of these phases[122, 133, 134]. The interfacial tension between the two liquid phases also significantly affects the microgels spreading, with higher extent of spreading observed for higher interfacial tension[135]. Softer nanogels spread to a greater extent over a liquid-liquid interface compared to more densely crosslinked nanogels and hence provide better emulsion stability[123]. Further, the spreading of the microgels and nanogels can be controlled dynamically via a range of external stimuli[128], making these particles excellent candidates for emulsion stabilizers to form Pickering emulsions[123, 136]. Similar to the microgels in a single solvent, a volume phase transition can be triggered in thermoresponsive or pH-responsive gel particles adsorbed at the interfaces resulting in a reduced interfacial coverage due to particle collapse and a subsequent loss of emulsion stability[68, 128].

Herein, we characterize controlled degradation of a nanogel particle in a single solvent and at the liquid-liquid interface. Controlled degradation is of interest since it can be used to dynamically tailor size, shape and thereby transport properties of nanogels and microgels in various environments. In particular, photo-triggered degradation can be turned on and off remotely, which could bring further advantages to regulate properties of these soft particles and rates of cargo release from these nano- and microcarriers. For the nanogels adsorbed at the liquid-liquid interfaces, controlled degradation could provide means to dynamically tune properties of these interfaces, such as interfacial tension and topography of a liquid-liquid interface. Unlike rather comprehensive understanding of gelation processes for various

polymer systems, understanding of the process of network degradation to date remains limited. Controlled degradation can be introduced in micro and nanogels via several pathways[137]. Previous experimental studies provide insights into the erosion of the microgels with chemically labile crosslinkers[138, 139] and microgels with blocks degradable via hydrolysis of ester bonds[140]. Progress of microgel degradation in experiments has been tracked via measurement of the size of microgel particles either in suspensions[120, 140, 141] or adsorbed on a solid substrate[138, 139]. Measurements in suspension show distinctly different profiles for microgels with homogenous network architecture compared to microgels with an initial core-shell structure[141]. The measurements at the surface are either performed by direct observation of degradation of microgel particles adsorbed on a solid substrate[138] or by extracting the nanogel particles from the degrading medium and then depositing them on a solid substrate for measurements and characterization[139].

Since nanogels and microgels are soft polymer networks with characteristic linear sizes on the order of tens to hundreds nanometers to tens of microns, respectively, mesoscale modeling approaches are commonly used to capture their behavior in solvents and at the interfaces. The DPD approach[58, 66, 142] has also been used to model a broad range of multi-component systems[37-39, 41, 43, 44, 90, 142-150] and is often chosen to model behavior of microgels at liquid-liquid interfaces[68, 122, 133, 151-155]. To model controlled degradation and erosion of these microgels, we use the framework described in chapter three which uses the modified segmental repulsive potential (mSRP)[62] to overcome unphysical crossing of polymer chains along with modeling degradable bonds[70, 84]. Similar to chapter four, as a

model polymer network, we focused on gels synthesized by the end-linking of four-arm polyethylene glycol (PEG) precursors[23, 24, 94] originally fabricated by Sakai et al[23]. As noted also in chapter four, these precursors can be modified during their synthesis by including photodegradable functional groups, for example nitrobenzyl[14, 27, 28] or coumarin[24, 27] groups. We showed[70] that the reverse gel point characterizing disappearance of the percolated network is close to but somewhat higher than the value predicted by the bond percolation theory on a diamond lattice[26, 110]. In what follows, we use the same model polymer network with controllably degradable crosslinks between four-arm polymer precursors[70] and focus on characterization of structural characteristics of the remnant nanogel and distribution of broken-off fragments during the degradation process. We consider degradation of nanogels in a single solvent and at the liquid-liquid interface. We show that the affinity between the polymer and solvent strongly affects the evolution of shape and size of the remnant nanogel during the degradation process. The work described in this chapter is published in the Macromolecules. The corresponding journal article is ref. [156] of the dissertation and the permission to reproduce this work in this chapter is included in Appendix B of this dissertation.

**5.2 Specific details of the simulation protocol**

The overall general simulation approach used in this work is the same as that used in chapter four. One specific aspect relevant to this chapter is that in addition to the water and PEG beads, a third kind of beads need to be introduced for the hydrophobic oil phase in the system. For this purpose, we use the same mapping that was originally derived by Groot and Rabone[36] and

which we have used in the previous chapters. Within this coarse-graining scheme, one oil bead represents three $CH_2$ groups[36]. To summarize the coarse-graining choice for this chapter, three water molecules are coarse-grained into a single DPD bead, one hydrophilic PEG bead is taken to represent[157] 1.5 $CH_2OCH_2$ groups and one hydrophobic bead represented three $CH_2$ groups, same as in ref. [36].

Also as described in chapter two and four previously, the interaction parameter between the beads of different types is chosen based on the affinity between the respective moieties as[58] $a_{ij} = a_{ii} + 3.27\chi_{ij}$, where $\chi_{ij}$ is the Flory–Huggins interaction parameter. The repulsion parameter between the polymer and water beads is chosen based on the PEG–water Flory–Huggins interaction parameter[29], $\chi$ = 0.45, as $a_{pw} = 79.5$, and the repulsion parameter between the polymer and oil beads is chosen as $a_{po} = 85.0$. Both these values are close to the values chosen in Ref. [36] to capture the interactions between polyethyleneoxide and water beads and polyethyleneoxide and oil beads (where one DPD bead represents three $CH_2$ groups), respectively. For simplicity, the degradable end groups are taken to have the same solubility as PEG beads. We vary the repulsion parameter between the water and oil phase in the studies below by setting $a_{ow} = 100, a_{ow} = 120$, and $a_{ow}$ =150 in selected series of simulations; note that an increase in $a_{ow}$ corresponds to an increase in the interfacial tension between the oil and water phases[58]. Within the range of chosen values of $a_{ow}$, the oil phase is immiscible with water; it had been previously shown in DPD simulations by Nair et al [158] that the dependence of a mean square radius of gyration on the degree of polymerization of chains composed of oil beads with $a_{ow} = 100$ follows an anticipated scaling for poor solvent. The specific choice of the repulsion parameters in each simulation series below along with the system sizes is provided in Tables 5.1

and 5.2 below. Also, same as in chapter four, all quantities in this work are provided in reduced DPD units, with $r_c$ as the unit length, τ as the unit time, and $k_BT$ as the unit of energy.

To simulate bond breaking during degradation, we use the framework described in chapter three with a reaction time that is taken ten times larger than the time for each update of positions of the beads[46, 47, 49-51], $\tau_r = 10\Delta t$. Similar stochastic approaches have been used previously for various reactive systems[46, 49, 81, 97]. For various polymer networks undergoing controlled photodegradation, the degradation occurs[46] orders of magnitude slower than the characteristic diffusion times on the relevant length scales[70, 84]. Hence we use relatively low degradation rate set by[70] $P = 9 \cdot 10^{-6}$ (corresponding to degradation rate constant of $k = 4.5 \text{ x } 10^{-5}\tau^{-1}$) to ensure that our system is in a kinetically limited regime[46, 84]. After a bond breaking event occurs, the two beads remain unbonded for the rest of the simulation with no change to the interaction parameters of these beads.It should also be noted that although bond breaking can take place every ten timesteps, we only store the bead trajectories every $t_M = 1000\Delta t$ to decrease file sizes with minimal loss of information.

The same diamond-like lattice[46, 98] as described in chapter four is used as an initial configuration of the nanogel's polymer network. Same as in the case of hydrogel films, the effective "unit cell" is created by first placing tetra-functional beads at lattice sites and then placing $N_x/2$ beads for each of the four polymer arms[70], so that there are $N_x$ beads between the centers of two bonded precursors. To create nanogel particles, we first replicate this unit cell $N_{rep}$ times in each of the x, y, and z directions. The fractional precursors with a functionality less than four at the faces of the initially cubic network are deleted and a sphere is drawn inside the cubic network with its center as the center of the cube and a diameter ($D_{cut}$) smaller than the side length of the cube. All precursors with any bead outside of the sphere are deleted to generate approximately

spherical nanogel particle with an integer number of total precursors $N_p$ and with dangling chains at the surface of the network[84]. All the parameters used for constructing the initial network are provided in Table 5.1. Prior to the production runs, all the nanogels are equilibrated in the water phase for $12x10^5$ time steps without allowing for degradation.

**Table 5.1**: Parameter sets corresponding to the degradation simulations in single solvent

| Set | $N_x$ | Unit cell repeats | Radius factor | Total polymer beads | $N_p$ | Total degradable bonds | $a_{pw}$ | Simulation box size | Beads in one precursor |
|---|---|---|---|---|---|---|---|---|---|
| A | 10 | 5x5x5 | 0.97 | 9996 | 476 | 836 | 79.5 | 60x60x60 | 21 |
| B | 10 | 6x6x6 | 0.85 | 12537 | 597 | 1032 | 79.5 | 60x60x60 | 21 |
| C | 10 | 6x6x6 | 0.97 | 16821 | 801 | 1416 | 79.5 | 60x60x60 | 21 |
| D | 6 | 6x6x6 | 0.96 | 10413 | 801 | 1416 | 79.5 | 50x50x50 | 13 |
| E | 20 | 6x6x6 | 0.64 | 9799 | 239 | 380 | 79.5 | 60x60x60 | 41 |
| F* | 6 | 6x6x6 | 0.77 | 5421 | 417 | 708 | 79.5 | 60x60x60 | 13 |
| G | 10 | 5x5x5 | 0.67 | 3612 | 172 | 284 | 79.5 | 60x60x60 | 21 |
| H | 10 | 6x6x6 | 0.72 | 6909 | 329 | 560 | 79.5 | 60x60x60 | 21 |
| I | 10 | 6x6x6 | 0.77 | 8757 | 417 | 708 | 79.5 | 60x60x60 | 21 |
| J | 16 | 6x6x6 | 0.77 | 13761 | 417 | 708 | 79.5 | 60x60x60 | 33 |
| K | 10 | 6x6x6 | 0.94 | 15309 | 729 | 1296 | 79.5 | 60x60x60 | 21 |
| L | 10 | 6x6x6 | 0.77 | 8757 | 417 | 708 | 82.0 | 60x60x60 | 21 |

| | | | | | | | | | |
|---|---|---|---|---|---|---|---|---|---|
| M | 10 | 6x6x6 | 0.77 | 8757 | 417 | 708 | 85.0 | 60x60x60 | 21 |
| N | 6 | 6x6x6 | 0.77 | 5421 | 417 | 708 | 82.0 | 60x60x60 | 13 |
| O | 6 | 6x6x6 | 0.77 | 5421 | 417 | 708 | 85.0 | 60x60x60 | 13 |

* reference parameter set

F*, N and O parameter sets are used to analyze impact of solvent quality in main text.

**Table 5.2**: Parameter sets used in simulations of degradation at interface

| **Set** | $a_{ow}$ | **Simulation box size** | **# water beads** | **# oil beads** | **# polymer beads** | **Total beads** |
|---|---|---|---|---|---|---|
| A | 100 | 60x60x70 | 372579 | 378000 | 5421 | 756000 |
| B | 120 | 60x60x70 | 372579 | 378000 | 5421 | 756000 |
| C | 150 | 60x60x70 | 372579 | 378000 | 5421 | 756000 |

Properties of the nanogel polymer networks in sets A-C are same as in set F in Table 5.1

An equilibrated nanogel particle swollen in water is shown in Fig. 5.1b. PEG beads are shown in cyan, and the end groups of both precursors are shown in red and blue, respectively. For clarity of representation, the water beads are hidden. The degradable bonds in the system are chosen to be the bonds between the end functionalities (Fig. 5.1a) since the cleavable sites are typically chosen to be in the proximity of the end functionality[24, 26]. Three water molecules are represented by a single DPD bead, the oil phase is modeled using short chains with four beads each[158], and the number of beads between the centers of two bonded precursors, $N_x$, is varied as detailed in Table 5.1.

The processes of degradation of nanogels in a single solvent and degradation of nanogels adsorbed at the liquid-liquid interface are characterized and compared in this study. In all the simulations of the gel particles degrading in a single solvent, bond breaking is switched on immediately after the equilibration step and the degradation is carried on for $3x10^6$ time steps. In all the simulations involving degradation of the nanogels at the liquid-liquid interface, the nanogels equilibrated in water are first placed into the water phase in the binary oil-water system and are allowed to adsorb onto the interface and attain a new equilibrium shape. The degradation is turned on only after the gels are equilibrated at the liquid-liquid interface; then the degradation study is carried out for $3x10^6$ time steps.

## 5.3 Results and Discussion

### *5.3.1 Characterizing nanogel degradation in bulk and at the liquid-liquid interface*

We first characterize degradation of a nanogel depending on its environment via tracking and comparing the main characteristics of the degradation process for the same nanogel particle swollen in a good solvent and adsorbed at the liquid-liquid interface. The snapshots during degradation are shown in Fig. 5.1 with panels b-d corresponding to degradation in water and panels e-j corresponding to degradation at the oil-water interface. The parameters are chosen corresponding to the reference parameter sets (Tables 5.1 and 5.2 above). Prior to the onset of degradation, the nanogel swollen in water attained approximately spherical shape upon equilibration (Fig. 5.1b). During degradation, the breaking of bonds results in an effective decrease in crosslink density accompanied by detachment of fragments from the nanogel particle. To characterize the degradation process, we first define a cluster as a set of bonded precursors at any stage during the degradation[70]. In a similar manner, we define the nanogel as the largest cluster of bonded precursors at a given time instant. This definition is relevant until the reverse gel point,

since only until this point the largest cluster represents the remnant part of the original nanogel, as can be seen in Fig. 5.2. The largest cluster of chemically bonded precursors is highlighted in all images in Fig. 5.1, while the detached fragments are shown as translucent. The decrease in the effective crosslink density is pronounced at relatively early times, during which approximately homogenous swelling of the remnant nanogel in water is observed (Fig. 5.1c, also see quantitative characterization below). At this stage, a fraction of the fragments that are detached from the nanogel diffuses away from the network while some fragments remain stuck inside the particle.

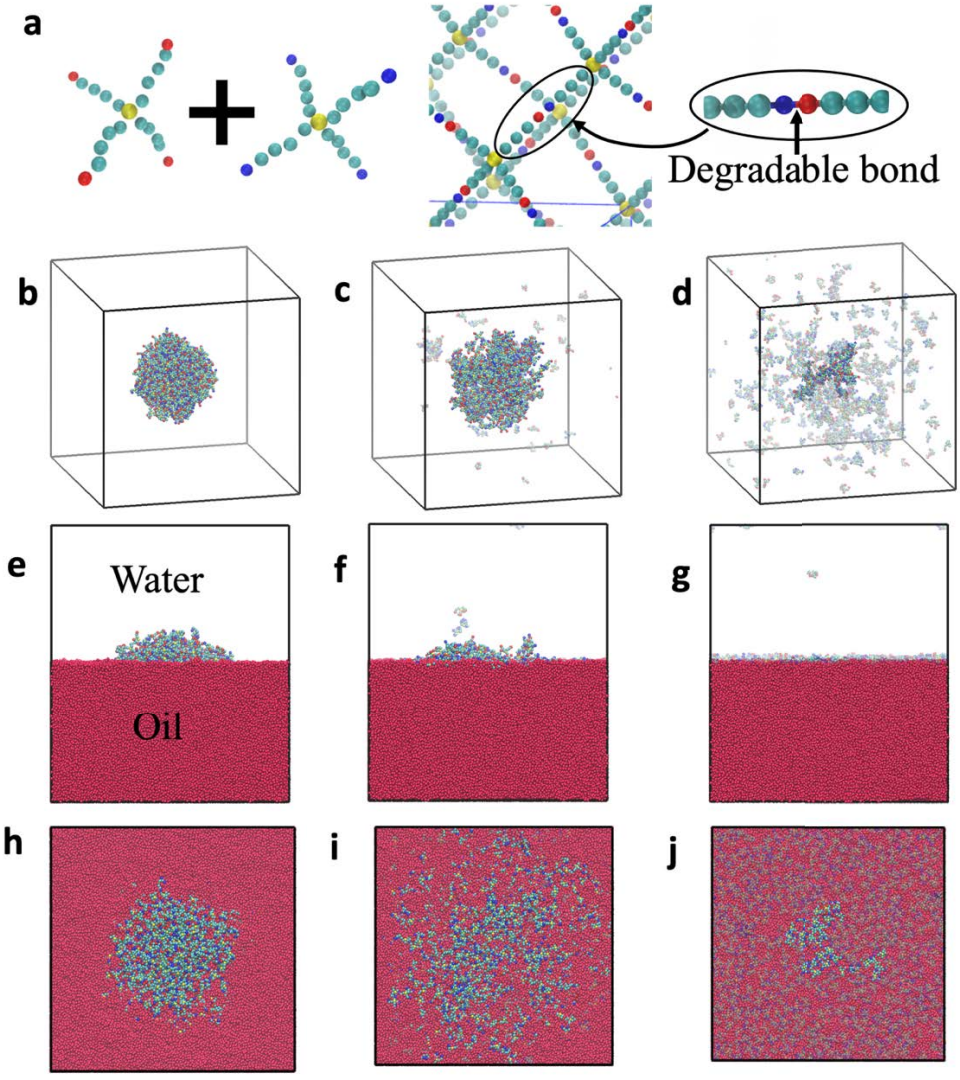

**Figure 5.1. Nanogel degradation in water and at the oil-water interface.** (**a**) Schematic of the fragment of nanogel network with degradable bonds. Snapshots of a single nanogel corresponding to the reference parameter set (set F in Table 5.1), **(b-d)** nanogel degradation in good solvent and **(e-j)** degradation of a nanogel initially adsorbed at the oil-water interface. Dimensionless time, in units of $\tau$, is t=0 in (b, e, h), t=10,000 in (c, f, i), and t=22,000 in (d, g, j). Polymer beads are colored as described in the text, oil beads are shown in red and water beads are hidden for visual clarity. **(e-g)** Side view and **(h-j)** top view of the nanogel at the interface. In the above snapshots, the largest cluster is highlighted while all other polymer beads shown as translucent.

At late times, due to detachment of sufficiently large fraction of fragments, the nanogel loses its spherical shape.

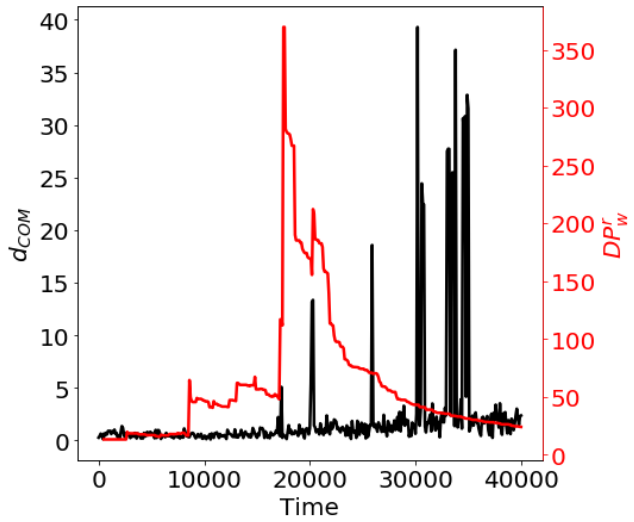


**Figure 5.2: Tracking nanogel as the largest connected cluster in the system.** Displacement of the center of mass of the largest cluster every 5000 simulation steps ($d_{COM}$, black curve, left axis)

and reduced weight average degree of polymerization, ($DP_w^r$, red curve, right axis) during degradation of the nanogel with reference parameters set F (Table 5.1). Large "jumps" in $d_{COM}$ only occur at or after the reverse gel point (global peak in $DP_w^r$) indicating that up to the reverse gel point the largest cluster corresponds to the remaining portion of the original nanogel, hence only smooth changes in $d_{COM}$ are observed until the reverse gel point. As degradation continues, either the fragment corresponding to the original nanogel or one of the larger fragments that broke-off can become the largest clusters in the system; large "jumps" in $d_{COM}$ indicate that different fragments separated by a notable distance are identified as largest clusters at various time instants.

In comparison to the nanogel in the water (Fig. 5.1b-d), the nanogel at the liquid-liquid interface has an initial asymmetric shape prior to the degradation (Fig. 5.1e,h). This shape is defined by the interplay between the energetically favorable shielding of oil-water contacts and an energy penalty due to the increase in elastic energy contribution upon nanogel deformation. Prior studies demonstrated effective flattening of gel particles at the interfaces[123, 129, 133] with more pronounced interfacial spreading of loosely crosslinked gels. The specific deformation and the depth of protrusion into each liquid phase depends on the affinity between the polymer strands and these liquids phases[122, 133, 134]. For the chosen affinity of the polymer network with both liquid phases (see section 5.2), the nanogel adsorbed at the interface largely remains in the water attaining close to hemispherical shape prior to degradation. Similar to the nanogel in water considered above, at the beginning of degradation the decrease in crosslink density is notable and correspondingly leads to the enhanced spreading and interfacial coverage (Fig. 5.1f,i). The remnant nanogel particle along with most of the detached fragments remains adsorbed at the interface with the adsorbed fragments diffusing along the interface to promote shielding of a large

number of unfavorable oil-water contacts. The fragments that detach while in the water phase are also later adsorbed by the interface (one such fragment is highlighted in Fig. 5.1f). Below we characterize the reverse gelation transition for the nanogels at the interface and that in a single solvent.

*5.3.2 Characterizing nanogel size, shape, reverse gel point, and mass loss*

Prior to the degradation the nanogel constitutes the only cluster in the system. During the degradation process, clusters of different sizes (i.e. both different numbers of precursors and different geometric sizes) and shapes are formed in the system. The nanogel particle, defined above as the largest cluster of connected precursors, contains $N(t)$ precursors at any time, out of the initial $N_p$ precursors in the original nanogel. We measure the size and shape of the degrading remnant nanogels via the gyration tensor of the largest cluster at any time. The components of the gyration tensor are given as $S_{mn} = \frac{1}{N_b^2}\Sigma_{i=1}^{N_b}\Sigma_{j=i}^{N_b}\left(r_m^i - r_m^j\right)\left(r_n^i - r_n^j\right)$, where $m, n$ indicate cartesian directions, $N_b$ is the total number of beads comprising the nanogel and $r_m^i$ is the $m$-th component of the position vector $\boldsymbol{r}^i$ of the $i^{\text{th}}$ particle. The eigenvalues of the gyration tensor, $\lambda_1, \lambda_2,$ and $\lambda_3,$ provide a measure of characteristic size squared along three principle directions and allow one to calculate the radius of gyration, $R_g,$ and the shape anisotropy, $\kappa^2$, as:

$$R_g^2 = \lambda_1 + \lambda_2 + \lambda_3 \tag{5.1}$$

and

$$\kappa^2 = \frac{3\left(\lambda_1^2+\lambda_2^2+\lambda_3^2\right)}{2(\lambda_1+\lambda_2+\lambda_3)^2} - \frac{1}{2}. \tag{5.2}$$

The $\kappa^2$ is typically used to characterize shapes of various polymeric species[61, 159, 160] and ranges from $\kappa^2 = 0$ for an ideal sphere to $\kappa^2 = 0.25$ for a planar object (with $\lambda_1 = \lambda_2$ and $\lambda_3 =$

0) to $\kappa^2 = 1$ for points on a line[159]. For linear polymer chains, $\kappa^2 \approx 0.43$ and $\approx 0.39$ in good and theta solvents, respectively [161-163].

The time evolution of $R_g$ and $\kappa^2$ for a nanogel particle (reference parameter set F in Table 5.1) degrading in water (black curve) and at the interface (red curve) is provided in Fig. 5.3 a,b. The values at $t = 0$ indicate the equilibrium values prior to degradation. As degradation begins, the $R_g$ of the nanogel in the water increases approximately up to $t \approx 19{,}000$ for the chosen simulation run (Fig. 5.3) and then decreases. During the initial increase in $R_g$, up to $t \approx 10{,}000$, there is no significant change in $\kappa^2$. Close to zero values of $\kappa^2$ correspond to the equilibrium spherical nanogel shape prior to and during initial stages of degradation. Hence, the nanogel size initially increases without any notable increase in shape anisotropy; this indicates that the nanogel undergoes approximately homogenous swelling maintaining the spherical shape during this initial phase of degradation. The second portion of the increase in $R_g$ is somewhat less smooth (at times approximately within the interval $t \in [10^4 : 1.9 \cdot 10^4]$ for the simulation in Fig. 5.3); during this time frame, some increase in $\kappa^2$ is observed, indicating notable deviations from spherical symmetry. The latter sharp decrease in $R_g$ is accompanied by a significant increase in the shape anisotropy. As we show below, this decrease in $R_g$ and increase in $\kappa^2$ correspond to the reverse gelation transition. At late times the measured value of $R_g$ and $\kappa^2$ correspond merely to the largest polymeric cluster in the system and not to the remnant nanogel (as discussed in Fig. 5.2).

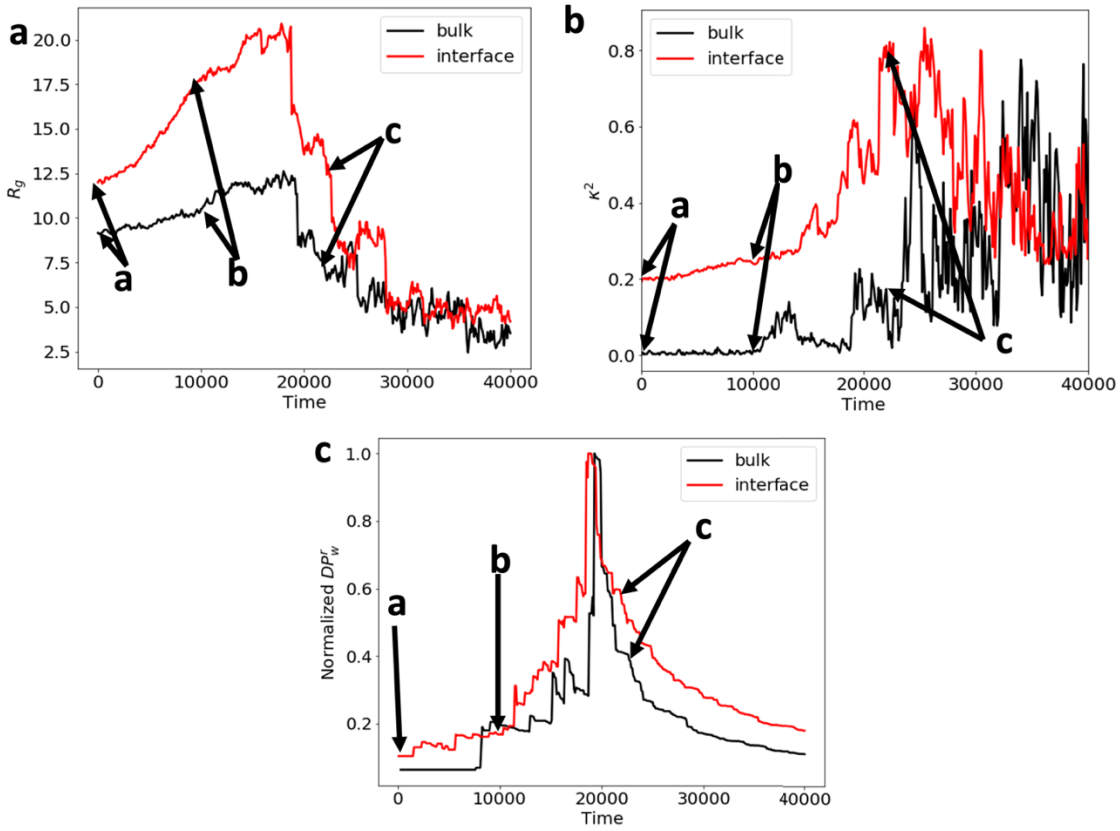


**Figure 5.3.** Time evolution of **(a)** the radius of gyration, $R_g$, (**b**) shape anisotropy, $\kappa^2$, (**c**) reduced weight average degree of polymerization, $DP_w^r$ . The points marked by arrows correspond to the snapshots in Fig. 5.1. The data in **c** are normalized by the corresponding maxima.

Thus at late times the value of $R_g$ decreases significantly while $\kappa^2$ fluctuates around an average value of $\kappa^2 \approx 0.40 \pm 0.19$ (Fig. 5.3b, the average is taken at time interval $t \in [35000: 50000]$ using 150 frames). Large fluctuations of the shape anisotropy were previously reported while characterizing conformations of polymers of various architectures[61, 161-163].

For the nanogel at the interface, the initial values of both $R_g$ and $\kappa^2$ are higher than the values for the nanogel in water due to the initial spreading of the nanogel at the interface prior to degradation as discussed above. As degradation begins, the $R_g$ increases faster compared to the nanogel in water and then decreases sharply at late times ($t > \approx 18{,}000$ for the simulation in Fig. 5.3). In contrast to the degradation in water, $\kappa^2$ for the degradation at interface increases continuously from the beginning of degradation. This indicates that the nanogel loses its initial shape at the interface immediately after the onset of degradation since the degradation promotes the spreading over the interface.

Next we relate the observed trends in $R_g$ and $\kappa^2$ to the reverse gelation transition in both cases of degradation in a single solvent and degradation at an interface. Analogous to the approach used to identify gel point in the simulations of gelation process[101, 102, 106, 107], the location of the reverse gel point can be identified[70], as in the orevious chapter, using the reduced weight average degree of polymerization, $DP_w^r$, defined as

$$DP_w^r(t) = \frac{\Sigma' \, n_i(t) \, i^2}{\Sigma' \, n_i(t) \, i}, \tag{5.3}$$

where $n_i(t)$ is the number of topological clusters with size $i$ at time $t$ and the $'$ indicates summation over all but the largest cluster. The $DP_w^r$ curves for the degradation of a nanogel in water (in black) and at the interface (in red) are shown in Fig. 5.3c. The critical time instant corresponding to the peak value of $DP_w^r$ indicates the reverse gel point[70], which is analogous to the definition of gel point in gelation simulations[101, 102, 106, 107, 113, 115]. The time instant corresponding to peaks in $DP_w^r$ in Fig. 5.3c, $t_c$, allows one to identify a reverse gel point as a critical value of the fraction of degradable bonds intact at this time instant[70], $p_c = \exp(-kt_c)$. The exact location of the reverse gel point somewhat differs for the individual simulations due to the stochastic nature of the degradation process. Indeed, the reverse gel points are approximately within the error bars

for the two scenarios when averaged over five independent simulation runs. Specifically, $p_c = 0.44 \pm 0.01$ for the degradation in water and $p_c = 0.47 \pm 0.05$ for the degradation at interface. This is expected since the current model assumes, for simplicity, no effect of the surrounding moieties on the probability of bond breaking. Once the reverse gel point for a given system is identified, the proximity to this point at a given time instant can be defined via the relative extent of degradation[70], $\epsilon$ , which was defined in the previous chapter and is analogous to the definitions of relative extent of gelation during the gelation process[87]:

$$\epsilon = \frac{p_c - p}{1 - p_c}. \tag{5.4}$$

Note that the fraction of bonds broken, $1 - p$, defines an extent of the degradation reaction and hence the definition of $\epsilon$ above provides a relative measure of proximity to the reverse gel point. With the above definition, $\epsilon = -1$ corresponds to the onset of degradation, $\epsilon = 0$ to the reverse gel point, and positive values of $\epsilon$ correspond to the degradation after the reverse gelation transition. In what follows, we plot all data characterizing degradation processes as a function of $\epsilon$ to identify main trends in evolution with the proximity to the reverse gel point.

The dependence of shape anisotropy $\kappa^2$, the ratio of the largest to smallest eigenvalues $\lambda_1/\lambda_3$, and $R_g$ for nanogels degrading in water (black curves) and for nanogels degrading at the interface (red curves) with an increase in the extent of degradation up to the reverse gel point is provided in Fig. 5.4. The values in this and following plots are averaged over five independent simulations with error bars denoting standard deviation.

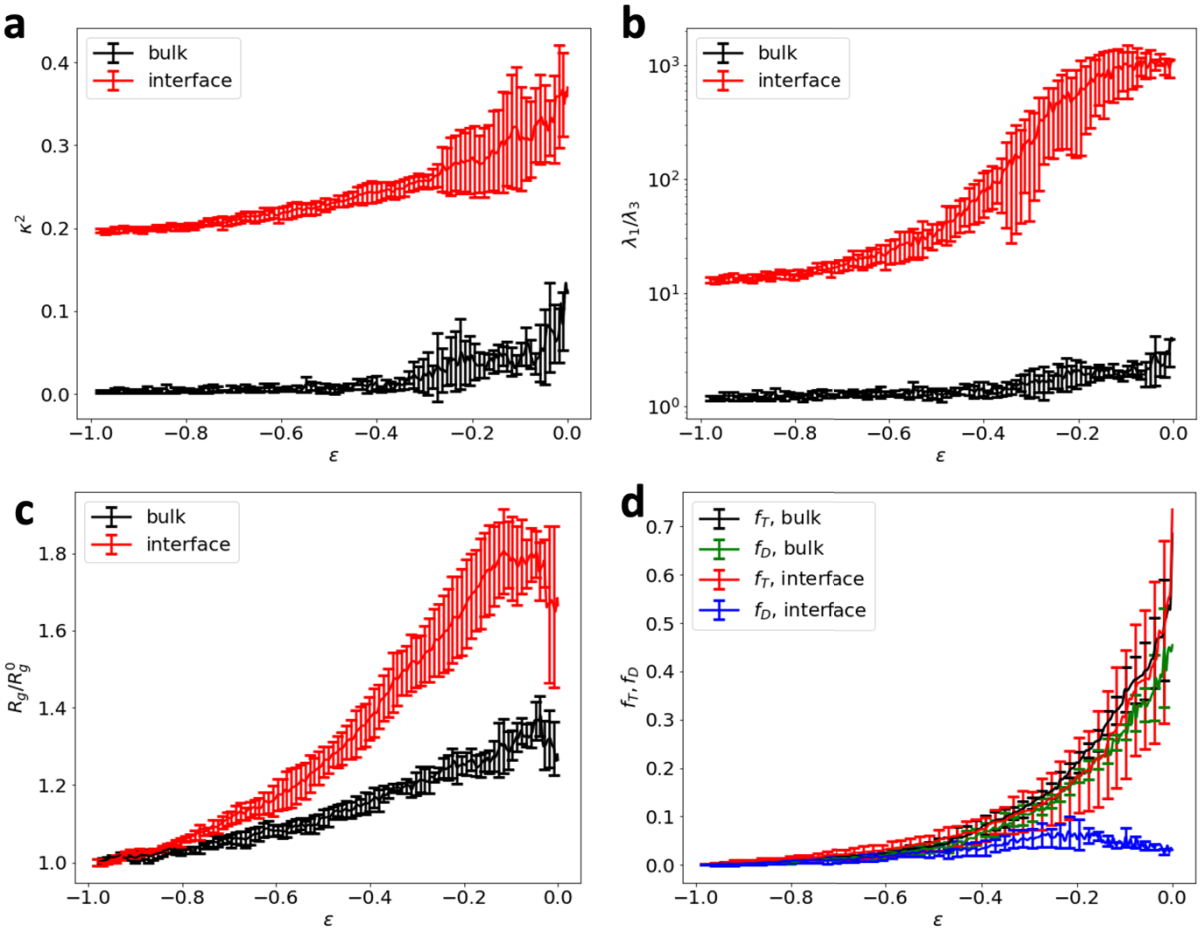


**Figure 5.4.** Evolution of (**a**) shape anisotropy, (**b**) ratio of largest to smallest eigenvalues, (**c**) radius of gyration normalized by the value prior to degradation, and (**d**) topological and distance-based mass loss for degradation in water and at the interface. The distance-based mass loss is represented by green (in water) and blue (at interface) curves, and $f_T$ is shown in black (in water) and in blue (at interface). All data represent an average over five independent simulations with error bars denoting standard deviation.

Relatively far from the reverse gel point ($\epsilon \approx [-1:-0.38]$), $\kappa^2 \approx 0$ and $\lambda_1/\lambda_3 \approx 1$ for the degradation in water with relatively small error bars (Fig. 5.4a,b), confirming that the broken bonds

at this extent of degradation result in an effective decrease of the crosslink density and nearly isotropic swelling of the nanogel particle. Correspondingly, $R_g$ increases monotonically with relatively small error bars at these low $\epsilon$ (Fig. 5.4c). With further increase in the extent of degradation of nanogel in water ($\epsilon \gtrsim -0.38$), both $\kappa^2$ and $\lambda_1/\lambda_3$ somewhat increase with notably larger error bars indicating that nanogel is no longer isotropic. However, the average value of $\kappa^2$ and the standard deviation around mean remain low with respect to that expected for example for a random coil configuration.

On the contrary, both $\kappa^2$ and $\lambda_1/\lambda_3$ increase nearly monotonically from the onset of degradation with the increase in $\epsilon$ for the gels degrading at the interface (red curves in Fig. 5.4 a,b). Note that the initial values of $\kappa^2$ and $\lambda_1/\lambda_3$ on these plots are defined by the equilibrium shape of the gel particle adsorbed at the interface. As discussed above, this shape is anisotropic and depends on the affinities between all the moieties in the system and on the crosslink density of the nanoparticle prior to degradation. A distinct (over two orders of magnitude) increase in the ratio $\lambda_1/\lambda_3$ with an increase in $\epsilon$ indicates that the nanogel essentially spreads over the interface during the degradation. Correspondingly, more distinct increase in the radius of gyration normalized by that prior to degradation is observed with an increase in $\epsilon$ for the nanogels in water (Fig. 5.4c).

The characterization of topological clusters described above provides information about the remnant nanogel particle and allows one to identify the reverse gel point. In addition, it is also instructive to analyze the spatial distribution of fragments detaching from the degrading nanogels. Hence, in addition to the characterization of topological clusters discussed above, we also define a distance-based cluster or an agglomerate as the set of polymer precursors each having at least one contact with another precursor[70] (two beads belonging to these precursors are within the

interaction distance $r_c$). Correspondingly, during the degradation process we calculate the number of precursors in the largest agglomerate in the system, $N_D(\epsilon)$, along with the size of the largest topological cluster as defined above, $N(\epsilon)$. At the onset of degradation, $N_D(-1) \equiv N(-1) \equiv N_p$ . During the degradation, $N_D(\epsilon)$ can significantly exceed $N(\epsilon)$ since it accounts for the fragments stuck within or remaining in the close proximity to the surface of the largest topological cluster. The fraction of precursors broken-off from the nanogel can be characterized via the topological mass loss, $f_T(\epsilon) = 1 - N(\epsilon)/N_p$, while the fraction of precursors that not only broke-off but also diffused away (to distance exceeding $r_c$) from the largest agglomerate (which encompasses the remnant nanogel) can be characterized via distance-based mass loss as $f_D(\epsilon) = 1 - N_D(\epsilon)/N_p$.

The fraction of broken-off fragments represented by $f_T(\epsilon)$ is indistinguishable for degradation in water and at an interface (black and red curves in Fig. 5.4d). This is anticipated, since topological mass loss is defined by the rate constant of bonds breaking and does not depend on diffusion of broken-off fragments. For degradation in water, $f_D$ in this reference scenario (green curve) is indistinguishable from $f_T$, clearly indicating that no fragments are stuck within the largest agglomerate or in close proximity to it. On the contrary, $f_D$ at the interface remains close to zero (blue curve in Fig. 3d) as the fragments that detach from the nanogel remain adsorbed at the interface. $f_D$ somewhat increases around $\epsilon \approx -0.2$ as some fragments diffuse away from the nanogel particle, however at later times these fragments are adsorbed onto the interface. In the proximity of the reverse gel point, the degraded fragments cover the interface having contacts with largest agglomerate thereby reducing $f_D$ to values close to zero.

*5.3.3 Scaling of reverse gel point*

Next we identify the reverse gel point as a function of the number of precursors in the nanogel, $N_p$. The specific nanogel parameters used in multiple series of simulations in water and

at the interface are provided in Tables 5.1 and 5.2. For each parameter set the critical value of $p_c$ is found from the maximum of the reduced weight-average degree of polymerization using the procedure described above. The values of $\overline{p_c}$ provided in Fig. 5.5 are averaged over five independent simulation runs with the error bars representing the standard deviation, $\Delta\overline{p_c}$. The data from nanogels in water and at the interface are shown in Fig. 5.5 by the black and red symbols, respectively. The data points shown by the green symbols are reproduced from chapter four on hydrogel films[70]. The $\overline{p_c}$ is lower for the simulations with higher total number of precursors and this value of reverse gel point is also close to the analytical estimate from the bond percolation theory on a diamond lattice[87, 110] marked by the dashed line in Fig. 5.5. There is an evident increase in both $\overline{p_c}$ and $\Delta\overline{p_c}$ with the decrease in $N_p$. The increase in $\Delta\overline{p_c}$ is attributed to the stochastic nature of the process since higher number of precursors provide better statistics. The increase in $\overline{p_c}$ upon decrease of the number of precursors is anticipated from analytical theories of gelation reflecting the finiteness of any "simulated" system (finite number of precursors) compared to the infinite system sizes assumed in classical percolation theories[87, 110, 164].

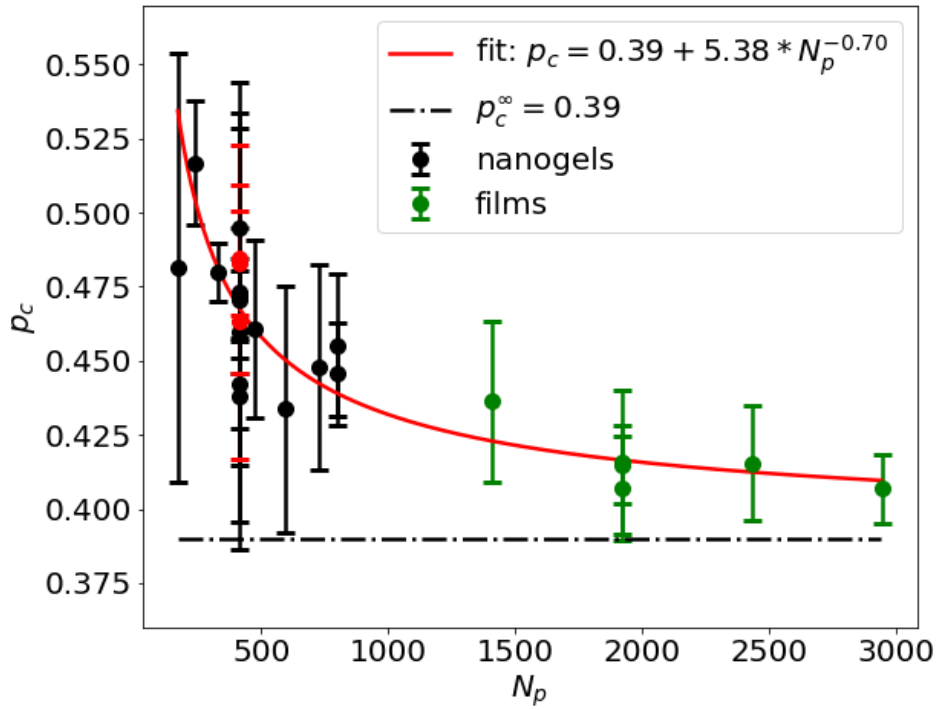


**Figure 5.5. Scaling of the reverse gel point with the number of precursors, $N_p$.** The dependence of reverse gel point $p_c$ on the total number of precursors in the system. Symbols correspond to the measured $p_c$ for nanogels degrading in water (black symbols), nanogels degrading at the interface (red symbols) and hydrogel films from Ref. [70] (green symbols). The dashed line corresponds to $p_c^{\infty} = 0.39$. The error bars represent standard deviation taken over five independent simulations in each case. The red line corresponds to a weighted nonlinear least squares fitting of the simulated data.

The following relation is expected to hold for percolation on regular lattices during gelation process[87, 110, 115]:

$$p_c(N_p) = p_c^{\infty} + cN_p^{-\sigma}, \tag{5.5}$$

where $p_c^\infty$ is an analytical estimate for the percolation threshold on an infinite lattice, $\sigma$ is a scaling exponent and $c$ is a proportionality constant. It should be noted here that nanogel particles indeed consist of a finite number of polymeric precursors and hence, as opposed to gelation of macroscopic samples, effects of finiteness should be taken into account. For the gelation process modeled as percolation on Bethe lattice of functionality four, the values $p_c^\infty = 0.33$ and $\sigma = 0.5$ had been derived[87, 110]. However, both these values are not expected to hold for gelation processes that differ significantly from the ideal Bethe lattice percolation model and for the corresponding reverse gelation processes. For example, values of $p_c^\infty$ significantly exceeding the predicted $0.33$ (so-called delay in the gel point) have been reported in a number of studies of gelation processes[107, 109, 113-117]; this delay is typically attributed to intramolecular reactions. The gel point values close to percolation threshold on the diamond lattice $(0.39)$ have been reported for the gelation of tetra-arm PEG precursors near the overlap concentration[111, 112]. Further, the scaling exponent $\sigma = 0.5$ is not expected to necessarily hold for the systems with defects such as loops[106, 115] or for the systems with intramolecular reactions. The scaling relation in equation (5.5) had been used[106, 115] for prediction of true gel points using Kinetic Monte Carlo simulations; it had been shown that the predicted gel point is insensitive to the scaling exponent within the range $\sigma \approx 0.3 - 0.7$.

Unlike fairly comprehensive understanding of gelation processes for various systems, understanding of the kinetics of network degradation remains limited. Reverse gel points ranging between 0.43 and 0.48 for networks formed by the tetra-PEG precursors at various stochiometric ratios were reported by Li et. al. [26]; the authors concluded that the reverse gel points observed in their work are close to the predictions of percolation models on the diamond lattice. In our recent work[70] (see also chapter four) we demonstrated that the reverse gel point calculated during

degradation of hydrogel films formed by the tetra-arm precursors is close to but somewhat higher than predictions of bond percolation theory on a diamond lattice[110].

To estimate the scaling of the reverse gel point with the number of precursors, $N_p$, based on our simulation data, we used a weighted nonlinear least squares regression method*[165]*. Equation (5.5) was used as the prediction model with a weighted loss function taken as $\sum\left(\frac{p_c(N_p)-\overline{p_c}}{\Delta\overline{p_c}}\right)^2$, where $p_c(N_p)$ is the predicted value and the summation is taken over all the available data points. The choice of $1/\Delta\overline{p_c}$ values as weights is made herein to bias the fitting towards data points with lower $\Delta\overline{p_c}$ since these points are measured with higher certainty*[165]*. By setting*[110]* $p_c^{\infty} = 0.39$ and treating $c$ and $\sigma$ as the fitting parameters, we obtained the best fit as $c = 5.38 \pm 2.38$ and $\sigma = 0.7 \pm 0.07$. The best fit to the simulation data points is provided in Fig. 5.5 as $p_c = p_c^{\infty} + 5.38 * N_p^{-0.70}$ (red curve).

*Effects of polymer-solvent interaction*

We now focus on the effect of polymer-solvent interaction on the degradation and erosion kinetics of nanogel particles in a single solvent. We consider three values of the polymer-solvent interaction parameter: $a_{ps} = 79.5, 82.0$ and 85.0 with $a_{ps} = 79.5$ representing a good solvent and $a_{ps} = 82.0, 85.0$ representing decrease in solvent quality. The snapshots for degradation of nanogels for these three cases are shown in Fig. 5.1b-d, Fig. 5.6a-c and Fig. 5.6d-f, respectively.

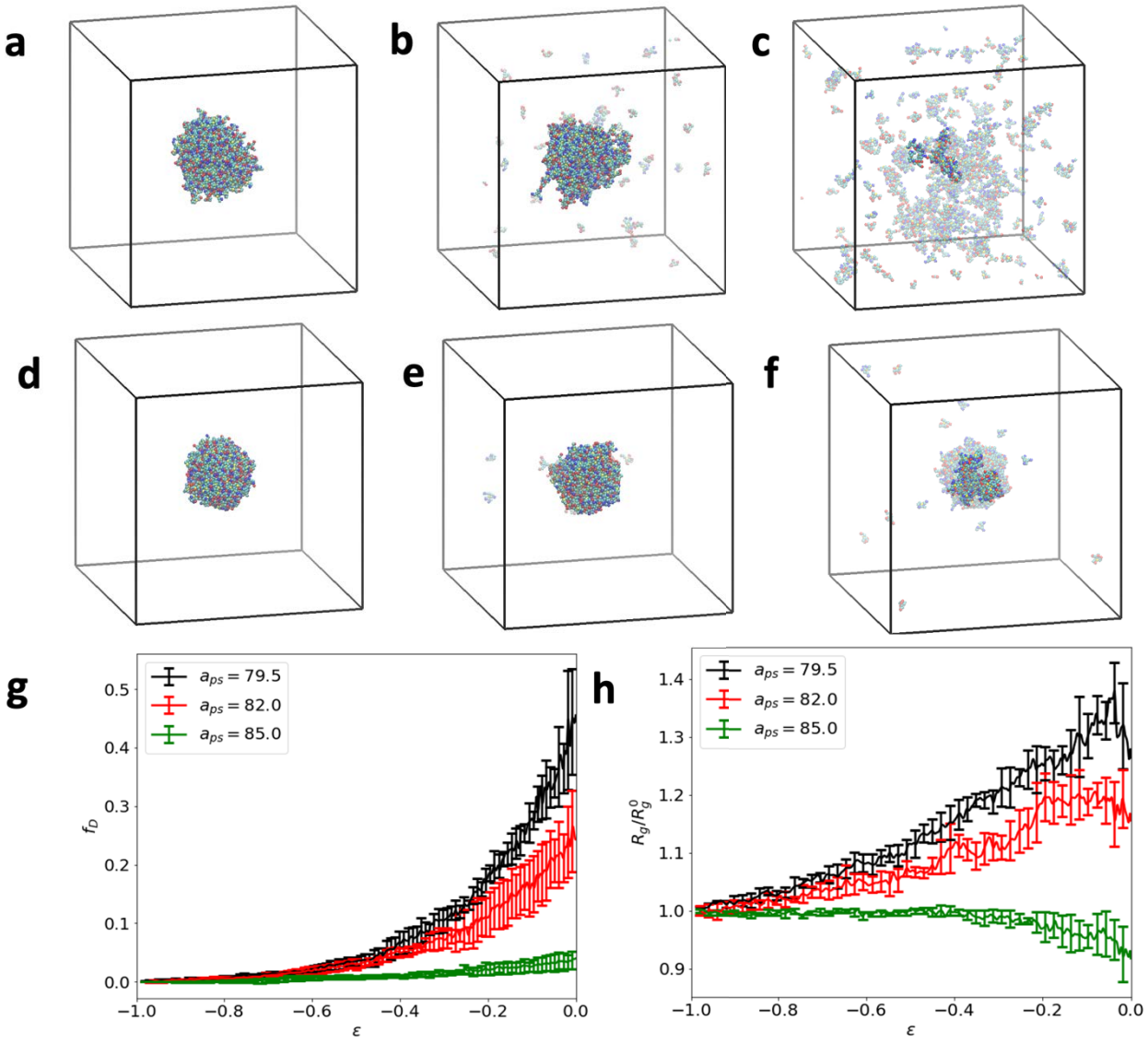


**Figure 5.6. Effects of solvent quality on nanogel degradation in a single solvent.** Snapshots of the nanogel degrading in a solvent with $a_{ps} = 82.0$ **(a-c)** and in a solvent with $a_{ps} = 85.0$ **(d-i)** at t=0 **(a, d)** , t=10,000 **(b, e)** and t=22,000 **(c, f)**. **(g)** Evolution of the distance-based mass loss and (**h**) radius of gyration during degradation in a solvent with $a_{ps} = 79.5$ (black curve), $a_{ps} = 82.0$ (red curve) and $a_{ps} = 85.0$ (green curve).

A decrease in solvent quality results in a lower degree of swelling both prior to and during the degradation of the nanogel. This is evident in the initial and early time snapshots of the degrading nanogel particles. As expected, the topological mass loss, $f_T(\epsilon)$, in all three cases remains the same. The fractional mass loss from the largest agglomerate, however, $f_D(\epsilon)$, follows distinctly different trends depending on solvent quality. Recall that $f_D$ effectively accounts for the fragments that not only break-off but also diffuse away from the nanogel. For the solvent of intermediate quality ($a_{ps} = 82.0$, top row in Fig. 5.6), significantly smaller number of fragments are seen leaving the main agglomerate than that in the reference scenario at the same time instants (Fig. 5.1, top row). These differences are even more pronounced for the relatively poor solvent ($a_{ps} = 85.0$), where only small fraction of fragments is seen leaving the nanoparticle (second row in Fig. 5.6). As discussed above, no notable agglomeration of the broken-off fragments within the nanogel is observed for the good solvent case (black curve in Fig. 5.6g). Clearly some agglomeration of the broken-off segments within the largest agglomerate is observed for the intermediate solvent quality ($a_{ps} = 82.0$), resulting in significantly lower values of $f_D(\epsilon)$, in particular in the proximity of the reverse gel point (red curve in Fig. 5.6g). For the relatively poor solvent ($a_{pw} = 85.0$, green curve in Fig. 5.6g), the distance-based mass loss remains close to zero throughout the degradation indicating that almost the entire mass remains agglomerated with the largest agglomerate. This is also apparent from the snapshots in Fig. 5.6e-f, which show that majority of broken-off fragments remain aggregated in the close proximity to the nanogel particle (for example, in Fig. 5.6f only the highlighted part in the center of the agglomerate is the nanogel particle).

Understanding fractional mass loss from the largest agglomerate in solvents of various qualities allows one to understand dependence of the radius of gyration of the nanogel degrading

in these solvents as a function of the extent of degradation reaction. At the onset of degradation ($\epsilon = -1$), the radius of gyration depends on the equilibrium degree of swelling in the solvent of a chosen quality and as anticipated decreases with the decrease in solvent quality. To characterize a relative change in the radius of gyration depending on solvent quality, we plot the dependence of $R_g$ scaled by the value of $R_g$ prior to degradation for each case as a function of the proximity to the reverse gel point (Fig. 5.6h). As degradation occurs the nanogel in good solvent shows the highest relative increase in $R_g$ (black curve in Fig. 5.6h). As discussed above, an effective decrease in the crosslink density enables higher absorption of water within the polymer network and thus an increased swelling of the nanogel is observed in a good solvent. For the gel degrading in solvent of relatively poor quality ($a_{ps} = 85.0$, green curve in Fig. 5.6h), the $R_g$ remains nearly constant until relative extent of degradation reaches about $\epsilon \approx -0.4$; this is consistent with the above observation that up to this point there is essentially no mass loss from the largest agglomerate (green curve in Fig. 5.6g). Further increase in $\epsilon$ upon approaching reverse gel point results in the decrease in $R_g$ , which is consistent with mass loss due to the fragments diffusing away from the nanogel as seen in Fig. 5.6g. Intermediate solvent quality ($a_{ps} = 82$, red curve in Fig. 5.6h) still leads to the swelling of the gel particle due to the decrease in crosslink density, however the relative increase in $R_g$ is less pronounced than that in the good solvent case.

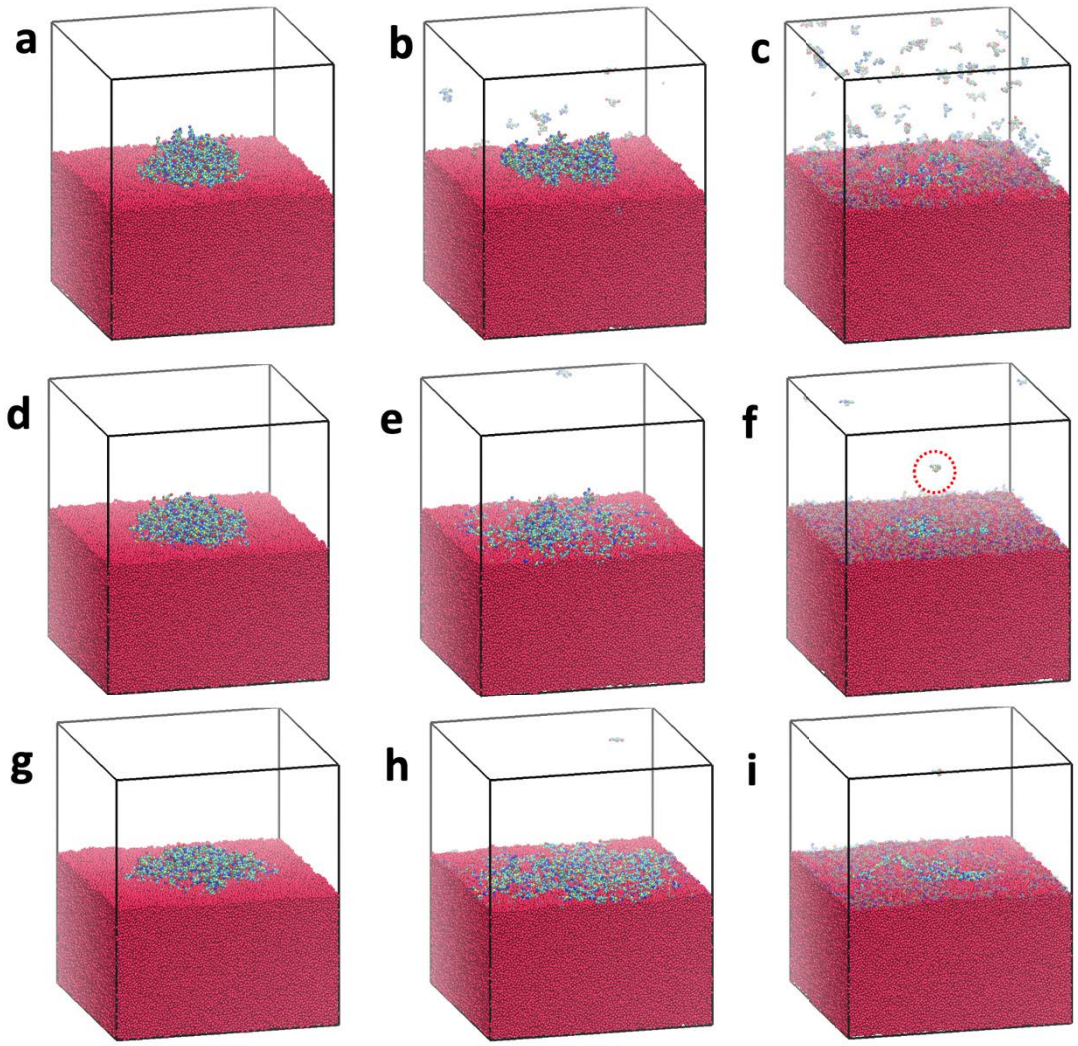


**Figure 5.7.** Snapshots of the nanogel degrading at an interface with the oil-water interaction parameter (a-c) $\mathbf{a_{ow} = 100}$ , (d-f) $\mathbf{a_{ow} = 120}$ and (g-i) $\mathbf{a_{ow} = 150}$ at (a, d, g) t=0, (b, e, h) t=10,000 and (c, f, i) t=22,000.

Similar to the effect of solvent quality in case of degradation in a single solvent, the interaction between the two liquids affects the kinetics of erosion and spreading of nanogel at the

liquid-liquid interface. As introduced in the model section, we consider three sets of liquid-liquid interaction parameters, $a_{ow} = 100, 120$ and $150$. Increasing $a_{ow}$ results in a stronger repulsion and correspondingly higher interfacial tension between the two liquids. The snapshots for degradation of a nanogel particle at the interface with $a_{ow} = 100$, 120 and 150 are shown in Fig. 5.7a-c, Fig. 5.7d-f and Fig. 5.7g-i, respectively. For the cases with higher repulsion ($a_{ow} = 120$ and $150$), all the fragments formed during degradation remain at the interface for the entire duration of the process (see Fig. 5.7d-i). A small fraction of fragments, such as fragments formed somewhat away from the interface (as the ones circled in Fig. 5.7f), diffuse within the liquid phase before adsorbing onto the interface. Once adsorbed at the interface, these fragments do not detach from the interface and remain adsorbed. For the case with $a_{ow} = 100$ (the case with lowest interfacial tension considered), a notable fraction of fragments remains in the liquid phase without adsorption onto the interface (see Fig. 5.7a-c). This difference in adsorption is seen quantitatively in the evolution of the number of contacts between the beads of the two liquid phases in Fig. 5.8a. The cases of three different interfaces with $a_{ow} = 100, 120$ and $150$ are represented in Fig. 5.8 by black, red, and green curves, respectively. As the nanogel degrades at the interface, the number of contacts between the two liquids decreases due to spreading of the remnant nanogel and broken-off fragments over the interface. For the case of $a_{ow} = 100$, this decrease is relatively moderate with respect to the other two cases. The difference in the observed behavior can be attributed to the relatively smaller energy gain due to shielding of the unfavorable oil-water interactions upon fragment adsorption onto the interface.

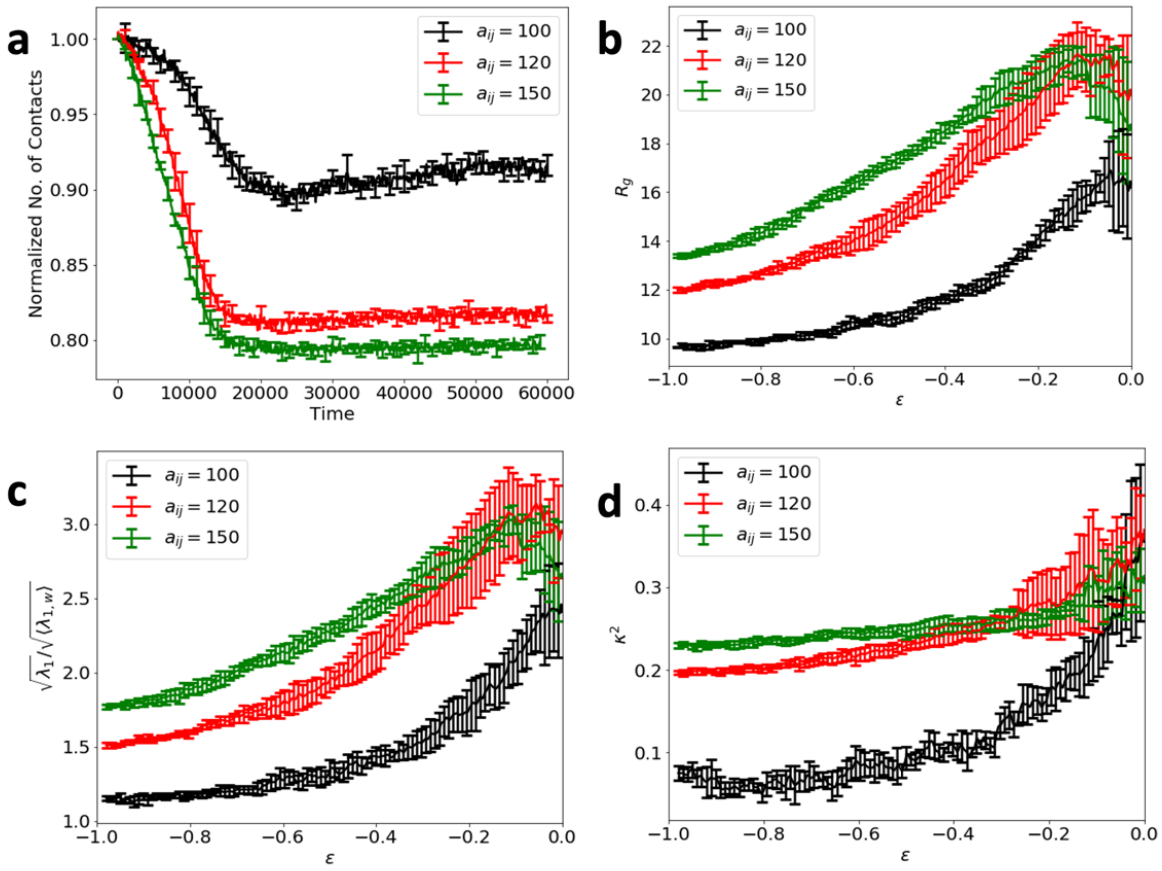


**Figure 5.8. Effects of liquid-liquid interaction parameter.** Evolution of **(a)** the number of contacts between two liquid phases, (**b**) radius of gyration, (**c**) extent of spreading, and (**d**) shape anisotropy for a nanogel particle degrading at the interface with $a_{ow} = 100$ (black curves), $a_{ow} = 120$ (red curves) and $a_{ow} = 150$ (green curves). All quantities are averaged over five simulations with error bars representing standard deviation. The data in (**a**) is normalized by the initial number of contacts for each case.

Our results show that this decrease in total interfacial energy due to spreading of small fragments at the interface with $a_{ow} = 100$ is not sufficient to compensate for introducing relatively unfavorable contacts of polymer with oil with respect to that with water (recall that

$a_{po} > a_{pw}$) along with the decrease in entropy due to interfacial confinement of these fragments. For the interfaces with $a_{ow} = 120$ and $a_{ow} = 150$, the decrease in interfacial energy upon fragment adsorption onto the interface is correspondingly higher, hence it is energetically favorable for the fragments to remain adsorbed decreasing the number of liquid-liquid contacts.

Evolution of the radius of gyration, extent of interfacial spreading, and shape anisotropy, $\kappa^2$, of the nanogels with the proximity to the reverse gel point are provided in Fig. 5.8b-d. The extent of spreading, $e$, is defined as[68]:

$$e(\epsilon) = \frac{\sqrt{\lambda_1(\epsilon)}}{<\sqrt{\lambda_{1,w}}>}, \tag{5.6}$$

where $\lambda_1(\epsilon)$ is the largest eigenvalue of the gyration tensor during degradation, and $\langle\sqrt{\lambda_{1,w}}\rangle = 5.58$ in reduced units of length is the average of the square root of the largest eigenvalue during equilibration in the water phase. All three characteristics provide information only about the remnant nanogel (the largest topological cluster in the system) and not about spreading of the smaller fragments. The initial values of $R_g$ prior to degradation increase with an increase in $a_{ow}$. This trend is in agreement with prior studies, which demonstrated enhanced stretching of nanogels at interfaces with higher interfacial tension[135]. Correspondingly, the initial extent of spreading for the nanogel at the interface with $a_{ow} = 100$ is the lowest ($e \approx 1.1$ prior to degradation) and increases with an increase in $a_{ow}$. In all cases considered, extent of spreading increases while approaching the reverse gel point, reaching nearly three-fold extension ($e \approx 2.75$) for the two interfaces with higher interfacial tension. Note that the relative extent of spreading with respect to that at the onset of degradation is most pronounced for the gels at the interface with $a_{ow} = 100$. This difference in the relative extent of spreading can be understood by following variation in the shape anisotropy of the nanogels during their spreading over various interfaces. The gel adsorbed at the interface with relatively low interfacial tension ($a_{ow} = 100$) attains close to a hemispherical

shape with $\kappa^2 \approx 0.10$ for the gel with chosen crosslink density. The same nanogel spreads and flattens more with an increase in $a_{ow}$, attaining more anisotropic shapes with values of $\kappa^2 \approx 0.20$ and $\kappa^2 \approx 0.22$ for the remaining two cases, respectively (thereby approaching 0.25 corresponding to a flat shape). As degradation occurs the $\kappa^2$ for nanogel at all interfaces increases with the increase being highest for the $a_{ow} = 100$ interface. Near the reverse gel point, nanogels at all three interfaces probed attain similar values of $\kappa^2 \approx 0.36$ with relatively large error bars. This value however remains lower than the values for the largest cluster at late times after the reverse gelation transition as reported above.

To summarize, these studies demonstrate that controlled degradation effectively promotes spreading of the remnant nanoparticle for all interfacial properties probed in this work. Specifically, the extent of spreading increases with an increase in the extent of degradation. The nanogel attains relatively flat shapes during the entire degradation process for two cases of interfaces with relatively high interfacial tension. For the same two cases, the fragments broken-off from the nanogel are adsorbed onto the interface thereby notably decreasing a number of unfavorable oil-water contacts. For the lowest interfacial tension considered, large fraction of the broken-off fragments remains dispersed in the water phase. Hence, this study shows that controlled degradation can be used to promote spreading of the nanogels at the soft interfaces and concurrently control location of the broken-of fragments to either be dispersed in the good solvent or to be controllably deposited at the interface.

### 5.4 Conclusions

Via DPD simulations, we characterized the degradation of nanogels suspended in a solvent and those adsorbed at the liquid-liquid interface [156]. In both scenarios, nanogels undergo a reverse gelation transition with the reverse gel point depending on the number of

polymeric precursors constituting the original nanogel. We identified the reverse gel points in various scenarios via peak values of the reduced weight average degree of polymerization. Our results demonstrate [156] that the reverse gel point follows a scaling relation $p_c^{\infty} + cN_p^{-\sigma}$ with respect to the number of polymer precursors , $N_p$, with the exponent $\sigma = 0.7$ and $p_c^{\infty} = 0.39$, which in turn is the value predicted by the bond percolation theory on a diamond lattice[110]. Further, in both scenarios we characterized the structural characteristics of the remnant nanogels along with the spatiotemporal distribution of polymeric fragments released during degradation as a function of proximity to the reverse gel point. Our results demonstrate distinct differences in structural characteristics of degrading nanogels depending on its environments. Nanogel degradation in a good solvent results in approximately uniform swelling of the remnant particle due to the decrease in crosslink density for the moderate relative extent of degradation reaction, $\epsilon \approx [-1: -0.38]$; within this range of $\epsilon$, the particle keeps approximately spherical shape ($\kappa^2 \approx 0$), while $R_g$ gradually increases. On the contrary, the shape anisotropy $\kappa^2$ increases nearly monotonically from the onset of degradation with an increase in $\epsilon$ for the gels degrading at the interface, indicating that initial shape of the nanogel adsorbed at the interface is nearly immediately lost upon degradation since bond breaking promotes interfacial spreading. We demonstrate that the overall degradation process including mass loss from the nanogel is significantly affected by the nature of the polymer-solvent interactions. Further, for the nanogels initially adsorbed at the liquid-liquid interface, shape changes and spreading of the remnant nanogel along with dispersion of detaching fragments

is affected significantly by the interfacial tension between the two incompatible liquids. For lower interfacial tension, some of the detaching fragments disperse to the liquid phase with higher affinity to polymer beads. Our results clearly demonstrate that controlled degradation of the nanogels adsorbed at liquid-liquid interfaces results in an enhanced extent of spreading and provides a means to control interfacial properties at the nanoscale. Further, our results provide insights on using controlled degradation to dynamically tune shapes of nanocarriers and nanoscale topography at a liquid-liquid interface. Devanshu Thakar is acknowledged for conducting simulations corresponding to the data sets A-E listed in Table 5.1 and for contributing to some of the analysis for these simulations during his summer internship. The work described in this chapter is published in the Macromolecules. The corresponding journal article is ref. [156] of the dissertation and the permission to reproduce this work in this chapter is included in Appendix B of this dissertation. The data for each plot in this chapter is also available publicly at https://doi.org/10.5281/zenodo.7410537.

# CHAPTER SIX

# Modeling controlled thermal degradation of polyolefins under a local temperature gradient

## 6.1 Motivation and background

### *6.1.1 Importance of polyolefin recycling and challenges with traditional approach*

Polyolefins, among the most abundantly used polymers in the world accounting for more than half of global primary polymer production[166], find applications in a wide range of industries[17]. Despite their widespread use, only a small fraction of polyolefins are recycled in the present day[17, 166]. For instance, only 14% of the total post-consumer packaging waste is collected for recycling[166], out of which only 2% is effectively recycled to the same or similar quality applications[166]. The traditional approach to recycling these polymers involves thermal degradation of the material in an attempt to recover the monomer[166]. However, this process often leads to the formation of several side products, which decrease the yield of the degradation reaction. This chapter outlines initial work towards exploring an alternative approach for recycling polyolefins that can potentially overcome these challenges. Specifically, this chapter aims to simulate degradation of polyolefins to shorter length oligomers which can be recycled or upcycled into useful products. To achieve this goal, our collaborators are currently introducing microwave absorbing materials into the bulk of the polyolefinic materials. When subject to pulsed microwave irradiation, these materials can be heated up to temperatures at which thermal degradation of the polyolefin takes place. The long-term goal of the simulation work is to inform concurrent experiments about optimal conditions to carry out the microwave assisted degradation. Using the simulation and experiment in tandem, a target molecular weight and dispersity in the polymer melt is aimed to be achieved. Overall, the goal of this project is to develop a more efficient and

sustainable approach to recycling polyolefins, which can have a significant impact on the environment and the economy.

Within this broad goal, the specific focus of this chapter will be on setting up an appropriate modeling approach that captures relevant details such as local temperature dependence of degradation reaction kinetics, molecular weight dependence of the diffusivity of polymers, and the ability to simulate a local temperature gradient from the surface of the microwave absorber to the bulk of the polymer material.

*6.1.2 Diffusivity of polyethylene melt*

Polyethylene melt properties depend on both temperature and polymer molecular weight. The self-diffusivity of polyethylene melts ($D$) is known to follow Rouse ($D \propto M^{-1}$) and reptation ($D \propto M^{-2}$)[167-170] regimes below and above the critical entanglement molecular weight, respectively. The temperature dependence of polyethylene melt viscosity follows an Arrhenius dependance[171, 172]:

$$D = D_0 \exp\left(-\frac{E_D}{RT}\right), \tag{6.1}$$

where $D_0$ is a pre-exponential factor and the activation energy $E_D \approx 30\ \mathrm{kJ/mol}$. Overall, the self-diffusion constant for polyethylene varies several orders of magnitude $10^{-5} - 10^{-11}\ cm^2/s$ [167-172] depending on both the temperature and molecular weight at which the measurement is performed. In simulations of polymer melts, the diffusivity is measured via the mean squared displacement of the center of masses of polymer chains[62, 173]. Transition from the rouse to reptation scaling at sufficiently high molecular weights of linear polymers has been observed in both coarse-grained molecular dynamics[173] and DPD with mSRP[62] simulations.

*6.1.3 Thermal degradation of polyethylene*

Thermal degradation of polyethylene (PE) is reported to occur primarily via random scission mechanism.[18, 174] Fig. 6.1 below shows a schematic of the degradation mechanism.

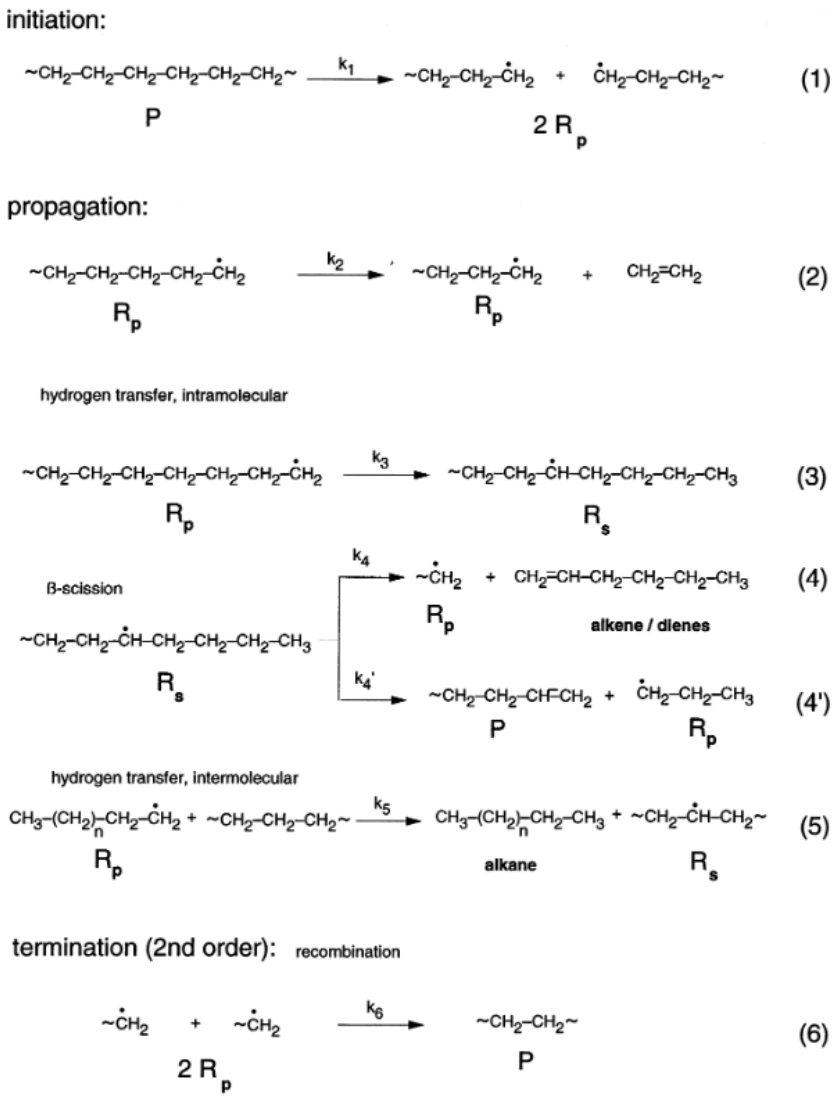


**Figure 6.1.** Schematic pathway of thermal degradation of polyethylene. Reproduced from ref. [18] with permission from Elsevier.

The degradation is initiated by random scission of the polymer chain into primary radicals, as shown in step 1 of Fig. 6.1. The free radical initiation is followed by propagation via intra/inter molecular hydrogen transfer and $\beta$ scission reactions (steps 2-5), while termination is assumed to occur via recombination[18, 174] (shown in step 6). In addition to random scission, a chain end scission reaction is also possible as shown in Fig. 6.2.

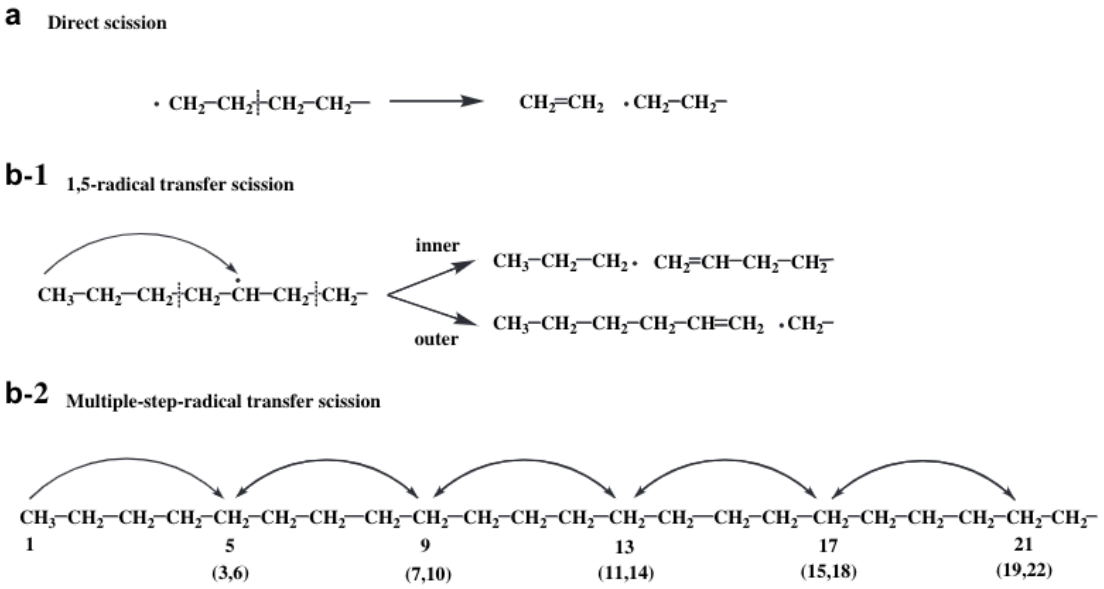


**Figure 6.2.** Mechanism of chain-end scission reaction of polyethylene. Reproduced from ref. [175] with permission from Elsevier.

During the random scission reaction, bond cleavage follows first order kinetics which, assuming Arrhenius dependance of the rate constant, can be written as[176]:

$$\frac{dx}{dt} = k(T)(1 - x), \tag{6.2}$$

where $x$ is the fraction of bonds broken, $k(T) = k_0 \exp\left(-\frac{E_b}{RT}\right)$ is the temperature dependent degradation rate constant, $k_0$ is the pre-exponential factor, and $E_b$ activation energy for the bond breaking reaction.

In experiments, thermal degradation is often studied in terms of the degree of mass conversion[18, 176, 177] ($\alpha$), which has the same form as the fractional mass loss defined in chapter four:

$$\alpha(t) = \frac{\left(m_0 - m(t)\right)}{m_0}, \tag{6.3}$$

where $m_0$ is the mass of a sample at the beginning of the experiment and $m(t)$ is the mass at time $t$ during thermal degradation. Mass loss occurs primarily due to volatilization of low molecular weight products formed during degradation. Prior theoretical and simulation work has focused on predicting the degradation kinetics via the degree of mass conversion. The degradation kinetics are often written in terms of the degree of mass conversion as:

$$\frac{d\alpha}{dt} = \kappa f(\alpha), \tag{6.4}$$

where $\kappa$ is a rate constant given via the Arrhenius form $\kappa = \kappa_0 \exp\left(-\frac{E_m}{RT}\right)$, $\kappa_0$ is the pre-exponential factor, $E_m$ is an activation energy for the mass degradation kinetics and $f(\alpha)$ is a function dependent on the kinetic model for the degradation process. The activation energy for mass loss during the degradation process has been reported to be conversion dependent and in the range of $150 - 250\ kJ/mol$.[18, 176-178].

Several models for $f(\alpha)$ have been proposed in literature[176], ranging from models that assume n-th order reaction kinetics[18] ($f(\alpha) = \alpha^n$) to models that relate the bond cleavage kinetics to the mass loss[176]. As the overall thermal degradation mechanism is complex (see Figs. 6.1 and 6.2 above), it is not trivial to relate the bond cleavage kinetics to the mass conversion

kinetics. For simplicity, simulation approaches typically only consider the first step of the degradation reactions[21, 175, 179], i.e. either random scission or chain end scission or both, and there are limited studies considering the possibility of recombination of molecules[180]. Since initial bond breaking pre-dominantly occurs via random scission[18, 21, 174] in thermal degradation of polyethylene, we will describe the modeling of random scission process in more detail. Fig. 6.3 below shows a schematic of the random scission mechanism applied in the stochastic modeling of polyethylene thermal degradation[21].

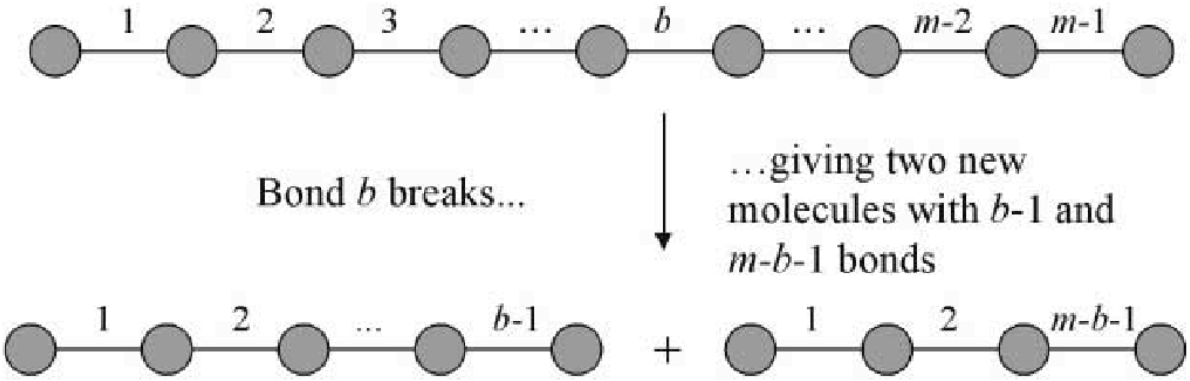


**Figure 6.3.** Schematic of the random scission mechanism in linear polyethylene chain. Reproduced from ref. [21] with permission from Elsevier.

As shown in Fig. 6.3 above, random scission is typically assumed to occur at only one site at a time in any polymer chain and hence leads to an increase of one molecule per scission event[21, 175, 179]. Consider that at some point during the random scission, a fraction $x$ of the total bonds have broken and there are $N_i(x)$ polymer chains with $i$ as their degree of polymerization. As random scission continues, some of these $N_i(x)$ chains disintegrate into smaller fragments while

some chains are formed as a consequence of disintegration of longer chains into chains with $i$ repeat units. Overall, the rate equation for $N_i(x)$ can be written as[179]:

$$\frac{dN_i}{dt} = -k(T)(i-1)N_i + 2k(T)\sum_{j=i+1}^{N} N_j \tag{6.5}$$

where, $N$ is the maximum initial degree of polymerization. The first term on the right-hand side of equation (6.5) represents the rate of disappearance of chains with $i$ repeat units and the second term represents their rate of formation. The total number bonds in the chains with $i$ repeat units is given by $(i-1)N_i$ and, since the scission of any one of these bonds would result in a chain disappearing, hence the rate of disappearance is $-k(T)(i-1)N_i$. Now, consider a chain with $i+m$ repeat units, where $m > 0$. The scission of such a chain, either at the $m^{th}$ bond or at the $i^{th}$ bond would result in the formation of a chain with $i$ repeat units. Hence, for each such chain with more than $i$ repeat units, there are two possible scission reactions that can produce a chain with $i$ repeat units leading to a rate of formation given by $2k(T)\Sigma_{\mathrm{j=i+1}}N_j$. Substituting $dt = \frac{dx}{k(T)(1-x)}$ from equation (6.2) above for the first order kinetics, we obtain the equation[21],

$$\frac{dN_i}{dx} = -\frac{(i-1)N_i}{1-x} + \frac{2}{1-x}\sum_{j=i+1}^{n} N_j \tag{6.6}$$

Assuming as in ref. [21], a solution in the form

$$N_i(x) = Ax^s(1-x)^{i-1}, \tag{6.7}$$

equation (6.6) can be rewritten as

$$\frac{d}{dx}\left(Ax^s(1-x)^{i-1}\right) = -(i-1)Ax^s(1-x)^{i-2} + 2Ax^s\sum_{j=i+1}^{n}(1-x)^{j-2} \tag{6.8}$$

For a large value of the maximum initial degree of polymerization, $N \to \infty$, the summation in the last term can be calculated analytically as $\Sigma_{j=i+1}^{\infty}(1-x)^{j-2} = (1-x)^{i-1}/x$. Using this summation, equation (6.8) can be simplified as:

$$(1-x)^{i-1} s x^{s-1} = 2x^{s-1}(1-x)^{i-1}, \tag{6.9}$$

which gives $s = 2$. The constant A remains to be determined. We can use the information so far to determine the number fraction of chains with $i$ monomers, $n_i(x) = \frac{N_i(x)}{\Sigma_{i=1}^{N} N_i(x)}$, as:

$$n_i(x) = \frac{Ax^2(1-x)^{i-1}}{Ax^2 \sum_{i=1}^{n}(1-x)^{i-1}}. \tag{6.10}$$

For the limit of $N \to \infty$, $\sum_{i=1}^{\infty}(1-x)^{i-1} = 1/x$ which leads to further simplification of equation (6.10) to:

$$n_i(x) = x(1-x)^{i-1}. \tag{6.11}$$

The above number fraction distribution during random scission is identical to the well-known most probable distribution during any step growth polymerization reaction, also known as Flory or Flory-Schulz[181, 182] distribution. The latter is typically described in terms of the fraction of bonds formed $p = 1 - x$. This similarity is expected since, the random scission reaction is essentially reverse of the step growth polymerization process[183].

From the above information, we can also calculate the weight fraction distribution, $w_i(x)$,

$$w_i(x) = \frac{iN_i(x)}{\Sigma_{i=1}^{\infty} iN_i(x)} \tag{6.12}$$

$$w_i(x) = ix^2(1-x)^{i-1}. \tag{6.13}$$

To relate the bond cleavage kinetics with mass loss, those bond breaking reactions which result in the formation of volatile fragments need to be considered. To address this, theoretical approaches

typically define $L$ as the shortest degree of polymerization of non-volatile fragments[21, 174, 175, 179]. Hence, the non-volatile fraction of total mass remaining, $1 - \alpha(x)$, reads

$$1 - \alpha(x) = \frac{\Sigma_{i=L}^{\infty} i N_i(x)}{\Sigma_{i=1}^{\infty} i N_i(x)} \tag{6.14}$$

This leads to the Simha-Wall equation[22] that relates the fraction of bonds broken during random scission to $\alpha$ as:

$$\alpha(x) = 1 - (1 - x)^{L-1}[1 + x(L - 1)]. \tag{6.15}$$

The activation energy of bond breaking in degradation of polyethylene has been estimated to be ≈ 125kJ/mol[21, 174]. The average C-C bond energy is ≈ 348kJ/mol.[174, 184]

## 6.2 Methods

### *6.2.1 eDPD approach*

The energy conserving dissipative particle dynamics (eDPD) method[56] enables modeling of non-isothermal heat transport processes in polymers[56, 57]. This method can be used to model the thermal response of various polymeric systems such as colloids[185], micelles[72], polymer nanocomposites[71] and microgels[65]. Specifically, eDPD has been used to model the effect of particle-fluid interactions on the mobility of thermophoretic colloidal microswimmers[185]. Non-equilibrium processes involving changes in solvent affinity for polymers displaying either lower critical solution temperature (LCST) or upper critical solution temperature (UCST) type behavior can be explicitly modeled using the eDPD method[65]. This aspect has been used in modeling of reversible heat-stiffening of nanocomposites made from

cellulose nanocrystals grafted with a LCST polymer[71] and in modeling the transport of thermoresponsive micelles and vesicles through a non-isothermal fluid medium[72].

To enable energy conservation, the internal energy of a DPD bead has been introduced as an additional degree of freedom in the eDPD method. This leads to modifications to the form of the momentum conservation equations of the standard DPD method. The momentum conservation equations for eDPD have the following temperature dependent parameters:

$$a_{ij} = A_{ij}.\frac{k_B(T_i + T_j)}{2}, \tag{6.16}$$

$$w_D = w_R^2 = \left(1 - \frac{r}{r_c}\right)^s, \tag{6.17}$$

$$\sigma_{ij}^2 = \frac{4\gamma_{ij}k_B T_i T_j}{T_i + T_j}. \tag{6.18}$$

Here, the strength of the conservative force $a_{ij}$ can have a temperature dependence prescribed through the $A_{ij}$ parameter and $T_i$ is the temperature of $i^{th}$ bead. The function $A_{ij} = A_{ij}^* + \Delta A/(1 + \exp(\pm\omega(T_{ij} - T_0)))$ has been used to model LCST and UCST type polymers[65, 72]. The weight functions $w_D$ and $w_R$ are also chosen to be temperature dependent via the exponent $s$. The exact form of this temperature dependence will be discussed in more detail below.

In addition to the momentum conservation equations, the eDPD method also uses the following equations for conservation of total energy[56]:

$$\frac{d(m_i C_v T_i)}{dt} = \Sigma_{i \neq j}\left(q_{ij}^C + q_{ij}^V + q_{ij}^R\right), \tag{6.19}$$

$$q_{ij}^C = k_{ij} w_{CT}(r_{ij})\left(\frac{1}{T_i} - \frac{1}{T_j}\right), \tag{6.20}$$

$$q_{ij}^V = \frac{1}{2C_v}\left(w_D(r_{ij})\left[\gamma_{ij}(\boldsymbol{e_{ij}}.\boldsymbol{v_{ij}})^2 - \frac{(\sigma_{ij})^2}{m}\right] - \sigma_{ij} w_R(r_{ij})(\boldsymbol{e_{ij}}.\boldsymbol{v_{ij}})\zeta_{ij}\right), \tag{6.21}$$

$$q_{ij}^{R} = \beta_{ij} w_{RT}(r_{ij}) dt^{-\frac{1}{2}} \zeta_{ij}^{e}. \tag{6.22}$$

Here, $C_v$ is the dimensionless heat capacity of each eDPD bead with temperature $T_i$. The definition and choice of $C_v$ have been discussed in previous literature[56, 57] and details regarding our choice are provided below. The collisional ($q_{ij}^{C}$) and random ($q_{ij}^{R}$) heat fluxes together account for conduction of heat through the material. The viscous heat flux $\left(q_{ij}^{V}\right)$ accounts for viscous heating due to conversion of the particle's mechanical energy to heat. The strengths of the collisional and random heat fluxes $k_{ij}$ and $\beta_{ij}$ and are given as $k_{ij} = C_v^2 \kappa \left(T_i + T_j\right)^2 / 4k_B$ and $\beta_{ij}^2 = 2k_B k_{ij}$, where $\kappa$ is a mesoscopic heat friction parameter.

*6.2.2 Considerations for modeling temperature dependent thermal degradation*

In addition to the bond breaking conditions described in chapter three, there are certain additional constraints required to simulate random scission. For example, if the method of generating random numbers for each bond in the polymer chain is used without any additional constraints, it could lead to unphysical reactions such as simultaneous breaking of both bonds by which a bead is connected to the polymer chain. A bond length based constraint is introduced to ensure a maximum of one bond per DPD bead can break at a time. For each DPD bead, the bond with the longest length is identified as a potential candidate for attempting bond breaking. An attempt to break the bond, i.e. generation of a random number, is only carried out if the said bond is a potential candidate for both DPD beads that constitute this bond. Hence, random numbers are not generated for all bonds in the polymer chain but only a fraction of the total bonds at a particular time step are considered for the bond breaking reaction. Bond lengths at each time step follow a Gaussian distribution around the mean equilibrium bond length ($r_b$, described in chapter two) and the length of a particular bond can be thought of as a random sample from this distribution.

Whether a particular bond is longer or shorter than it's neighbors is rather random and, hence, at each time a random subset of bonds is considered for the bond breaking reaction. The fraction of bonds within a chain that are attempted to be broken would depend on the actual degree of polymerization of a particular chain. Taking as an example, the extreme case of chains with $N = 2$, any bond can potentially be broken, while it will certainly not be the case for longer chains. In section 6.3.4 below, we will look at the impact of this criteria on the overall degradation reaction kinetics.

As discussed in chapter three, we aim in this dissertation to introduce the framework to incorporate effects of the local environment on the degradation reaction. In general, kinetics of the degradation reaction depend on the local environment such as temperature or pH in the vicinity of the degradable bond. The dependence of reaction rate constant on local properties is represented mathematically by the Arrhenius relation:

$$k = k_0 \exp\left(-\frac{E_a}{RT}\right), \tag{6.23}$$

where $k_0$ is a pre-exponential factor, $E_a$ is the activation energy for the reaction, $R$ is the universal gas constant and, $T$ the local temperature. With this context, we introduce the temperature

dependence described in equation (6.23) into the degradation framework by modifying the reaction probability $P$, to depend on the local temperature as:

$$P = P_0 \exp\left(-\frac{E_a}{RT_l}\right), \tag{6.24}$$

where $T_l$ is the local temperature at the reaction site $T_l = \frac{(T_i+T_j)}{2}$, $T_i$ and $T_j$ is the eDPD temperature of bead $i$ and $j$, respectively.

*6.2.2 Measurement of diffusivity and viscosity of an eDPD liquid*

To begin setting up the eDPD model, we first aim to setup a system to simulate and reproduce physical properties such as the viscosity and diffusivity of a simple eDPD liquid[57]. For this purpose, we used the following parameters as introduced by Li et. al.[57]: bead number density $\rho = 4$, cut-off distance $r_c = 1.58$, strength of the conservative force $a_{ij} = 18.75\, k_B T$. The reference temperature $T^* = 300K$ is used to scale the dimensionless temperatures such that the temperatures ranging from 273K to 373K are equivalent to the dimensionless temperatures T = 0.91 to 1.25. The dimensionless heat capacity of a single eDPD bead $(C_v)$ is normalized by the Boltzmann constant $k_B^* = 1.381\text{x}10^{-23} JK^{-1}$ and is given by $C_v = C_v^* L^{*3}/\rho k_B^*$, where $C_v^*$ is the volumetric heat capacity and $L^*$ is the reference length. Using $C_v^* = 4.167\text{x}10^6 Jm^{-3}K^{-1}$ for water at 300K and a reference length $L^* = 11nm$ gives $C_v = 1.0\text{x}10^5$. To ensure accurate temperature dependence of the diffusivity and viscosity, we use the temperature dependent form of the exponent of the weighting function[57] $s = 0.41 + 1.9(T^2 - 1)$.

We determine the self-diffusion coefficient via the mean square displacement (MSD) of beads,

$$\langle \big(\boldsymbol{r}(t) - \boldsymbol{r}(0)\big)^2 \rangle = 6Dt, \tag{6.25}$$

where $< (\boldsymbol{r}(t) - \boldsymbol{r}(0))^2 >$ is the MSD and $D$ is the self-diffusivity of eDPD beads. The MSD for several temperatures is plotted as a function of time in Fig 6.4a below. As follows from the equation above, the self-diffusivity can be calculated from the slope of the lines in Fig. 6.4a.

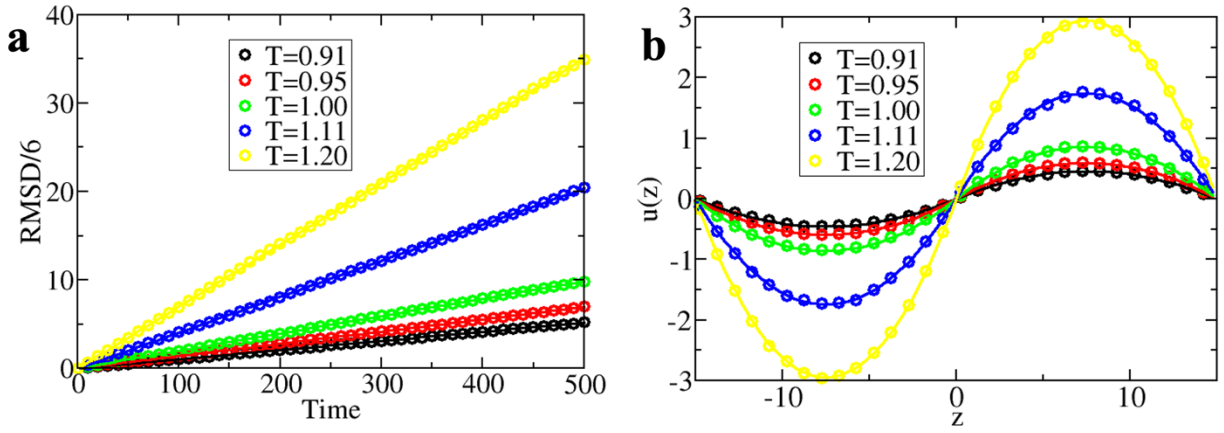


**Figure 6.4.** (**a**) Mean squared displacement of eDPD beads. (**b**) Velocity profile during perioidic Poiseuille flow of the eDPD system. A simulation box of 30x30x30 was used in each case.

To measure kinematic viscosity, we use the periodic Poiseuille flow method[57]. In this method, a periodic Poiseuille flow is generated in the simulation box by applying a body force to each eDPD bead. To generate Poiseuille flow the box is divided into two equal domains and an equal and opposite body force is applied to particles in each domain. The resulting velocity profile is then fitted to the analytical solution

$$u(z) = \frac{g_x z(d - |z|)}{2\nu}, \tag{6.26}$$

where $\nu$ is the kinematic viscosity, d = 15 is the half-length of the simulation box and $g_x = 0.2$ in dimensionless units is a body force on each eDPD particle. The resulting velocity profiles in our simulations along with the fitted analytical solutions are plotted in Fig. 6.4b.

Approximate analytical equations for the transport coefficients of a DPD fluid have been derived previously by several authors[57, 58, 186]. Specifically for the eDPD fluid with weight functions as described above, the self-diffusivity and kinematic viscosity are given as follows[57]:

$$D = \frac{3k_BT(s+1)(s+2)(s+3)}{8\pi\gamma\rho r_c^3}, \tag{6.27}$$

$$\nu = \frac{3k_BT(s+1)(s+2)(s+3)}{16\pi\gamma\rho r_c^3} + \frac{16\pi\gamma\rho r_c^5}{5(s+1)(s+2)(s+3)(s+4)(s+5)}. \tag{6.28}$$

Fig. 6.5 below shows the variation of kinematic viscosity and self-diffusivity of the eDPD fluid. As is seen in the plots in Fig. 6.5, numerical measurements of the transport coefficients agree well with the analytical expressions above. It has also been shown in literature[57] that these values agree well with the measured experimental values for water.

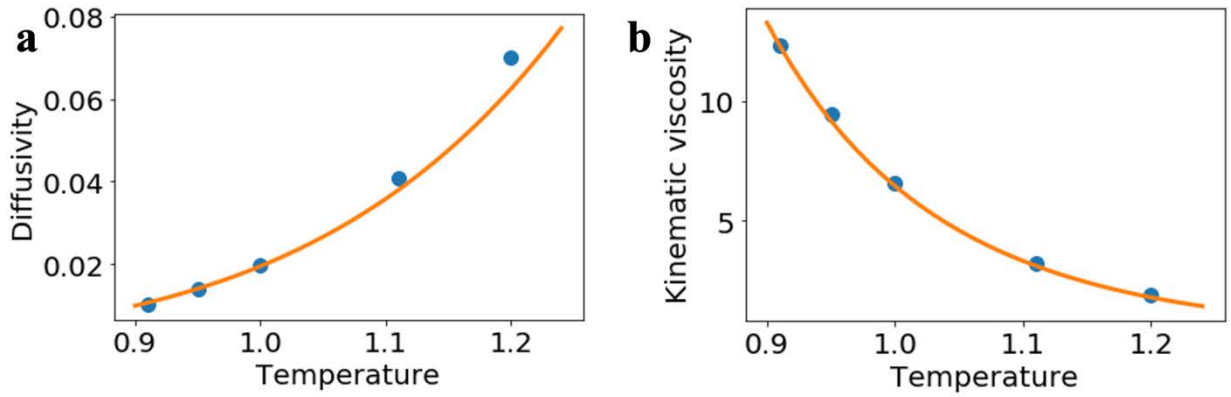


**Figure 6.5.** Temperature dependence of (**a**) diffusivity and (**b**) kinematic viscosity of the eDPD fluid measured numerically from simulations (symbols) and calculated as per analytical expressions (solid lines).

Hence, so far we have reproduced results from previous literature[57] for the properties of liquids modeled using the eDPD approach. Next, we will focus on the parameter choice for our model eDPD polymer melt and analyze properties such as the thermal conductivity, self-diffusion constant and structure of polymer chains of the simulated polyolefin melt.

## 6.3 Results and Discussion

### *6.3.1 Measuring thermal conductivity*

In the above section, we demonstrated temperature dependence of the properties of an eDPD liquid. As shown above for the mass diffusivity and kinematic viscosity, the thermal conductivity is also a measured output from eDPD simulations. For measuring thermal conductivity, we used DPD parameters as introduced in chapter three: $\rho = 3$, cut-off distance $r_c = 1.0$, strength of the conservative force $a_{ij} = 78k_BT$. For the choice of eDPD parameters in this preliminary study, we set [57], $C_v = C_v^* L^{*3}/\rho k_B^*$, where $C_v^*$ is the volumetric heat capacity and $L^*$ is the reference length. It had been shown that [57] $C_v^* = 4.167\text{x}10^6 Jm^{-3}K^{-1}$ for water at 300K and a reference length $L^* = 11nm$ gives $C_v = 1.33\text{x}10^5$. As in the previous section, the same temperature dependence of the power for the weighting function, $s = 0.41 + 1.9(T^2 - 1)$, is used. It should be noted here that alternate choices for $s$ and $C_v$ have been used in previous eDPD simulations of polymers[65, 72, 187]. For example, $s = 2$ and $C_v = 10^3$, along with the heat friction coefficient $\kappa = 10^{-3}$ have been used in eDPD simulations of thermoresponsive polymers[65]. Hence in addition to the preliminary choice of eDPD parameters in this chapter, more detailed analysis for the choice of these parameters is planned to be conducted in the future

to ensure that the thermal conductivity and diffusivity of simulated melts demonstrate expected dependences with molecular weight and temperature.

Using the above parameters, we conducted the following experiment to setup a temperature gradient. First, eDPD beads were equilibrated for 20,000 timesteps in a 40x40x40 simulation box with periodic boundaries and the temperature was set to be uniform throughout $T_0 = 1.0$. Then, a boundary layer of beads within a distance $\delta = 3$ from both y-periodic faces was made immobile, these immobile beads are colored red in Fig. 6.6a while the mobile eDPD beads are colored blue. In addition to this, to ensure minimal crossing of beads across the periodic face an additional soft repulsion potential $U_{wall} = 1000 * (h - h_c)^2$ was added to all beads within a distance $h$ ($\leq h_c = 1$) from the periodic walls. This system was then further equilibrated for an additional 20,000 time steps. After the second equilibration, a slight fluctuation was observed in the density at the interface between the mobile and immobile phases which is shown by the red curve in Fig. 6.6b. This fluctuation is evident compared to the homogenous density distribution after the first equilibration step (shown by black curve in Fig. 6.6b) and has a maximum magnitude of less than 1% inside the mobile region.

At the end of the second equilibration, the temperatures of the two immobile regions were changed such that the region near the lower y-boundary had a colder temperature of $T_c^w = 0.9$ and the upper region had a hotter temperature of $T_h^w = 1.1$. The evolution of temperature profiles inside the simulation box is shown in Fig. 6.6c. As is evident in Fig. 6.6c, the temperature evolution is well described by analytical solutions of the heat equation. Slight deviations from the analytical solution are observed at later times. This is attributed to the fact that our choice of conservative interaction parameters leads to a density gradient in the eDPD liquid as the temperature gradient evolves.

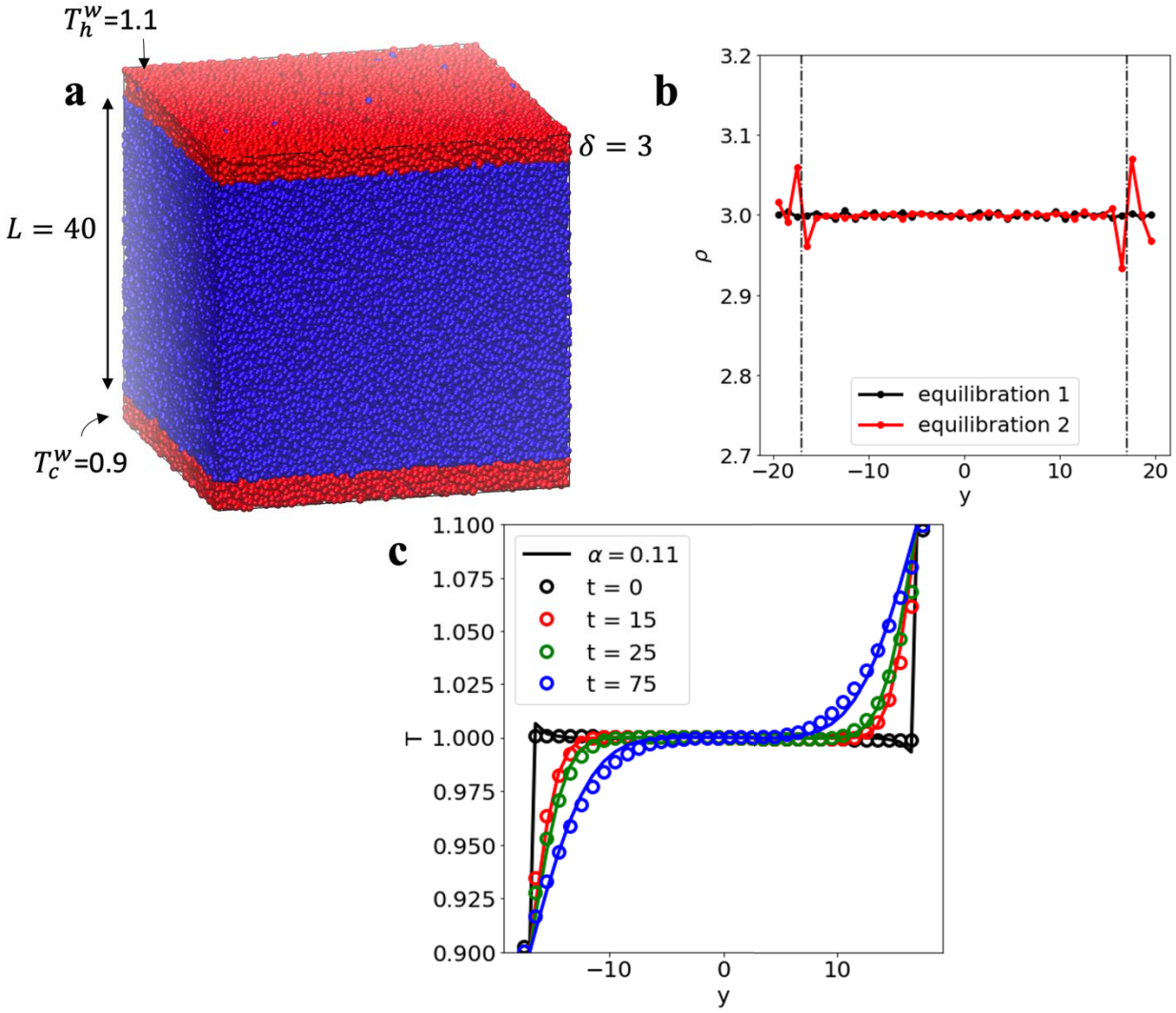


**Figure 6.6.** (**a**) Snapshot of the simulation box after the second equilibration step, see text for details. The red and blue beads indicate the immobile and mobile phases respectively. (**b**) Number density of eDPD beads inside the simulation box at the end of the first (black) and second (red) equilibrations. The dashed lines indicate the interface between the mobile and immobile phases. (**c**) Temperature profiles inside the simulation box at t=0 (black), t=15 (red), t=25 (green) and t=75 (blue). The symbols indicate measurements from eDPD simulations and lines indicate analytical solutions of the heat equation.

The variation of density as a function of temperature is expected in liquids and is not accounted for in the form of the heat equation we used. To obtain the thermal diffusivity $\alpha$ we fitted the temperature values from the eDPD simulations to the analytical solution of heat equation at t=15. The fitted value of thermal diffusivity $\alpha = 0.11\, r_c^2 \tau^{-1}$ agrees well with the theoretical estimate of the macroscopic thermal diffusivity in eDPD simulations provided in literature[57, 188]:

$$\alpha = \frac{k}{\rho C_v} = \frac{2\pi\rho}{315 k_B} \kappa C_v r_C^5 = 0.12 r_c^2 \tau^{-1}. \tag{6.24}$$

**Table 6.1.** Details of the simulated systems for determining properties of eDPD melts

| **N** | **L** | **Total simulation time** | **Measurement time** $t_M$ | $\frac{\langle R^2 \rangle}{\langle R_g^2 \rangle}$ |
|---|---|---|---|---|
| 8 | 20 | $50000\tau$ | $100\tau$ | 5.69 |
| 10 | 20 | $50000\tau$ | $100\tau$ | 5.78 |
| 15 | 20 | $50000\tau$ | $100\tau$ | 5.89 |
| 20 | 20 | $100000\tau$ | $100\tau$ | 5.93 |
| 30 | 30 | $50000\tau$ | $100\tau$ | 5.97 |
| 40 | 40 | $200000\tau$ | $100\tau$ | 5.97 |
| 60 | 40 | $300000\tau$ | $300\tau$ | 5.99 |
| 80 | 40 | $300000\tau$ | $300\tau$ | 6.00 |
| 100 | 40 | $300000\tau$ | $300\tau$ | 6.00 |
| 120 | 40 | $300000\tau$ | $300\tau$ | 6.03 |

*6.3.2 Static and dynamic properties of the eDPD melt*

The starting structure of the eDPD melt is modeled using linear polymers with $N$ beads per chain placed randomly in a cubic simulation box with side length $L$. Each bead is assigned a constant initial temperature $T_i = 1.0$. Table 6.1 provides a summary of the details of all the simulated systems.

Longer total simulation times and larger box sizes were chosen for the melts of longer polymers since longer chains have longer relaxation times and larger sizes. In addition, since the overall simulation times are much longer for the longer chains, snapshots were saved after longer intervals of time (see measurement time in Table 6.1) to reduce the overall file sizes. For each of the simulations, the trajectory up to $t = 10{,}000$ in reduced time units was considered as an equilibration phase by the end of which, chains are expected to reach a random coil configuration. Only the trajectory after $t = 10{,}000$ was considered for measurements of properties of the polymer melts. Fig. 6.7a,b shows snapshots of 8 randomly chosen chains for $N = 8$ and $N = 120$ simulations after the entire simulations have finished.

To ensure that the polymer chains in our model obey random walk statistics, we measure the mean squared radius of gyration $\langle R_g^2 \rangle$ and the mean squared end-to-end distance $\langle R^2 \rangle$ for the melt,

$$\langle R_g^2 \rangle = \frac{1}{N} \langle \sum_{i=1}^{N} (\boldsymbol{r}_i - \boldsymbol{r}_{com})^2 \rangle, \tag{6.25}$$

$$\langle R^2 \rangle = \langle (\boldsymbol{r}_1 - \boldsymbol{r}_N)^2 \rangle, \tag{6.26}$$

respectively, where $\boldsymbol{r}_i$ is the position of bead $i$ in a chain, $\boldsymbol{r}_{com} = \frac{1}{N} \Sigma_i \boldsymbol{r}_i$ is the center of mass of a chain, and $\langle\ \rangle$ represents an average over all chains. Fig. 6.7c shows both $\langle R_g^2 \rangle$ and $\langle R^2 \rangle$ as a function of $N - 1$ for all the simulations listed in Table 6.1. Both of these quantities are measured

from the data of the last 100 saved frames and scale linearly with $N-1$ as expected for the random coil polymer configuration[173]. In addition, the ratio $\frac{\langle R^2 \rangle}{\langle R_g^2 \rangle} \approx 6$ for each of the $N$ considered, see values in Table 6.1, which is also expected for random coils[173].

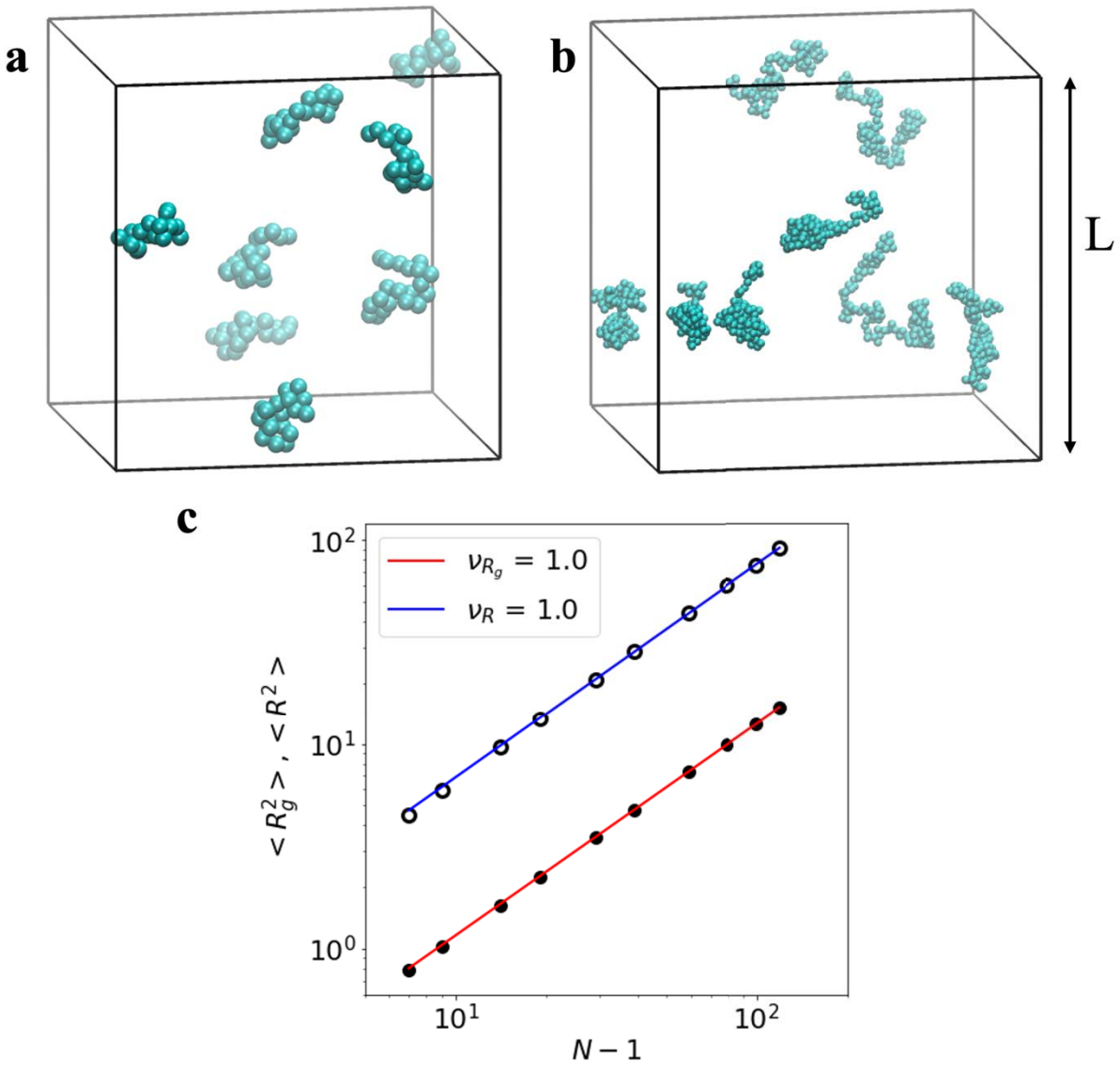


**Figure 6.7.** Snapshots of polymer chains in the equilibrated simulation box with (**a**) $N = 20$ and (**b**) $N = 120$ beads per chain. Only eight chains are shown in each box while the rest are hidden. The simulation box size is $L = 20$ in **a** and $L = 40$ in **b**. (**c**) Scaling of the mean squared end-to-

end distance (open symbols, blue line) and mean squared radius of gyration (closed symbols, red line). The lines show fitting to a $+ bN^{\nu}$. Both quantities follow expected scaling for random coils with $\nu = 1.0$.

To measure the diffusion constant of chains, we measured the mean squared displacement of the chain center of mass ($g_3(t)$) starting from the configuration at $t = 10{,}000$, i.e. after the initial equilibration phase. This quantity is typically utilized in simulation studies[62, 173] to measure diffusion constants of melts and is defined as:

$$g_3(t) = \langle [\boldsymbol{r}_{com}(t) - \boldsymbol{r}_{com}(0)]^2 \rangle \tag{6.27}$$

According to reptation theory, at late times $g_3$ is expected to scale as $g_3 \propto t^1$ and the diffusion constant of polymer chains can be derived from late time values of $g_3(t)$ using the relation,

$$g_3(t) \approx 6Dt. \tag{6.28}$$

The time evolution of $g_3(t)$ for melts with $N = 8$ to $N = 120$ is shown in Fig. 6.8a. Diffusion constants are measured by fitting the $g_3$ values from the last 100 measured frames of the simulations with the equation (6.28) above. The dependence of the melt diffusion constant on the number of bonds in each chain of the melt is plotted in Fig. 6.8b.

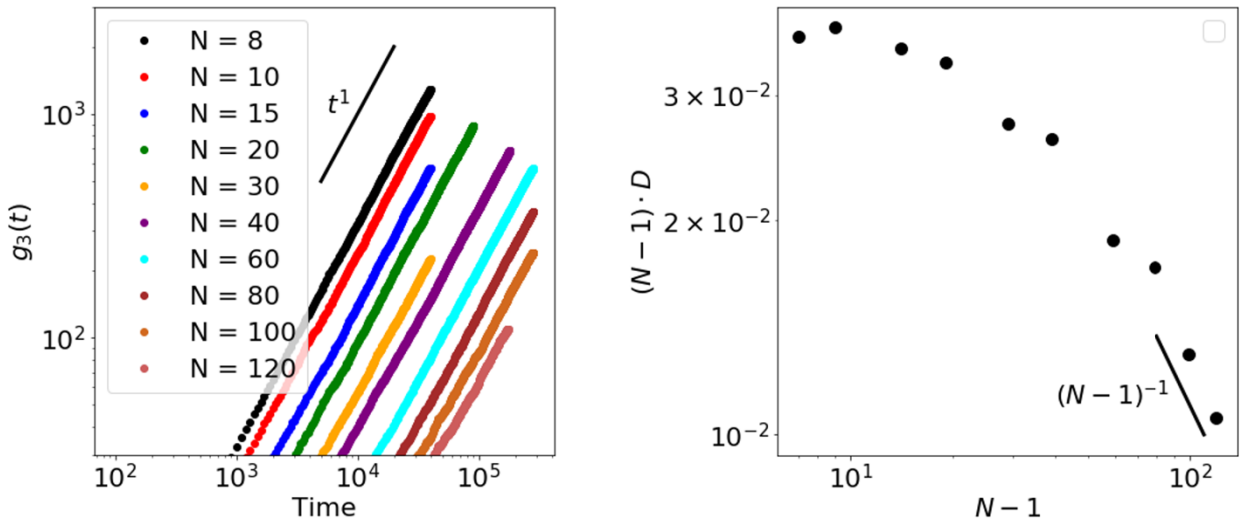


**Figure 6.8.** (**a**) Evolution of the mean squared displacement of the chain center of mass, $g_3(t)$ for melts of polymers with different degrees of polymerization ($N$) as described in the legend. (**b**) Dependence of the product $(N-1)\,.\,D$ on the number of bonds in the chains $N-1$.

The data of diffusion constant demonstrates that up to $N \approx 15$, an approximately constant value of the product $(N-1)\,.\,D$ is observed. This is expected from the Rouse theory of diffusive motion where $D \propto (N-1)^{-1}$. For $N \geq 80$, the trend starts to approach the reptation regime scaling $D \propto (N-1)^{-2}$. This trend in the diffusion constant data indicates that in the higher region of the studied molecular weights, $80 \leq N \leq 120$, the polymer melts are in a transition regime between the pure rouse and reptation dynamics.

*6.3.3 Modeling random scission under thermal degradation*

In section 6.2.2 above, we described additional criteria apart from those outlined in chapter three of this dissertation, to model random scission of linear polymer chains. To evaluate what fraction of the total bonds can potentially be broken, we applied the above approach to a melt with initial degree of polymerization $N = 120$. We tracked the progress of degradation by tracking the

fraction of bonds intact, $p = 1 - x$. The data in Fig. 6.9 above shows that the thermal degradation reaction follows first order kinetics with a rate constant $k \approx 0.38P(T)/\tau_R$. The factor 0.38 appears here since, as discussed in section 6.2.2 above, the degradation probability is evaluated for only a fraction of all the bonds.

To further confirm that our simulations follow trends expected for the random scission process we tracked the evolution of number fraction $(n_i(x))$ and weight fraction$(w_i(x))$ distribution of polymer chains as shown in Fig. 6.10 below.

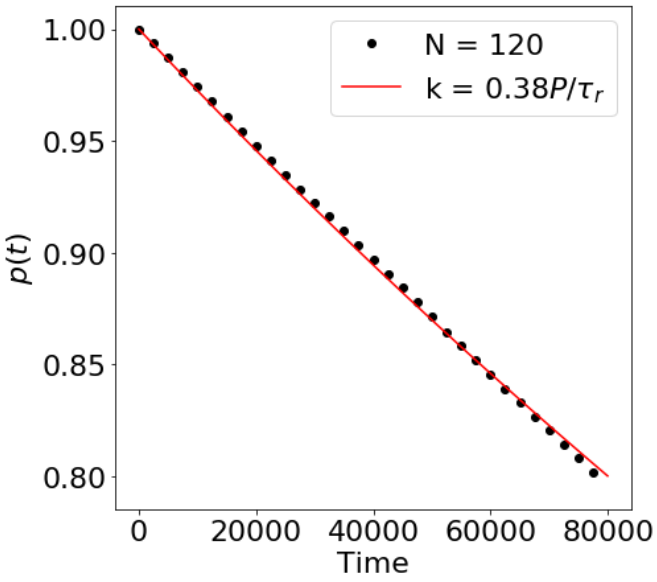


**Figure 6.9.** Evolution of the fraction of bonds intact during simulation of an eDPD melt with $N = 120$. The symbols represent data from an eDPD simulation and the line represents a fitting of the first order equation $p = \exp(-kt)$. The values $P(T) = 900\exp(-32/T)$, $\tau_R = 0.1$ were used for the degradation simulation which was carried out at $T = 1.53$ in reduced DPD units corresponding to $T = 450\ ^0\text{C}$.

Both of these distributions follow the trends expected from the Flory-Schulz distribution for sufficiently high initial values of the degree of polymerization. Symbols of different color represent data corresponding to time instants during the eDPD simulations with specific fraction of bonds broken as mentioned in the legend. Lines represent plots of equations (6.11) and (6.13) above. Highest deviations in the trends are observed near the limit $x \to 0$ (see data for $x = 0.01$) which is the limiting case where almost no bonds are broken. In this limit, the expected distribution would be the unimolecular starting distribution we used for these simulations which is different from the Flory-Schulz prediction.

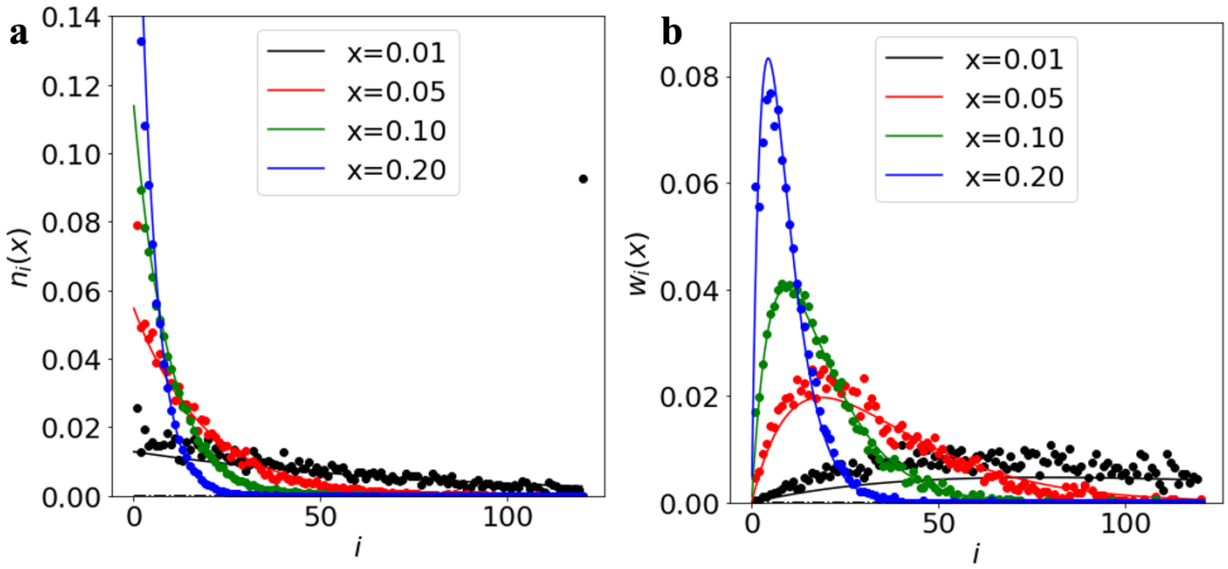


**Figure: 6.10.** (a) Number fraction $n_i(x)$ and (b) weight fraction $w_i(x)$ distributions during random scission of polymer melt with initial degree of polymerization $N = 120$. Symbols represent data from eDPD simulations while lines representing plots of equations 6.11 and 6.13 above.

Outliers are also observed for the longest chain length in the simulation, $N = 120$ since the statistics are poor for this chain length and the number of chains with $N = 120$ only keeps decreasing throughout the simulation.

### 6.4 Conclusions

We have developed an initial framework for simulating the thermal degradation of polyolefin melts. The framework uses a combined eDPD-mSRP approach to enable simulation of temperature gradients in entangled polymer melts. The approach used in this chapter produces polymer melts that show a transition from the rouse to reptation regime dynamics with increasing molecular weight. The polymer chains at different molecular weights also demonstrate random walk statistics expected from polymer chains in the melt state[173]. When a temperature gradient is applied across the simulation box, temperature profile in the bulk of the simulated single bead liquid system follows the trend expected from the heat conduction equation. Further, we conducted a preliminary simulation of the thermal degradation of this polymer melt. The degradation reaction constant in this model is dependent on the local temperature at which the degradation reaction is carried out. The simulated degradation reaction results in a distribution of polymer chain lengths in the melt that follows the expected Flory-Schulz distribution for the random scission process[183]. The initial framework outlined in this chapter can be expanded further to simulate the local temperature dependent thermal degradation of polyolefin melts.

# CHAPTER SEVEN

# Conclusions

In this dissertation, we developed a framework for the simulation of degradation of polymer networks and melts at the mesoscale. We used the DPD mesoscale simulation technique along with mSRP to model the dynamics of polymers while avoiding unphysical crossing of the polymer chains. We used a stochastic approach to model bond breaking during the degradation process and implemented a modified form of the mSRP-DPD formulation to allow for dynamically switching off the extra mSRP repulsion as bonds break. The developed simulation protocol also allows for switching on mSRP repulsion upon bond formation and was used in our lab for simulating the hydrosilylation reaction during synthesis of polymer derived ceramics[85].

The framework described above was used to simulate photo-controlled degradation and erosion in tetra-PEG based hydrogel films. We tracked the progress of degradation reaction by measuring the fraction of degradable bonds intact along with the evolution of molecular weight distribution in the system. We identified a reverse gel point as a critical fraction of bonds broken and then analyzed fractional mass loss from the hydrogel film as a function of the relative extent of the degradation reaction with respect to the reverse gel point. We also analyzed the impact of mass loss on properties such as the film thickness and crosslink density.

In addition to simulating hydrogel films, we also simulated degradation of finite sized nanogel particles either suspended in a single solvent or adsorbed at the interface between two incompatible liquids. We identified the dependence of the reverse gel point of these particles on the total number of polymer precursors. We also analyzed the evolution of nanogel shape and size during degradation and studied the impact of surrounding local conditions, such as the solvent quality, on the evolution of these properties. During degradation in a good solvent, the nanogel

undergoes homogenous swelling. The degree of swelling during degradation in a single solvent decreases with a decrease in solvent quality. At the interface, the decrease in elasticity of nanogels as degradation proceeds leads to increased spreading and interfacial coverage. The adsorption of polymeric fragments formed during degradation along with the extent of spreading of the remnant nanogel depends on the interfacial tension between the two liquids. The simulation protocol developed for this work was implemented as pair srp/react[83] in the LAMMPS software[75-77] to enable usage by the broader scientific community. Various aspects of the above work, discussed in chapters 2-5, have been published in four journal articles [68, 70, 84, 85]; one journal article has been accepted for publication and a review on this topic has been submitted as a book chapter[189]. Additionally, the data regarding nanogel degradation work is publicly available on Zenodo: https://doi.org/10.5281/zenodo.7410537

Lastly, we discussed our initial progress towards developing a framework for simulating local temperature dependent thermal degradation of polyolefin melts. For this purpose, we used the energy conserving dissipative particle dynamics (eDPD) technique which allows simulation of temperature gradients in the simulation. The simulated polymer melts show a transition from the rouse to reptation regime dynamics with increasing molecular weight. We simulated thermal degradation of this polymer melt via the random scission mechanism with a degradation rate constant dependent on the local temperature of the polymer. Our initial degradation simulations result in molecular weight distributions in the melt that follow the expected Flory-Schulz distribution for the random scission process[183]. Overall, the last chapter outlines initial simulation framework towards that will aid in exploring an alternative approach for recycling polyolefins.

# REFERENCES


1. Shieh, P., et al., *Cleavable comonomers enable degradable, recyclable thermoset plastics.* Nature, 2020. **583**(7817): p. 542-547.

2. Whajah, B., et al., *Catalytic Depolymerization of Waste Polyolefins by Induction Heating: Selective Alkane/Alkene Production.* Industrial & Engineering Chemistry Research, 2021. **60**(42): p. 15141-15150.

3. LeValley, P.J., et al., *Photolabile Linkers: Exploiting Labile Bond Chemistry to Control Mode and Rate of Hydrogel Degradation and Protein Release.* Journal of the American Chemical Society, 2020. **142**(10): p. 4671-4679.

4. Lin, C.C. and K.S. Anseth, *PEG Hydrogels for the Controlled Release of Biomolecules in Regenerative Medicine.* Pharmaceutical Research, 2009. **26**(3): p. 631-643.

5. Azagarsamy, M.A., et al., *Photocontrolled Nanoparticles for On-Demand Release of Proteins.* Biomacromolecules, 2012. **13**(8): p. 2219-2224.

6. Truong, V.X., et al., *Wavelength-Selective Coupling and Decoupling of Polymer Chains via Reversible 2+2 Photocycloaddition of Styrylpyrene for Construction of Cytocompatible Photodynamic Hydrogels.* Acs Macro Letters, 2018. **7**(4): p. 464-469.

7. McKinnon, D.D., et al., *Design and Characterization of a Synthetically Accessible, Photodegradable Hydrogel for User-Directed Formation of Neural Networks.* Biomacromolecules, 2014. **15**(7): p. 2808-2816.

8. Metters, A.T., C.N. Bowman, and K.S. Anseth, *A statistical kinetic model for the bulk degradation of PLA-b-PEG-b-PLA hydrogel networks.* Journal of Physical Chemistry B, 2000. **104**(30): p. 7043-7049.

9. Göpferich, A., *Polymer Bulk Erosion.* Macromolecules, 1997. **30**(9): p. 2598-2604.

10. Kloxin, A.M., et al., *Photodegradable Hydrogels for Dynamic Tuning of Physical and Chemical Properties.* Science, 2009. **324**(5923): p. 59-63.

11. Frey, M.T. and Y.L. Wang, *A photo-modulatable material for probing cellular responses to substrate rigidity.* Soft Matter, 2009. **5**(9): p. 1918-1924.

12. Wong, D.Y., et al., *Photodegradable Hydrogels to Generate Positive and Negative Features over Multiple Length Scales.* Macromolecules, 2010. **43**(6): p. 2824-2831.

13. Luo, Y. and M.S. Shoichet, *A photolabile hydrogel for guided three-dimensional cell growth and migration.* Nature Materials, 2004. **3**(4): p. 249-253.

14. Griffin, D.R. and A.M. Kasko, *Photoselective Delivery of Model Therapeutics from Hydrogels.* Acs Macro Letters, 2012. **1**(11): p. 1330-1334.

15. Ramanan, V.V., et al., *Photocleavable side groups to spatially alter hydrogel properties and cellular interactions.* Journal of Materials Chemistry, 2010. **20**(40): p. 8920-8926.

16. Kloxin, A.M., et al., *Tunable Hydrogels for External Manipulation of Cellular Microenvironments through Controlled Photodegradation.* Advanced Materials, 2010. **22**(1): p. 61-+.

17. Geyer, R., J.R. Jambeck, and K.L. Law, *Production, use, and fate of all plastics ever made.* Science Advances, 2017. **3**(7).

18. Bockhorn, H., et al., *Kinetic study on the thermal degradation of polypropylene and polyethylene.* Journal of Analytical and Applied Pyrolysis, 1999. **48**(2): p. 93-109.

19. Ashley, G.W., et al., *Hydrogel drug delivery system with predictable and tunable drug release and degradation rates.* Proceedings of the National Academy of Sciences of the United States of America, 2013. **110**(6): p. 2318-2323.

20. Jahanmir, G., M.J. Abdekhodaie, and Y. Chau, *Stochastic Modeling of Degradation Behavior of Hydrogels.* Macromolecules, 2018. **51**(11): p. 3941-3952.

21. Staggs, J.E.J., *Modelling random scission of linear polymers.* Polymer Degradation and Stability, 2002. **76**(1): p. 37-44.

22. Simha, R. and L.A. Wall, *KINETICS OF CHAIN DEPOLYMERIZATION.* Journal of Physical Chemistry, 1952. **56**(6): p. 707-715.

23. Sakai, T., et al., *Design and fabrication of a high-strength hydrogel with ideally homogeneous network structure from tetrahedron-like macromonomers.* Macromolecules, 2008. **41**(14): p. 5379-5384.

24. Azagarsamy, M.A., et al., *Coumarin-Based Photodegradable Hydrogel: Design, Synthesis, Gelation, and Degradation Kinetics.* Acs Macro Letters, 2014. **3**(6): p. 515-519.

25. Brown, T.E., I.A. Marozas, and K.S. Anseth, *Amplified Photodegradation of Cell-Laden Hydrogels via an Addition-Fragmentation Chain Transfer Reaction.* Advanced Materials, 2017. **29**(11): p. 7.

26. Li, X., et al., *Precise Control and Prediction of Hydrogel Degradation Behavior.* Macromolecules, 2011. **44**(9): p. 3567-3571.

27. Truong, V.X., F.Y. Li, and J.S. Forsythe, *Photolabile Hydrogels Responsive to Broad Spectrum Visible Light for Selective Cell Release.* Acs Applied Materials & Interfaces, 2017. **9**(38): p. 32441-32445.

28. Villiou, M., J.I. Paez, and A. del Campo, *Photodegradable Hydrogels for Cell Encapsulation and Tissue Adhesion.* Acs Applied Materials & Interfaces, 2020. **12**(34): p. 37862-37872.

29. Metters, A. and J. Hubbell, *Network formation and degradation behavior of hydrogels formed by Michael-type addition reactions.* Biomacromolecules, 2005. **6**(1): p. 290-301.

30. Reddy, S.K., K.S. Anseth, and C.N. Bowman, *Modeling of network degradation in mixed step-chain growth polymerizations.* Polymer, 2005. **46**(12): p. 4212-4222.

31. Tibbitt, M.W., A.M. Kloxin, and K.S. Anseth, *Modeling controlled photodegradation in optically thick hydrogels.* Journal of Polymer Science Part a-Polymer Chemistry, 2013. **51**(9): p. 1899-1911.

32. Sridhar, S.L., et al., *Heterogeneity is key to hydrogel-based cartilage tissue regeneration.* Soft Matter, 2017. **13**(28): p. 4841-4855.

33. Hoogerbrugge, P.J. and J.M.V.A. Koelman, *Simulating Microscopic Hydrodynamic Phenomena with Dissipative Particle Dynamics.* Europhysics Letters (EPL), 1992. **19**(3): p. 155-160.

34. Groot, R.D. and P.B. Warren, *Dissipative particle dynamics: Bridging the gap between atomistic and mesoscopic simulation.* J. Chem. Phys., 1997. **107**(11): p. 4423-4435.

35. Espanol, P. and P.B. Warren, *Perspective: Dissipative Particle Dynamics.* J. Chem. Phys, 2017. **146**(15): p. 150901.

36. Groot, R.D. and K.L. Rabone, *Mesoscopic Simulation of Cell Membrane Damage, Morphology Change and Rupture by Nonionic Surfactants.* Biophys. J., 2001. **81**(2): p. 725-736.

37. Feng, Y.H., et al., *Dissipative Particle Dynamics Aided Design of Drug Delivery Systems: A Review.* Molecular Pharmaceutics, 2020. **17**(6): p. 1778-1799.

38. Wang, X., K.P. Santo, and A.V. Neimark, *Modeling Gas–Liquid Interfaces by Dissipative Particle Dynamics: Adsorption and Surface Tension of Cetyl Trimethyl Ammonium Bromide at the Air–Water Interface.* Langmuir, 2020. **36**(48): p. 14686-14698.

39. Santo, K.P. and A.V. Neimark, *Effects of metal-polymer complexation on structure and transport properties of metal-substituted polyelectrolyte membranes.* Journal of Colloid and Interface Science, 2021. **602**: p. 654-668.

40. Salib, I., et al., *Harnessing Fluid-Driven Vesicles To Pick Up and Drop Off Janus Particles.* ACS Nano, 2013. **7**(2): p. 1224-1238.

41. Dutt, M., et al., *Modeling the Self-Assembly of Lipids and Nanotubes in Solution: Forming Vesicles and Bicelles with Transmembrane Nanotube Channels.* ACS Nano, 2011. **5**(6): p. 4769-4782.

42. Shin, J.M., et al., *Morphological Evolution of Block Copolymer Particles: Effect of Solvent Evaporation Rate on Particle Shape and Morphology.* ACS Nano, 2017. **11**(2): p. 2133-2142.

43. Vishnyakov, A., M.T. Lee, and A.V. Neimark, *Prediction of the Critical Micelle Concentration of Nonionic Surfactants by Dissipative Particle Dynamics Simulations.* Journal of Physical Chemistry Letters, 2013. **4**(5): p. 797-802.

44. Mills, Z.G., W.B. Mao, and A. Alexeev, *Mesoscale modeling: solving complex flows in biology and biotechnology.* Trends in Biotechnology, 2013. **31**(7): p. 426-434.

45. Sirk, T.W., et al., *An enhanced entangled polymer model for dissipative particle dynamics.* The Journal of Chemical Physics, 2012. **136**(13): p. 134903.

46. Yong, X., et al., *Harnessing Interfacially-Active Nanorods to Regenerate Severed Polymer Gels.* Nano Letters, 2013. **13**(12): p. 6269-6274.

47. Liu, H., et al., *Influence of Surface-Initiated Polymerization Rate and Initiator Density on the Properties of Polymer Brushes.* Macromolecules, 2009. **42**(7): p. 2863-2872.

48. Lisal, M., J.K. Brennan, and W.R. Smith, *Mesoscale simulation of polymer reaction equilibrium: Combining dissipative particle dynamics with reaction ensemble Monte Carlo. I. Polydispersed polymer systems.* Journal of Chemical Physics, 2006. **125**(16).

49. Yong, X., O. Kuksenok, and A.C. Balazs, *Modeling free radical polymerization using dissipative particle dynamics.* Polymer, 2015. **72**: p. 217-225.

50. Singh, A., et al., *Photo-regeneration of severed gel with iniferter-mediated photo-growth.* Soft Matter, 2017. **13**(10): p. 1978-1987.

51. Singh, A., et al., *Tailoring the structure of polymer networks with iniferter-mediated photo-growth.* Polymer Chemistry, 2016. **7**(17): p. 2955-2964.

52. Yong, X., et al., *Harnessing Interfacially-Active Nanorods to Regenerate Severed Polymer Gels.* Nano Lett., 2013. **13**(12): p. 6269-6274.

53. Liu, Y., J. Aizenberg, and A.C. Balazs, *Using Dissipative Particle Dynamics to Model Effects of Chemical Reactions Occurring within Hydrogels.* Nanomaterials, 2021. **11**(10): p. 2764.

54. Kawagoe, Y., et al., *Thermoset resin curing simulation using quantum-chemical reaction path calculation and dissipative particle dynamics.* Soft Matter, 2021. **17**(28): p. 6707-6717.

55. Feng, Y.H., et al., *Mesoscopic Simulation for the Effect of Cross-Linking Reactions on the Drug Diffusion Properties in Microneedles.* Journal of Chemical Information and Modeling, 2021. **61**(8): p. 4000-4010.

56. Espanol, P., *Dissipative particle dynamics with energy conservation.* Europhysics Letters, 1997. **40**(6): p. 631-636.

57. Li, Z., et al., *Energy-conserving dissipative particle dynamics with temperature-dependent properties.* Journal of Computational Physics, 2014. **265**: p. 113-127.

58. Groot, R.D. and P.B. Warren, *Dissipative particle dynamics: Bridging the gap between atomistic and mesoscopic simulation.* Journal of Chemical Physics, 1997. **107**(11): p. 4423-4435.

59. Groot, R.D. and T.J. Madden, *Dynamic simulation of diblock copolymer microphase separation.* Journal of Chemical Physics, 1998. **108**(20): p. 8713-8724.

60. Nikolov, S., A. Fernandez-Nieves, and A. Alexeev, *Mesoscale modeling of microgel mechanics and kinetics through the swelling transition.* Applied Mathematics and Mechanics-English Edition, 2018. **39**(1): p. 47-62.

61. Tu, S.D., et al., *Mesoscale Modeling of Agglomeration of Molecular Bottlebrushes: Focus on Conformations and Clustering Criteria.* Polymers, 2022. **14**(12).

62. Sirk, T.W., et al., *An enhanced entangled polymer model for dissipative particle dynamics.* Journal of Chemical Physics, 2012. **136**(13): p. 11.

63. Nikunen, P., I. Vattulainen, and M. Karttunen, *Reptational dynamics in dissipative particle dynamics simulations of polymer melts.* Physical Review E, 2007. **75**(3).

64. Warren, P.E.a.P., *Statistical Mechanics of Dissipative Particle Dynamics.* EPL (Europhysics Letters), 1995. **30**(4): p. 191.

65. Li, Z., et al., *Mesoscale modeling of phase transition dynamics of thermoresponsive polymers.* Chemical Communications, 2015. **51**(55): p. 11038-11040.

66. Hoogerbrugge, P.J. and J. Koelman, *Simulating microscopic hydrodynamic phenomena with dissipative particle dynamics.* Europhysics Letters, 1992. **19**(3): p. 155-160.

67. Lee, M.T., et al., *Parametrization of Chain Molecules in Dissipative Particle Dynamics.* Journal of Physical Chemistry B, 2016. **120**(22): p. 4980-4991.

68. Choudhury, C.K., V. Palkar, and O. Kuksenok, *Computational Design of Nanostructured Soft Interfaces: Focus on Shape Changes and Spreading of Cubic Nanogels.* Langmuir, 2020. **36**(25): p. 7109-7123.

69. Kumar, S. and R.G. Larson, *Brownian dynamics simulations of flexible polymers with spring-spring repulsions.* Journal of Chemical Physics, 2001. **114**(15): p. 6937-6941.

70. Palkar, V. and O. Kuksenok, *Controlling Degradation and Erosion of Polymer Networks: Insights from Mesoscale Modeling.* Journal of Physical Chemistry B, 2022. **126**(1): p. 336-346.

71. Cudjoe, E., et al., *Biomimetic Reversible Heat-Stiffening Polymer Nanocomposites.* Acs Central Science, 2017. **3**(8): p. 886-894.

72. Tang, Y.H., et al., *Non-Equilibrium Dynamics of Vesicles and Micelles by Self-Assembly of Block Copolymers with Double Thermoresponsivity.* Macromolecules, 2016. **49**(7): p. 2895-2903.

73. Allen, M.P. and D.J. Tildesley, *Computer simulation of liquids*. 2017: Oxford university press.

74. Nikunen, P., M. Karttunen, and I. Vattulainen, *How would you integrate the equations of motion in dissipative particle dynamics simulations?* Computer Physics Communications, 2003. **153**(3): p. 407-423.

75. Plimpton, S., *Fast Parallel Algorithms for Short-Range Molecular Dynamics.* J. Comput. Phys., 1995. **117**(1): p. 1-19.

76. Thompson, A.P., et al., *LAMMPS-a flexible simulation tool for particle-based materials modeling at the atomic, meso, and continuum scales.* Computer Physics Communications, 2022. **271**.

77. *LAMMPS Molecular Dynamics Simulator*. Available from: http://lammps.org.

78. Humphrey, W., A. Dalke, and K. Schulten, *VMD: Visual molecular dynamics.* Journal of Molecular Graphics & Modelling, 1996. **14**(1): p. 33-38.

79. Griffin, D.R. and A.M. Kasko, *Photodegradable Macromers and Hydrogels for Live Cell Encapsulation and Release.* Journal of the American Chemical Society, 2012. **134**(31): p. 13103-13107.

80. Gissinger, J.R., B.D. Jensen, and K.E. Wise, *Modeling chemical reactions in classical molecular dynamics simulations.* Polymer, 2017. **128**: p. 211-217.

81. Akkermans, R.L.C., S. Toxvaerd, and W.J. Briels, *Molecular dynamics of polymer growth.* Journal of Chemical Physics, 1998. **109**(7): p. 2929-2940.

82. Sirk, T.W. *Pair style srp*. 2012 February 13, 2023]; Available from: https://docs.lammps.org/pair_srp.html#.

83. Palkar, V. *Pair style srp/react*. 2022 February 13, 2023]; Available from: https://docs.lammps.org/pair_srp.html#pair-style-srp-react-command.

84. Palkar, V., C.K. Choudhury, and O. Kuksenok, *Development of Dissipative Particle Dynamics framework for modeling hydrogels with degradable bonds.* Mrs Advances, 2020. **5**(17): p. 927-934.

85. Xiong, Y., et al., *Mesoscale Modeling of Phase Separation Controlled by Hydrosilylation in Polyhydromethylsiloxane (PHMS)-Containing Blends.* Nanomaterials, 2022. **12**(18).

86. Shih, H. and C.C. Lin, *Cross-Linking and Degradation of Step-Growth Hydrogels Formed by Thiol-Ene Photoclick Chemistry.* Biomacromolecules, 2012. **13**(7): p. 2003-2012.

87. Rubinstein, M. and R.H. Colby, *Polymer Physics*. 2003: OUP Oxford.

88. Chen, S.S. and X. Yong, *Dissipative particle dynamics modeling of hydrogel swelling by osmotic ensemble method.* Journal of Chemical Physics, 2018. **149**(9).

89. Gumerov, R.A., et al., *Amphiphilic microgels adsorbed at oil-water interfaces as mixers of two immiscible liquids.* Soft Matter, 2019. **15**(19): p. 3978-3986.

90. Yong, X., et al., *Stackable, Covalently Fused Gels: Repair and Composite Formation.* Macromolecules, 2015. **48**(4): p. 1169-1178.

91. Chen, S.S. and X. Yong, *Elastocapillary interactions of thermoresponsive microgels across the volume phase transition temperatures.* Journal of Colloid and Interface Science, 2021. **584**: p. 275-280.

92. Nikolov, S.V., A. Fernandez-Nieves, and A. Alexeev, *Behavior and mechanics of dense microgel suspensions.* Proceedings of the National Academy of Sciences of the United States of America, 2020. **117**(44): p. 27096-27103.

93. Anakhov, M.V., R.A. Gumerov, and I.I. Potemkin, *Stimuli-responsive aqueous microgels: properties and applications.* Mendeleev Communications, 2020. **30**(5): p. 555-562.

94. Madl, C.M., L.M. Katz, and S.C. Heilshorn, *Tuning Bulk Hydrogel Degradation by Simultaneous Control of Proteolytic Cleavage Kinetics and Hydrogel Network Architecture.* Acs Macro Letters, 2018. **7**(11): p. 1302-1307.

95. Richtering, W. and B.R. Saunders, *Gel architectures and their complexity.* Soft Matter, 2014. **10**(21): p. 3695-3702.

96. Rebello, N.J., H.K. Beech, and B.D. Olsen, *Adding the Effect of Topological Defects to the Flory-Rehner and Bray-Merrill Swelling Theories.* Acs Macro Letters, 2021. **10**(5): p. 531-537.

97. Milchev, A., J.P. Wittmer, and D.P. Landau, *Formation and equilibrium properties of living polymer brushes.* Journal of Chemical Physics, 2000. **112**(3): p. 1606-1615.

98. Jha, P.K., et al., *Study of volume phase transitions in polymeric nanogels by theoretically informed coarse-grained simulations.* Soft Matter, 2011. **7**(13): p. 5965-5975.

99. Schultz, K.M. and K.S. Anseth, *Monitoring degradation of matrix metalloproteinases-cleavable PEG hydrogels via multiple particle tracking microrheology.* Soft Matter, 2013. **9**(5): p. 1570-1579.

100. Kruger, A.J.D., et al., *A catalyst-free, temperature controlled gelation system for in-mold fabrication of microgels.* Chemical Communications, 2018. **54**(50): p. 6943-6946.

101. Gupta, A.M., R.C. Hendrickson, and C.W. Macosko, *MONTE-CARLO DESCRIPTION OF AF HOMOPOLYMERIZATION - DIFFUSIONAL EFFECTS.* Journal of Chemical Physics, 1991. **95**(3): p. 2097-2108.

102. Shy, L.Y., Y.K. Leung, and B.E. Eichinger, *CRITICAL EXPONENTS FOR OFF-LATTICE GELATION OF POLYMER-CHAINS.* Macromolecules, 1985. **18**(5): p. 983-986.

103. Somvarsky, J. and K. Dusek, *KINETIC MONTE-CARLO SIMULATION OF NETWORK FORMATION .2. EFFECT OF SYSTEM SIZE.* Polymer Bulletin, 1994. **33**(3): p. 377-384.

104. Flory, P.J., *Molecular size distribution in three dimensional polymers. I. Gelation.* Journal of the American Chemical Society, 1941. **63**: p. 3083-3090.

105. Macosko, C.W. and D.R. Miller, *NEW DERIVATION OF AVERAGE MOLECULAR-WEIGHTS OF NONLINEAR POLYMERS.* Macromolecules, 1976. **9**(2): p. 199-206.

106. Lin, T.S., et al., *Topological Structure of Networks Formed from Symmetric Four-Arm Precursors.* Macromolecules, 2018. **51**(3): p. 1224-1231.

107. Polanowski, P., et al., *Effect of dilution on branching and gelation in living copolymerization of monomer and divinyl cross-linker: Modeling using dynamic lattice liquid model (DLL) and Flory-Stockmayer (FS) model.* Polymer, 2011. **52**(22): p. 5092-5101.

108. Polanowski, P., J.K. Jeszka, and K. Matyjaszewski, *Modeling of branching and gelation in living copolymerization of monomer and divinyl cross-linker using dynamic lattice liquid model (DLL) and Flory-Stockmayer model.* Polymer, 2010. **51**(25): p. 6084-6092.

109. Flory, P.J., *Principles of Polymer Chemistry*. 1953: Cornell University Press.

110. Stauffer, D. and A. Aharony, *Introduction To Percolation Theory*. 1994: Taylor & Francis.

111. Sakai, T., et al., *Sol-gel transition behavior near critical concentration and connectivity.* Polymer Journal, 2016. **48**(5): p. 629-634.

112. Nishi, K., et al., *Experimental Observation of Two Features Unexpected from the Classical Theories of Rubber Elasticity.* Physical Review Letters, 2017. **119**(26).

113. Rankin, S.E., et al., *Dynamic Monte Carlo simulation of gelation with extensive cyclization.* Macromolecules, 2000. **33**(20): p. 7639-7648.

114. Spouge, J.L., *EQUILIBRIUM RING FORMATION IN POLYMER-SOLUTIONS.* Journal of Statistical Physics, 1986. **43**(1-2): p. 143-196.

115. Wang, R., et al., *Kinetic Monte Carlo Simulation for Quantification of the Gel Point of Polymer Networks.* Acs Macro Letters, 2017. **6**(12): p. 1414-1419.

116. Tanaka, Y., J.L. Stanford, and R. Stepto, *Interpretation of Gel Points of an Epoxy-Amine System Including Ring Formation and Unequal Reactivity: Measurements of Gel Points and Analyses on Ring Structures.* Macromolecules, 2012. **45**(17): p. 7197-7205.

117. Lang, M. and T. Muller, *Analysis of the Gel Point of Polymer Model Networks by Computer Simulations.* Macromolecules, 2020. **53**(2): p. 498-512.

118. Reid, R., et al., *Analytical and Simulation-Based Models for Drug Release and Gel-Degradation in a Tetra-PEG Hydrogel Drug-Delivery System.* Macromolecules, 2015. **48**(19): p. 7359-7369.

119. Lin, C.C. and A.T. Metters, *Hydrogels in controlled release formulations: Network design and mathematical modeling.* Advanced Drug Delivery Reviews, 2006. **58**(12-13): p. 1379-1408.

120. Clegg, J.R., et al., *Synthetic networks with tunable responsiveness, biodegradation, and molecular recognition for precision medicine applications.* Science Advances, 2019. **5**(9).

121. Lu, Y., et al., *Thermosensitive core-shell particles as carriers for Ag nanoparticles: Modulating the catalytic activity by a phase transition in networks.* Angewandte Chemie-International Edition, 2006. **45**(5): p. 813-816.

122. Kleinschmidt, D., et al., *Microgel organocatalysts: modulation of reaction rates at liquid–liquid interfaces.* Materials Advances, 2020. **1**(8): p. 2983-2993.

123. Destribats, M., et al., *Soft microgels as Pickering emulsion stabilisers: role of particle deformability.* Soft Matter, 2011. **7**(17): p. 7689-7698.

124. Miksch, C.E., et al., *4D Printing of Extrudable and Degradable Poly (Ethylene Glycol) Microgel Scaffolds for Multidimensional Cell Culture.* Small, 2022. **18**(36): p. 2200951.

125. Scotti, A., et al., *How Softness Matters in Soft Nanogels and Nanogel Assemblies.* Chemical Reviews, 2022. **122**(13): p. 11675-11700.

126. Karg, M., et al., *Nanogels and Microgels: From Model Colloids to Applications, Recent Developments, and Future Trends.* Langmuir, 2019. **35**(19): p. 6231-6255.

127. Caldwell, A.S., B.A. Aguado, and K.S. Anseth, *Designing microgels for cell culture and controlled assembly of tissue microenvironments.* Advanced functional materials, 2020. **30**(37): p. 1907670.

128. Brugger, B. and W. Richtering, *Emulsions stabilized by stimuli-sensitive poly(N-isopropylacrylamide)-co-methacrylic acid polymers: Microgels versus low molecular weight polymers.* Langmuir, 2008. **24**(15): p. 7769-7777.

129. Mourran, A., et al., *When Colloidal Particles Become Polymer Coils.* Langmuir, 2016. **32**(3): p. 723-730.

130. Klinger, D. and K. Landfester, *Photo-sensitive PMMA microgels: light-triggered swelling and degradation.* Soft Matter, 2011. **7**(4): p. 1426-1440.

131. Lopez, C.G. and W. Richtering, *Does Flory-Rehner theory quantitatively describe the swelling of thermoresponsive microgels?* Soft Matter, 2017. **13**(44): p. 8271-8280.

132. Hang, C., et al., *NIR and UV-responsive degradable hyaluronic acid nanogels for CD44-targeted and remotely triggered intracellular doxorubicin delivery.* Colloids and Surfaces B: Biointerfaces, 2017. **158**: p. 547-555.

133. Rumyantsev, A.M., R.A. Gumerov, and I.I. Potemkin, *A polymer microgel at a liquid–liquid interface: theory vs. computer simulations.* Soft Matter, 2016. **12**(32): p. 6799-6811.

134. Geisel, K., L. Isa, and W. Richtering, *Unraveling the 3D localization and deformation of responsive microgels at oil/water interfaces: a step forward in understanding soft emulsion stabilizers.* Langmuir, 2012. **28**(45): p. 15770-15776.

135. Vialetto, J., et al., *Influence of the interfacial tension on the microstructural and mechanical properties of microgels at fluid interfaces.* Journal of Colloid and Interface Science, 2022. **608**: p. 2584-2592.

136. Fernandez-Rodriguez, M.A., A. Martin-Molina, and J. Maldonado-Valderrama, *Microgels at interfaces, from mickering emulsions to flat interfaces and back.* Advances in Colloid and Interface Science, 2021. **288**.

137. Zhang, X., et al., *Micro-and nanogels with labile crosslinks–from synthesis to biomedical applications.* Chemical Society Reviews, 2015. **44**(7): p. 1948-1973.

138. South, A.B. and L.A. Lyon, *Direct Observation of Microgel Erosion via in-Liquid Atomic Force Microscopy.* Chemistry of Materials, 2010. **22**(10): p. 3300-3306.

139. Agrawal, G., et al., *Degradable microgels synthesized using reactive polyvinylalkoxysiloxanes as crosslinkers.* Soft Matter, 2013. **9**(22): p. 5380-5390.

140. Hwang, D.K., et al., *Stop-flow lithography for the production of shape-evolving degradable microgel particles.* Journal of the American Chemical Society, 2009. **131**(12): p. 4499-4504.

141. Smith, M.H., E.S. Herman, and L.A. Lyon, *Network deconstruction reveals network structure in responsive microgels.* The Journal of Physical Chemistry B, 2011. **115**(14): p. 3761-3764.

142. Español, P. and P.B. Warren, *Perspective: Dissipative particle dynamics.* The Journal of Chemical Physics, 2017. **146**(15): p. 150901.

143. Santo, K.P. and A.V. Neimark, *Dissipative particle dynamics simulations in colloid and interface science: A review.* Advances in Colloid and Interface Science, 2021: p. 102545.

144. Wei, L., et al., *Highly Oil-Repellent Thermoplastic Boundaries via Surface Delivery of CF3 Groups by Molecular Bottlebrush Additives.* ACS Applied Materials & Interfaces, 2020. **12**(34): p. 38626-38637.

145. Xiong, Y., et al., *Mesoscale Modeling of Phase Separation Controlled by Hydrosilylation in Polyhydromethylsiloxane (PHMS)-Containing Blends.* Nanomaterials, 2022. **12**(18): p. 3117.

146. Choudhury, C.K. and O. Kuksenok, *Native-Based Dissipative Particle Dynamics Approach for α-Helical Folding.* The Journal of Physical Chemistry B, 2020. **124**(50): p. 11379-11386.

147. Gao, L., et al., *Understanding Interfacial Nanoparticle Organization through Simulation and Theory: A Review.* Langmuir, 2022. **38**(37): p. 11137-11148.

148. Vishnyakov, A., et al., *Interactions of Crosslinked Polyacrylic Acid Polyelectrolyte Gels with Nonionic and Ionic Surfactants.* The Journal of Physical Chemistry B, 2021. **125**(50): p. 13817-13828.

149. Zhang, M., et al., *Effect of Fluorophobic Character upon Switching Nanoparticles in Polymer Films from Aggregated to Dispersed States Using Immersion Annealing.* ACS Applied Polymer Materials, 2022. **4**(10): p. 7042-7053.

150. Kravchenko, V.S., et al., *Self-Assembly of Molecular Brushes with Responsive Alternating Copolymer Side Chains.* Macromolecules, 2022. **55**(22): p. 10176-10187.

151. Gumerov, R.A., et al., *Amphiphilic microgels adsorbed at oil–water interfaces as mixers of two immiscible liquids.* Soft Matter, 2019. **15**(19): p. 3978-3986.

152. Schmidt, M.M., et al., *Influence of charges on the behavior of polyelectrolyte microgels confined to oil–water interfaces.* Langmuir, 2020. **36**(37): p. 11079-11093.

153. Nickel, A.C., et al., *Anisotropic Microgels Show Their Soft Side.* Langmuir, 2022. **38**(17): p. 5063-5080.

154. Geisel, K., et al., *Hollow and core–shell microgels at oil–water interfaces: Spreading of soft particles reduces the compressibility of the monolayer.* Langmuir, 2015. **31**(48): p. 13145-13154.

155. Gumerov, R.A., et al., *Mixing of Two Immiscible Liquids within the Polymer Microgel Adsorbed at Their Interface.* ACS Macro Letters, 2016. **5**(5): p. 612-616.

156. Palkar, V., D. Thakar, and O. Kuksenok, *Nanogel Degradation at Soft Interfaces and in Bulk: Tracking Shape Changes and Interfacial Spreading.* Macromolecules.

157. Lee, M.-T., et al., *Parametrization of Chain Molecules in Dissipative Particle Dynamics.* The Journal of Physical Chemistry B, 2016. **120**(22): p. 4980-4991.

158. Nair, N., et al., *Coarse-Grained Simulations of Polymer-Grafted Nanoparticles: Structural Stability and Interfacial Behavior.* J. Phys. Chem. B, 2016. **120**(35): p. 9523-9539.

159. Theodorou, D.N. and U.W. Suter, *SHAPE OF UNPERTURBED LINEAR-POLYMERS - POLYPROPYLENE.* Macromolecules, 1985. **18**(6): p. 1206-1214.

160. Lee, H., J.R. Baker, and R.G. Larson, *Molecular dynamics studies of the size, shape, and internal structure of 0% and 90% acetylated fifth-generation polyamidoamine dendrimers in water and methanol.* Journal of Physical Chemistry B, 2006. **110**(9): p. 4014-4019.

161. Jagodzinski, O., E. Eisenriegler, and K. Kremer, *Universal shape properties of open and closed polymer chains: Renormalization group analysis and Monte Carlo experiments.* Journal de Physique I, 1992. **2**(12): p. 2243-2279.

162. Narros, A., A.J. Moreno, and C.N. Likos, *Effects of Knots on Ring Polymers in Solvents of Varying Quality.* Macromolecules, 2013. **46**(9): p. 3654-3668.

163. Steinhauser, M.O., *A molecular dynamics study on universal properties of polymer chains in different solvent qualities. Part I. A review of linear chain properties.* The Journal of Chemical Physics, 2005. **122**(9): p. 094901.

164. Šomvársky, J. and K. Dušek, *Kinetic Monte-Carlo simulation of network formation.* Polymer Bulletin, 1994. **33**(3): p. 369-376.

165. Watt, J., R. Borhani, and A.K. Katsaggelos, *Machine Learning Refined: Foundations, Algorithms, and Applications.* Machine Learning Refined: Foundations, Algorithms, and Applications, 2016: p. 1-286.

166. Coates, G.W. and Y. Getzler, *Chemical recycling to monomer for an ideal, circular polymer economy.* Nature Reviews Materials, 2020. **5**(7): p. 501-516.

167. Pearson, D.S., et al., *VISCOSITY AND SELF-DIFFUSION COEFFICIENT OF LINEAR POLYETHYLENE.* Macromolecules, 1987. **20**(5): p. 1133-1141.

168. Klein, J. and B.J. Briscoe, *DIFFUSION OF LONG-CHAIN MOLECULES THROUGH BULK POLYETHELENE.* Proceedings of the Royal Society of London Series a-Mathematical Physical and Engineering Sciences, 1979. **365**(1720): p. 53-73.

169. Bachus, R. and R. Kimmich, *MOLECULAR-WEIGHT AND TEMPERATURE-DEPENDENCE OF SELF-DIFFUSION COEFFICIENTS IN POLYETHYLENE AND POLYSTYRENE MELTS INVESTIGATED USING A MODIFIED NMR FIELD-GRADIENT TECHNIQUE.* Polymer, 1983. **24**(8): p. 964-970.

170. Fleischer, G., *A CRITICAL RECONSIDERATION OF POLYMER SELF-DIFFUSION DATA MEASURED BY THE NMR PULSED FIELD GRADIENT TECHNIQUE.* Makromolekulare Chemie-Rapid Communications, 1985. **6**(7): p. 463-467.

171. Tao, H., T.P. Lodge, and E.D. von Meerwall, *Diffusivity and viscosity of concentrated hydrogenated polybutadiene solutions.* Macromolecules, 2000. **33**(5): p. 1747-1758.

172. Bartels, C.R., B. Crist, and W.W. Graessley, *SELF-DIFFUSION COEFFICIENT IN MELTS OF LINEAR-POLYMERS - CHAIN-LENGTH AND TEMPERATURE-DEPENDENCE FOR HYDROGENATED POLYBUTADIENE.* Macromolecules, 1984. **17**(12): p. 2702-2708.

173. Kremer, K. and G.S. Grest, *DYNAMICS OF ENTANGLED LINEAR POLYMER MELTS - A MOLECULAR-DYNAMICS SIMULATION.* Journal of Chemical Physics, 1990. **92**(8): p. 5057-5086.

174. Gao, Z.M., et al., *Calculation of activation energy from fraction of bonds broken for thermal degradation of polyethylene.* Polymer Degradation and Stability, 2003. **81**(1): p. 125-130.

175. Ueno, T., E. Nakashima, and K. Takeda, *Quantitative analysis of random scission and chain-end scission in the thermal degradation of polyethylene.* Polymer Degradation and Stability, 2010. **95**(9): p. 1862-1869.

176. Sanchez-Jimenez, P.E., et al., *Generalized Kinetic Master Plots for the Thermal Degradation of Polymers Following a Random Scission Mechanism.* Journal of Physical Chemistry A, 2010. **114**(30): p. 7868-7876.

177. Gao, Z.M., I. Amasaki, and M. Nakada, *A thermogravimetric study on thermal degradation of polyethylene.* Journal of Analytical and Applied Pyrolysis, 2003. **67**(1): p. 1-9.

178. Paik, P. and K.K. Kar, *Thermal degradation kinetics and estimation of lifetime of polyethylene particles: Effects of particle size.* Materials Chemistry and Physics, 2009. **113**(2-3): p. 953-961.

179. Staggs, J.E.J., *Discrete bond-weighted random scission of linear polymers.* Polymer, 2006. **47**(3): p. 897-906.

180. Emsley, A.M. and R.J. Heywood, *COMPUTER MODELING OF THE DEGRADATION OF LINEAR-POLYMERS.* Polymer Degradation and Stability, 1995. **49**(1): p. 145-149.

181. Schulz, G., *Die Bildung polymerer Stoffe durch Kondensationsgleichgewichte. I.* Zeitschrift für Physikalische Chemie, 1938. **182**(1): p. 127-144.

182. Flory, P.J., *Molecular size distribution in linear condensation polymers.* Journal of the American Chemical Society, 1936. **58**: p. 1877-1885.

183. Odian, G., *Principles of polymerization*. 2004: John Wiley & Sons.

184. Hageman, J.C.L., et al., *Bond scission in a perfect polyethylene chain and the consequences for the ultimate strength.* Macromolecules, 2000. **33**(24): p. 9098-9108.

185. Fedosov, D.A., A. Sengupta, and G. Gompper, *Effect of fluid-colloid interactions on the mobility of a thermophoretic microswimmer in non-ideal fluids.* Soft Matter, 2015. **11**(33): p. 6703-6715.

186. Fan, X.J., et al., *Simulating flow of DNA suspension using dissipative particle dynamics.* Physics of Fluids, 2006. **18**(6).

187. Wang, Y., et al., *Controlled release of entrapped nanoparticles from thermoresponsive hydrogels with tunable network characteristics.* Soft Matter, 2020. **16**(20): p. 4756-4766.

188. Avalos, J.B. and A.D. Mackie, *Dynamic and transport properties of dissipative particle dynamics with energy conservation.* Journal of Chemical Physics, 1999. **111**(11): p. 5267-5276.

189. Palkar, V. and O. Kuksenok, *Modeling Reactive Hydrogels: Focus on Controlled Degradation*, in *Dynamics and Transport in Macromolecular Networks: Theory, Modelling, and Experiments*, L.-T. Yan, Editor., WILEY-VCH (submitted).

# APPENDIX A

## Implementation specifics for mSRP with bond breaking and formation

For this discussion, I will first introduce two types of C++ classes implemented within LAMMPS[A1-A3], namely pair styles and fix styles. Pair styles primarily compute pairwise forces between beads, e.g. the pairwise DPD forces, while fix styles perform some operation during a simulation timestep. The segmental repulsive potential in LAMMPS, as implemented by Tim Sirk and co-workers[A4, A5], is based on one pair style for the additional SRP potential (pair_srp.cpp) and one fix style (fix_srp.cpp) for handling pseudo beads during the simulation run.

To add the functionality of creation and deletion of pseudo beads upon bond creation or breaking, correspondingly, additions are needed to both styles. These additions are implemented in LAMMPS as files with a "_react" suffix (pair_srp_react.cpp and fix_srp_react.cpp) and these files are discussed below. Within these two files, major modifications to code are either in the class constructor or some member functions. Since both pair srp_react and fix srp_react are derived from the corresponding parent classes (pair srp and fix srp, respectively), the constructor of the original class is always called by default when instantiating either of the srp_react classes. Hence the constructor of srp_react only has the additional operations for this class. On the other hand, most member functions in the srp_react classes overwrite the function of the same name in the original srp class. Hence, member functions have the same code as in the original srp along with additions for the srp_react functionalities.

## pair_srp_react.cpp

*PairSRPREACT():*

In the constructor of the original pair srp class, an instance of the fix srp is created. As we will use the fix srp_react instead of fix srp, the fix srp is first deleted and then the fix srp_react is instantiated.

```
if (lmp->citeme) lmp->citeme->add(cite_srpreact);

// pair srp/react has its own fix, hence delete fix srp instance
// created in the constructor of pair srp
for( int ifix = 0; ifix<modify->nfix; ifix++)
  if( strcmp(modify->get_fix_by_index(ifix)->style, "SRP") == 0)
    modify->delete_fix(ifix);

// similar to fix SRP, create fix SRP REACT instance here with unique fix id
f_srp = (FixSRPREACT *) modify->add_fix(fmt::format("{:02d}_FIX_SRP_REACT all
SRPREACT",srp_instance));
++srp_instance;
```

*settings()*

The settings function serves the purpose of reading srp parameters from the input script. For the case of reactions along with srp, one additional parameter needs to be read from the input, namely the ID of the fix style that executes the reaction. The ID of the reaction fix style is passed to the pair srp command as follows (reproduced from edited manual page[A6]):

pair style srp/react cutoff btype dist react-id keyword value ...

The following code in the settings() function reads the react-id, searches the id within LAMMPS, decides whether it is fix bond break or fix bond create and stores the ID in either the idbreak or idcreate variables:

```
// default bond/break and bond/create settings
bond_break = false;
bond_create = false;
idbreak = nullptr;
idcreate= nullptr;

// find whether id is of bond/break or bond/create
const char* reactid = arg[3];
if(strcmp(modify->get_fix_by_id(reactid)->style,"bond/break") == 0)
{
  bond_break = true;
  int n = strlen(reactid) + 1;
  idbreak = new char[n];
  strcpy(idbreak, reactid);
}
else if(strcmp(modify->get_fix_by_id(reactid)->style,"bond/create") == 0)
{
  bond_create = true;
  int n = strlen(reactid) + 1;
  idcreate = new char[n];
  strcpy(idcreate, reactid)
}
else
  error->all(FLERR,"Illegal pair_style command");
```

*init_style()*

The id of the reaction fix read in the settings() function is passed to fix srp_react via the

init_style() function. The relevant part of code is as follows:

```
// if using fix bond/break, set id of fix bond/break in fix srp
// idbreak = id of fix bond break
if( bond_break )
{
  sprintf(c0, "%s", idbreak);
  arg0[0] = (char *) "bond/break";
  arg0[1] = c0;
  f_srp->modify_params(2, arg0);
  delete [] idbreak;
}

// if using fix bond/create, set id of fix bond/create in fix srp
// idcreate = id of fix bond break
if( bond_create )
{
  sprintf(c0, "%s", idcreate);
  arg0[0] = (char *) "bond/create";
  arg0[1] = c0;
  f_srp->modify_params(2, arg0);
  delete [] idcreate;
}
```

## fix_srp_react.cpp

The first task in the fix srp_react is to store and process information passed from the pair style srp_react as mentioned in the previous section. The modify_param() and init() functions undertake this task.

*modify_param()*
This function is called from the init_style() function in pair srp_react (see above) and passes information from pair srp_react to fix srp_react. The relevant addition that passes the ID of the reaction fix:

```
if (strcmp(arg[0],"bond/break") == 0) {
  int n = strlen(arg[1]) + 1;
  idbreak = new char[n];
  strcpy(idbreak,arg[1]);
  return 2;
}
if (strcmp(arg[0],"bond/create") == 0) {
  int n = strlen(arg[1]) + 1;
  idcreate = new char[n];
  strcpy(idcreate,arg[1]);
  return 2;
}
```

*init()*
The init() function creates instances of pointers to fix bond/break or fix bond/create as per information obtained via modify_param.

```
// find fix bond break
if( idbreak != nullptr )
  f_bb = (FixBondBreak *) modify->get_fix_by_id(idbreak);

// find fix bond create
if( idcreate != nullptr )
  f_bc = (FixBondCreate *) modify->get_fix_by_id(idcreate);

// free memory
delete [] idbreak;
delete [] idcreate;
```

After fix srp_react has received all relevant information, the next step is the heart of the problem, i.e. insertion and deletion of beads.

To understand the functions henceforth, it is helpful to start from a discussion of how a timestep works in LAMMPS. Following is the relevant part of the pseudocode for a LAMMPS timestep that is necessary in the current context, adapted from the LAMMPS documentation, https://docs.lammps.org/Developer_flow.html.

```
loop over N timesteps:

  # initial integration steps
  fix->initial_integrate()
  fix->post_integrate()

  nflag = neighbor->decide()
  if nflag:
    fix->pre_neighbor()
    neighbor->build()
    fix->post_neighbor()

  force_clear()
  fix->pre_force()

  pair->compute()
  bond->compute()

  fix->post_force()
  fix->final_integrate()
  fix->end_of_step()

end loop
```

The functions of form fix->function() above can be implemented in all fixes while only a few of these are implemented in a particular fix. The reaction fixes, bond/break and bond/create both execute reactions via the fix->post_integrate() function. The reaction fixes update the bond_atom data structure in LAMMPS which is a per-atom list containing bond partners for each atom. However, fix srp does not use this list directly to determine necessary bond particles but depends on a different data structure, bondlist, which is a per-bond list containing the atom-ids forming a particular bond. When a reaction occurs, the post_integrate function updates bond_atom list, and sets up a flag such that the neighbor->decide() function (see pseudocode above) returns true. Then, the neighbor->build() function updates bondlist from bond_atom. Since at this point in

the LAMMPS timestep we have all data needed to update the srp pseudo beads we implement a fix->post_neighbor() function in srp_react.

The following functions describe the overall changes needed to perform the operation described above.

*setmask()*
The setmask() function passes information about which of the fix->function() functions (see timestep pseudocode above) are implemented in a particular fix. As we implement a new post_neighbor function that is added to the mask in the setmask function via:

```
mask |= POST_NEIGHBOR;
```

*post_neighbor()*
This function checks whether a reaction has occurred via the number of bonds broken or created in a particular time step and then calls the setup_pre_force() function from the original fix srp class which builds the bond particle array based on the bondlist.

```
void FixSRPREACT::post_neighbor()
{
  // store ncalls as it is reset in fix srp setup pre force
  int ncalls = neighbor->ncalls;

  if( idbreak != nullptr)
    if(f_bb->breakcount)
    {
      setup_pre_force(0);

      //reset break count before exiting
      // not reseting breakcount would lead to redundant rebuilds
      f_bb->breakcount=0;

      // count additional call during setup_pre_force
      neighbor->ncalls = ncalls+1;
    }
  if( idcreate != nullptr)
    if(f_bc->createcount)
    {
      setup_pre_force(0);

      //reset create count before exiting
      // not reseting createcount would lead to redundant rebuilds
      f_bc->createcount=0;
```

```
      // count additional call during setup_pre_force
      neighbor->ncalls = ncalls+1;
    }
}
```

## References


A1. Plimpton, S., *Fast Parallel Algorithms for Short-Range Molecular Dynamics.* J. Comput. Phys., 1995. **117**(1): p. 1-19.

A2. *LAMMPS Molecular Dynamics Simulator*. Available from: http://lammps.org.

A3. Thompson, A.P., et al., *LAMMPS-a flexible simulation tool for particle-based materials modeling at the atomic, meso, and continuum scales.* Computer Physics Communications, 2022. **271**.

A4. Sirk, T.W., et al., *An enhanced entangled polymer model for dissipative particle dynamics.* Journal of Chemical Physics, 2012. **136**(13): p. 11.

A5. Sirk, T.W. *Pair style srp*. 2012 February 13, 2023]; Available from: https://docs.lammps.org/pair_srp.html#.

A6. Palkar, V. *Pair style srp/react*. 2022 February 13, 2023]; Available from: https://docs.lammps.org/pair_srp.html#pair-style-srp-react-command.

# APPENDIX B

# PERMISSIONS FOR REPRODUCING JOURNAL ARTICLES

# APPENDIX C

# PERMISSIONS FOR REPRODUCING FIGURES